Large Eddy Simulations of Sand Transport and Deposition in the Internal Cooling Passages of Gas Turbine Blades

Sukhjinder Singh

Dissertation submitted to the faculty of
Virginia Polytechnic Institute and State University
in partial fulfillment of the requirements for the degree of

Doctor of Philosophy
in
Mechanical Engineering

Danesh K. Tafti, Chair
Clinton L. Dancey
Srinath V. Ekkad
Wing F. Ng
Christopher J. Roy

March 21, 2014
Blacksburg, Virgnia

Keywords: Computational Fluid Dynamics (CFD), Heat Transfer, Sand Transport, Multiphase Flows, Large Eddy Simulations (LES), Internal Cooling, Deposition, Coefficient of Restitution

ABSTRACT

Large Eddy Simulations of Sand Transport and Deposition in the Internal Cooling Passages of Gas Turbine Blades

Sukhjinder Singh

Jet engines often operate under dirty conditions where large amounts of particulate matter can be ingested, especially, sand, ash and dirt. Particulate matter in different engine components can lead to degradation in performance. The objective of this dissertation is to investigate sand transport and deposition in the internal cooling passages of turbine blades. A simplified rectangular geometry is simulated to mimic the flow field, heat transfer and particle transport in a two pass internal cooling geometry. Two major challenges are identified while trying to simulate particle deposition. First, no reliable particle-wall collision model is available to calculate energy losses during a particle wall interaction. Second, available deposition models for particle deposition do not take into consideration all the impact parameters like impact velocity, impact angle, and particle temperature. These challenges led to the development of particle wall collision and deposition models in the current study.

First a preliminary simulation is carried out to investigate sand transport and impingement patterns in the two pass geometry by using an idealized elastic collision model with the walls of the duct without any deposition. Wall Modeled Large Eddy Simulations (WMLES) are carried to calculate the flow field and a Lagrangian approach is used for particle transport. The outcome of these simulations was to get a qualitative comparison with experimental visualizations of the impingement patterns in the two pass geometry. The results showed good agreement with

experimental distributions and identified surfaces most prone to deposition in the two pass geometry.

The initial study is followed by the development of a particle-wall collision model based on elastic-plastic deformation and adhesion forces by building on available theories of deformation and adhesion for a spherical contact with a flat surface. The model calculates deformation losses and adhesion losses from particle-wall material properties and impact parameters and is broadly applicable to spherical particles undergoing oblique impact with a rigid wall. The model is shown to successfully predict the general trends observed in experiments.

To address the issue of predicting deposition, an improved physical model based on the critical viscosity approach and energy losses during particle-wall collisions is developed to predict the sand deposition at high temperatures in gas turbine components. The model calculates a sticking or deposition probability based on the energy lost during particle collision and the proximity of the particle temperature to the softening temperature. For validation purposes, the deposition of sand particles is computed for particle laden jet impingement on a coupon and compared with experiments conducted at Virginia Tech. Large Eddy Simulations are used to calculate the flow field and heat transfer and particle dynamics is modeled using a Lagrangian approach. The results showed good agreement with the experiments for the range of jet temperatures investigated.

Finally the two pass geometry is revisited with the developed particle-wall collision and deposition model. Sand transport and deposition is investigated in a two pass internal cooling geometry at realistic engine conditions. LES calculations are carried out for bulk Reynolds number of 25,000 to calculate flow and temperature field. Three different wall temperature boundary conditions of 950 ^{o}C, 1000 ^{o}C and 1050 ^{o}C are considered. Particle sizes in the range 5-25 microns are considered, with a mean particle diameter of 6 microns. Calculated impingement and deposition patterns are discussed for different exposed surfaces in the two pass geometry. It is evident from this study that at high temperatures, heavy deposition occurs in the bend region and in the region immediately downstream of the bend.

The models and tools developed in this study have a wide range of applicability in assessing erosion and deposition in gas turbine components

To my father

ACKNOWLEDGEMENTS

My first debt of gratitude must go to my father, who worked several times harder than me and sacrificed a lot for my every little achievement and success. I certainly could not have come this far without his support and faith in me.

I would like to express my sincere gratitude to my advisor, Dr. Danesh Tafti for his continuous support throughout my PhD study and research, for his patience, motivation, enthusiasm, and immense knowledge. He patiently provided the vision, encouragement and the advice necessary for me to proceed through the doctoral program and complete my dissertation. He was always there for us in the lab, even on the weekends and holidays. I was always humbled by his wealth of knowledge and experience. Even if I was able to learn a little from him, it will go a long way. I also thank him for providing me with the opportunity to work with a talented team of researchers which included my advisor and my committee members, Dr. Srinath Ekkad and Dr. Wing Ng. I thank them all for the long hours of brainstorming and thoughtful discussions on this project as it has developed over the past three and a half years.

I would also like to thank rest of my committee members Dr. Christopher Roy and Dr. Clinton Dancey for reviewing my research and providing constructive feedback. This work would not have been possible without the financial support and direction of Rolls-Royce, especially Veera Rajendran, N. Wagers, H. Kwen, Paul Davis and B. Barker. I am also very thankful to Dr. Saad Ragab, his door was always open for any questions and discussions on fluid mechanics and CFD.

I highly appreciate the work of Jacob Delimont, Colin Reagle and Matt Murdock for carrying out experimental work which I used to validate my numerical results. I would like to thank all my lab mates: Naresh, Surya, Amit, Nagi, Sunil, Vivek, Ravi, Sai, Kevin, Deepu , Long and Kamal, especially Amit for his help in debugging the code and Naresh for those philosophical discussions, which I missed dearly in the last year.

Finally I would like to thank all my friends and family who stood by me in my good and bad times. I thank my dear mother and my three sisters who patiently waited and supported me throughout my doctoral research.

TABLE OF CONTENTS

LIST OF FIGURES

LIST OF TABLES

Chapter 1
Introduction

Sand and dust ingestion in aircraft engines and related engine failures, continues to be a major area of concern for the aircraft engine industry for the last several decades. As the global transportation and energy needs continue to increase, gas turbine engines are increasingly required to operate in harsh, particle laden environments. These fine particles can cause performance degradation through erosion and deposition in different gas turbine components. Aircrafts operating at low altitudes or at remote landing field are commonly subject to large amounts of fine particulate ingestion. For an aircraft flying through volcanic dust clouds, particles can also be ingested at cruising altitudes. Military aircraft engines frequently operating in desert environments face a drastic life reduction due to sand ingestion. Sand ingestion affects multiple components of a gas turbine engine. Some of the key issues are: compressor erosion, melting and glazing in combustor and turbines, blockage of cooling flow in the internal cooling circuits, blockage of film cooling holes, effect on the turbine efficiency due to changing aerodynamic characteristics as a result of deposition on the airfoil external surfaces, casing distortion and associated performance drop. These ingested particles can also reach the internal cooling passages of the turbine blades. Cooling air which is bled from the compressor can carry along significant amounts of sand particles to the internal cooling passages. These can deposit in cooling passages and also clog film cooling holes, leading to degradation in cooling performance and even blade metal failure. The problem is exacerbated by ribbed serpentine cooling passages which are dominated by recirculation regions and secondary flows, making them more susceptible to deposition.

Different aspects of the problem of sand and volcanic ash ingestion have been studied in the past, with the majority of the work focused on erosion and deposition of particles on a wide range of materials and under different operating conditions. The relevant literature review is summarized in the chapters to follow. In spite of being a critical engine component and highly susceptible to heat transfer degradation due to particle ingestion, there are no detailed studies on the particle transport in the internal cooling passages of turbine blades. The internal cooling technology for gas turbine components has developed over the years from simple smooth cooling passages to very complex geometries involving many differing surfaces, shapes, and fluid-surface interactions. The fundamental aim of this technology is to obtain the highest overall cooling effectiveness with the lowest possible penalty on the thermodynamic cycle performance. But the presence of fine particles in the cooling circuit can significantly hamper the performance of the internal cooling system. Depending upon the temperatures, the particles can clog cooling holes, deposit on the cooling duct surfaces and develop hot spots leading to degradation in heat transfer and even blade metal failure.

Particle transport and deposition in the hot gas path of a gas turbine engine can be better understood with a careful study of the underlying particle-wall impact mechanism. The coefficient of restitution (COR) is a good measure of the amount of energy lost during an impact and as such an excellent way to measure the effects of impact of the sand particles. With an accurate prediction of COR, it is possible to track particles through multiple impacts and determine which areas in the gas path are likely to see higher levels of deposition. More fundamental particle-wall interaction models can help predict accurately the sand transport and deposition in the hot gas path.

Objective

The objective of this study is to investigate the dynamics of sand impingement and deposition in the internal cooling passages of gas turbine blades with focus on the ribbed duct geometry. Time accurate Large Eddy Simulations are used to accurately characterize the complex turbulent flow field for geometries considered. The sand particles are treated discretely in the Lagrangian frame of reference. A novel particle-wall interaction model is developed to quantify the energy losses and predict the coefficient of restitution for a particle-wall collision. This model is further developed to predict particle deposition at higher temperatures, which accounts for energy losses during a particle wall collision along with change in physical properties of the particle with temperature.

This dissertation is structured as follows. Chapter 1 discusses the motivation and states the research objectives. Chapter 2 presents the Large Eddy Simulations of flow field and heat transfer in a two pass internal cooling geometry. Chapter 3 investigates the sand transport in the two pass internal cooling geometry. Chapter 4 discusses the development and validation of a novel particle-wall collision model to predict coefficient of restitution. Chapter 5 purposes and validates an improve particle deposition model for particulate flows at high temperatures. Chapter 6 explores the sand transport and deposition by using the particle-wall interaction models developed in the previous two chapters. Chapter 7 summarizes the findings and conclusions along with key contributions of the study.

Chapter 2

Large Eddy Simulation of Flow and Heat Transfer in a Two Pass Internal Cooling Geometry[1]

Accurate prediction of ribbed duct flow and heat transfer is of importance to the gas turbine industry. Detailed heat transfer in a two pass stationary square duct with rib turbulators is studied using wall modeled Large Eddy Simulations (WMLES). Each pass has ribs on two opposite walls and aligned normal to the main flow direction. The rib pitch to rib height (P/e) is 9.28, the rib height to channel hydraulic diameter (e/D_h) is 0.0625 and calculations have been carried out for a bulk Reynolds number of 25,000. The present study validates the use of WMLES for predicting flow and heat transfer with published data on similar geometries. The calculations predict the major flow features with reasonable accuracy especially distribution of mean and turbulent quantities in the developing, fully developed and 180^o bend region. It is found that the mean flow and turbulent quantities do not become fully developed until the flow passes the fifth rib of the duct. Results show that the heat transfer augmentation is higher in the second pass after the 180^o turn compared to the first pass. Local heat transfer comparisons show that the heat transfer augmentation shifts towards the outside smooth wall in the second pass after the 180^o turn. In addition to primary flow effects, secondary flow impingement on the smooth walls is found to

[1] A part of this chapter is reproduced from published work in ASME Summer Heat Transfer Conference, paper number, HT2012-58260, with permissions from ASME

develop by the fifth rib, while it continues to evolve downstream of the sixth rib. Results show the local and average distribution of Nusselt numbers normalized with classical Dittus and Boelter correlation.

2.1 . Introduction

Modern gas turbine blades are designed to operate at high temperatures well above allowable metal temperatures, since increased turbine inlet temperature leads to better thermal efficiency. As a result of our pursuit for better thermal efficiency, the turbine blade cooling has received growing and unremitting attention. In most of the practical gas turbines, the turbine blades of high pressure stage are usually too small to employ blade cooling techniques effectively. Many approaches, including novel material or alloy design, improved cooling techniques, and better manufacturing methods have been used to increase the operating temperature limit of the turbine blades and vanes to their current levels. In the cooling technique, internal cooling channels are located in the body of blade and turbine component. Bleed air from compressor is forced through these cooling passages (internal cooling) and openings at the blade external surface (external film cooling). Many cooling strategies including impingement cooling, film cooling and ribbed serpentine passages are employed to maximize the heat transferred from the blade to the coolant. In ribbed serpentine passages, repeated ribs are used on the channel walls as turbulence promoters to achieve heat transfer augmentation. The presence of these ribs leads to complex flow fields such as flow separation, reattachment and secondary flow between the ribs, which produce high turbulence leading to higher heat transfer coefficients. The increase in heat transfer is also accompanied by increased pressure losses due to increased friction in the presence of ribs. The flow and heat transfer in a ribbed internal cooling duct is very sensitive to flow Reynolds number and the geometric parameters such as blockage ratio(e/D_h), the rib pitch(P), the aspect ratio of the duct, the angle of the rib with respect to the flow and shape of the rib.

The present study is motivated by the need to accurately predict flow and heat transfer in such flows. The flow in a ribbed duct has some characteristic complex flow features: boundary layer separation, a curved shear layer, primary and secondary recirculation, reattachment of boundary layer, recovery, etc. Computational cost has limited most applications of CFD to solving the Reynolds averaged Navier-Stokes (RANS) equations and using turbulence models for closure in these equations. Though computationally inexpensive, RANS models are not reliable for flow dominated by massive separations as is the case in present study. Previous studies have shown that the turbulent viscosity and the turbulent shear stress are usually over predicted by two equation models in such flows [1, 2]. The eddy viscosity models which assumes isotropy of turbulence[1], fail to capture the flow features accurately, however, more complicated models have performed reasonably well[2]. The inability of these turbulence models to correctly predict the Reynolds stresses in the regions of high anisotropy, is one of the main reasons for their failure [3, 4]. Saidi and Sunden[5] also used $\kappa - \varepsilon$ models in periodic channel with inline orthogonal ribs, and their calculations showed mixed results. Ooi et al.[6] showed that $\nu^2 - \mathrm{f}$ model performs better than $\kappa - \varepsilon$ and S-A RANS models on orthogonal inline ribs. By using a $\kappa - \varepsilon - \mathrm{A}$ model, which is standard $\kappa - \varepsilon$ model with an Algebraic Stress Model (ASM), Liou[7, 8] was able to account for anisotropy of turbulence in calculations for two dimensional stationary ribbed duct with ribs on one wall. Iacovides and Raisee[9] compared effective viscosity models and differential second moment closure (DSM) models in a periodic ribbed duct, and showed that, even though DSM model could account for anisotropic turbulence, it could not predict heat transfer accurately. Sleiti and Kapat[10] conducted studies comparing several $\kappa - \varepsilon$ models and $\kappa - \omega$ models with Reynolds Stress Model (RSM) with enhanced wall treatment and observed better agreement between the RSM results and experiments in predicting mean flow and smooth side wall heat transfer with some inaccuracy in predicting ribbed wall heat transfer. Rigby[11] employed modified version of Menter's SST model[12, 13] to study heat and mass transfer in two pass ribbed channel with a 180^o turn at low Reynolds numbers (5200-7900), with and without rotation. It was observed that standard models failed to predict the reattachment accurately and modifications in the ω boundary conditions were required to improve accuracy. Despite these shortcomings, RANS models can produce fairly good results and are used widely because of much lower computational cost.

Large eddy simulations (LES) have also been used in the past to study fluid flow and heat transfer in ribbed channel geometries. Murata and Mochizuki[14] reported LES calculations of heat transfer on smooth and ribbed channels, but the Reynolds number was low and accuracy could not be verified as experimental comparison was not available. LES results for ribbed channel, presented by Watanabe and Takahashi[15], showed excellent agreement with mean velocity profiles and heat transfer measurements. Excellent comparisons between LES calculations and experiments have been shown in fully developed stationary ducts by Tafti[16], in fully developed rotating ducts by Abdel-Wahab and Tafti[17] in fully developed stationary ducts with 45^o ribs by Abdel-Wahab and Tafti[18] and in developing flow in stationary and rotating ducts by Sewall and Tafti[19, 20].

Despite the widespread success of LES calculation in predicting flow and heat transfer in turbulent flows, the grid requirements for larger or complex geometries are still very high. The resolution in the boundary layer has to be fine and increases rapidly with Reynolds number. This calls for special treatment of the boundary layer or wall modeling to limit the number of grid points. One such approximation is detached eddy simulation (DES), which was proposed by Spalart et al.[21]. The aim of DES is to combine the most favorable features of LES and RANS methods, i.e., application of RANS model for predicting attached boundary layers and LES for resolution of time dependent, three dimensional large eddies. The technique is non-zonal and simple in formulation, the transition between RANS and LES is seamless in that there is a single equation with no explicit declaration of RANS versus LES zones. Vishwanathan and Tafti[22] presented the capability of DES in predicting the turbulent flow and heat transfer in a two pass internal cooling ribbed duct with a 180^o turn. The results showed good quantitative comparisons with LES and experiments while reducing the computational complexity by nearly an order of magnitude.

The present study presents turbulent flow and heat transfer predictions in a two pass cooling ribbed duct with 180^o turn, using a zonal or two layer wall model. The boundary layer type equation are solved in the inner layer on a virtual grid, imbedded in outer LES grid and refined only in the wall normal direction. Computational details and validation of this wall modeling was previously presented for complex high Reynolds number flows[23].

2.2 Objective

The objective of current study is to evaluate the capabilities of WMLES in predicting the turbulent flow and heat transfer in a two pass internal cooling duct with a 180^o turn. While in many previous numerical studies[24], investigations are mostly limited to heat transfer in the fully developed region of a ribbed duct, this study provides detailed hydrodynamics and heat transfer comparisons in the developing flow, fully developed and 180^0 bend regions of the two pass duct. Of particular interest is the ability of WMLES to predict flow transition, including flow development in the duct, flow in the 180^o bend and the development of secondary flows in the duct cross-section. The overall motivation is to evaluate the use of WMLES for the accurate prediction of heat transfer in ribbed internal cooling ducts.

2.3 Methodology

2.3.1 Computational Model

2.3.1.1 Governing equations

The governing equations for unsteady incompressible viscous flow in a generalized coordinate system consists of mass, momentum, and energy conservation laws. The equations are mapped from physical $(\vec{x})$ to logical/computational space $(\vec{\xi})$ by a boundary conforming transformation $\vec{x} = \vec{x}(\vec{\xi})$, where $\vec{x} = (x, y, z)$ and $\vec{\xi} = (\xi, \eta, \zeta)$. The equations are non-dimensionalized by the hydraulic diameter (D_h^*) and inlet flow velocity scale (U_b^*) and written in conservative non-dimensional form as:

<u>Mass</u>:

$$\frac{\partial}{\partial \xi_j}\left(\sqrt{g} U^j\right) = 0 \tag{1}$$

Momentum:

$$\frac{\partial}{\partial t}\left(\sqrt{g}\,\overline{u}_i\right) + \frac{\partial}{\partial \xi_j}\left(\sqrt{g}\,\overline{U}^j\,\overline{u}_i\right) + \frac{\partial}{\partial \xi_j}\left(\left(\frac{1}{\mathrm{Re}} + \frac{1}{\mathrm{Re}_t}\right)\sqrt{g}\,g^{jk}\,\frac{\partial \overline{u}_i}{\partial \xi_k}\right) = -\frac{\partial}{\partial \xi_j}\left(\sqrt{g}\left(\vec{a}^{\,j}\right)_i \overline{p}\right) \tag{2}$$

Energy:

$$\frac{\partial}{\partial t}\left(\sqrt{g}\,\overline{\theta}\right) + \frac{\partial}{\partial \xi_j}\left(\sqrt{g}\,\overline{U}^j\,\overline{\theta}\right) = \frac{\partial}{\partial \xi_j}\left(\left(\frac{1}{\mathrm{Pr}\,\mathrm{Re}} + \frac{1}{\mathrm{Pr}_t\,\mathrm{Re}_t}\right)\sqrt{g}\,g^{jk}\,\frac{\partial \overline{\theta}}{\partial \xi_k}\right) \tag{3}$$

where $\vec{a}^{\,i}$ are the contravariant basis vectors, $\sqrt{g}$ is the Jacobian of the transformation, g^{ij} is the contravariant metric tensor, $\sqrt{g}U^j = \sqrt{g}(\vec{a}^{\,j})_k u_k$ is the contravariant flux vector, u_i is the Cartesian velocity vector, p is the pressure, and θ the non-dimensional temperature. The non-dimensional time used is $\mathrm{T}^*\,\mathrm{U}_\mathrm{b}^*/\mathrm{D}_\mathrm{h}^*$ and the Reynolds number is given by $\mathrm{U}_\mathrm{b}^*\mathrm{D}_\mathrm{h}^*/\nu$, Re_t is the inverse of the subgrid eddy-viscosity, which is modeled as

$$\frac{1}{\mathrm{Re}_t} = C_s^2\left(\sqrt{g}\right)^{\left(2/3\right)}\left|\overline{S}\right| \tag{4}$$

where $|\overline{S}|$ is the magnitude of the strain rate tensor given by $|\overline{S}| = \sqrt{2\overline{S_{ik}}\,\overline{S_{ik}}}$ and the Smagorinsky constant $C_s{}^2$ is obtained via the dynamic subgrid stress model [34-36]. To this end, a second test filter, denoted by $\hat{G}$, is applied to the filtered governing equations with the characteristic length scale of $(\vec{x})$ being larger than that of the grid filter, $\bar{G}$. The test filtered quantity is obtained from the grid filtered quantity by a second-order trapezoidal filter, which is given by $\hat{\varphi} = \frac{1}{4}(\overline{\varphi}_{i-1} + 2\overline{\varphi}_i + \overline{\varphi}_{i+1})$ in one dimension. The resolved turbulent stresses, representing the energy scales between the test and grid filters, $L_{ij} = \hat{\bar{u}}_i \hat{\bar{u}}_j - \hat{\bar{u}}_i \hat{\bar{u}}_j$ are then related to the subtest, $T_{ij} = \widehat{\overline{u_i u_j}} - \hat{\bar{u}}_i \hat{\bar{u}}_j$ and subgrid-scale stresses, $\tau_{ij} = \overline{u_i u_j} - \bar{u}_i \bar{u}_j$ through the identity, $L_{ij}^a = T_{ij}^a - \hat{\tau}_{ij}^a$. The anisotropic subgrid and subtest-scale stresses are then formulated in terms of the Smagorinsky eddy viscosity model as:

$$\tau_{ij}^a = -2C_s^2 \left(\sqrt{g}\right)^{2/3} \left|\bar{S}\right| \overline{S_{ij}} \tag{5}$$

$$T_{ij}^a = -2C_s^2 \alpha \left(\sqrt{g}\right)^{2/3} \left|\hat{\bar{S}}\right| \widehat{\overline{S_{ij}}} \tag{6}$$

Using the identity,

$$\begin{aligned} L_{ij}^a &= L_{ij} - \frac{1}{3}\delta_{ij} L_{kk} = 2C_s^2 \left(\sqrt{g}\right)^{2/3} \left[\alpha \left|\hat{\bar{S}}\right| \widehat{\overline{S_{ij}}} - \widehat{\left|\bar{S}\right| \overline{S_{ij}}} \right] \\ &= -2C_s^2 \left(\sqrt{g}\right)^{2/3} M_{ij} \end{aligned} \tag{7}$$

Here α is the square of the ratio of the characteristic length scale associated with the test filter to that of grid filter and is taken to be $\left[\hat{\bar{\Delta}}_i / \bar{\Delta}_i = \sqrt{6}\right]$ for a representative one-dimensional test filtering operation[25]. Using a least-squares minimization procedure of Lilly[26], a final expression for $C_s{}^2$ is obtained as:

$$C_s{}^2 = -\frac{1}{2} \frac{1}{(\sqrt{g})^{2/3}} \frac{L_{ij}^a \bullet M_{ij}}{M_{ij} \bullet M_{ij}} \tag{8}$$

The value of $C_s{}^2$ is constrained to be positive by setting it to zero when $C_s{}^2 < 0$.

2.3.1.2 Zonal two layer velocity model

The two layer wall model is formulated by solving a reduced set of simplified equations in the inner wall layer. The inner layer equations are solved on a virtual embedded grid along a normal between the first off-wall grid point ($y^+ < 50$) and the wall. The coupling between the inner and outer layer is accomplished by using the instantaneous outer flow velocity as a boundary condition to the inner layer, which is used to compute the wall shear stress by solving a suitable set of reduced equations. The wall shear stress is then used as a boundary condition in the solution of the outer layer equations at the first off-wall node.

A reduced set of equations in local wall coordinates (*n, t*) is formulated. Instead of solving three separate equations in the inner layer (one for each component of velocity), an effective tangent momentum transport equation is constructed(eq. 9 below) by neglecting the convection and time derivative terms, reducing the number of independent variables to one spatial dimension (n), allowing the solution of a tri-diagonal system of equations at each station along the normal to the wall.

$$\frac{\partial}{\partial n}\left[\left(\frac{1}{\mathrm{Re}}+\frac{1}{\mathrm{Re}_t}\right)\frac{\partial u_t}{\partial n}\right]=\frac{\partial P}{\partial t} \tag{9}$$

with $u_t = 0$ at the wall and $u_t = \|\vec{U}_t\|$ at the edge of the inner layer, where $\vec{U}_t$ is the instantaneous tangential velocity at the first off-wall grid point.

The eddy-viscosity is modeled[27] by

$$\begin{aligned}
\frac{1}{\mathrm{Re}_t} &= \frac{\kappa}{\mathrm{Re}} d^+ \left(1-e^{-d^+/A}\right)^2 \\
d^+ &= \rho u_\tau d / \mu \\
u_\tau &= \sqrt{\|\tau_w\| / \rho}
\end{aligned} \tag{10}$$

where κ is the von Karman constant, *d* is the normal distance from the wall, and A=19. The one-dimensional equation is solved iteratively (for u_t and $\|\tau_w\|$) by using a standard tri-diagonal solver for a second-order central difference approximation.

From the solution of Equation (10), the magnitude of the tangential wall shear stress is calculated as

$$\|\tau_w\| = \frac{1}{\mathrm{Re}} \frac{\partial u_t}{\partial n} |_{wall} \tag{11}$$

which is then decomposed into the respective directional components.

The calculated stress components at the wall can now be directly incorporated into the discretized momentum equations (Eqn. 2) at the first off-wall grid point in the outer layer. Substitution of the directional stress in the respective momentum equation completes the coupling between the inner and outer layer. More details of the procedure are outlined in Patil and Tafti[23].

2.3.1.3 Zonal two layer heat transfer model

An equivalent form to Equation (9) can be written for the energy equation in the inner layer as

$$\frac{\partial}{\partial n}\left[\left(1+\frac{\mathrm{Re}\cdot \mathrm{Pr}}{\mathrm{Re}_t \cdot \mathrm{Pr}_t}\right)\frac{\partial \theta}{\partial n}\right]=0 \tag{12}$$

Solution of Equation (12) requires the closure model for the turbulent Prandtl number. For the current investigation, the formulation of Kays [28] is used and presented in Equation (13).

$$1/\mathrm{Pr}_t = 0.58 + 0.22\left(\frac{\mathrm{Re}}{\mathrm{Re}_t}\right) - 0.0441\left(\frac{\mathrm{Re}}{\mathrm{Re}_t}\right)^2 \left\{1-\exp\left[\frac{-5.165}{\left(\frac{\mathrm{Re}}{\mathrm{Re}_t}\right)}\right]\right\} \tag{13}$$

Equation (12) is solved in the inner layer zonal mesh in a same way that Equation (9) is solved. The temperature at the first LES grid point off the wall and the specified wall temperature are used as boundary conditions for solving Equation (13). The heat flux at the wall is obtained using Equation (14) as

$$q''_w = -\frac{1}{\mathrm{Re}\cdot\mathrm{Pr}}\frac{d\theta}{dn}\Big|_{wall} \tag{14}$$

This heat flux is used as a boundary condition for the outer LES grid instead of using the specified wall temperature similar to the approach for the velocity model.

2.3.2 Numerical method

The governing equations for momentum and energy are discretized with a conservative finite-volume formulation using a second-order central (SOC) difference scheme on a non-staggered grid topology. The SOC discretization has minimal dissipation and has been shown to be suitable for LES computations. The Cartesian velocities and pressure are calculated and stored at the cell center, whereas contravariant fluxes are stored and calculated at cell faces. The discretized continuity and momentum equations are integrated in time using a projection method. The temporal advancement is performed in two steps, a predictor step, which calculates an intermediate velocity field, and a corrector step, which calculates the updated velocity at the new time step by satisfying discrete continuity. The computer program Generalized Incompressible Direct and Large Eddy Simulations of Turbulence (GenIDLEST) used for the current study has been applied and validated for numerous complex heat transfer and fluid flow problems. Details about the algorithm, functionality, and capabilities can be found in Tafti[29, 30]

2.3.2.1 Geometry description

A simplified geometry for the two pass internal cooling duct is considered in the present study. The geometry is a U-shaped duct with square cross section as shown in figure 2.1. All dimensions are based on the characteristic length, the hydraulic diameter of the duct (D_h = 0.0508m). Each pass has ribs on two opposite walls and aligned normal to the main flow. Rib height (e) is $0.0625D_h$ and pitch length (P) is $0.58D_h$ and hence rib pitch to rib height ratio is 9.28. First pass has 16 and second pass has 14 equally spaced ribs. Each pass is $20D_h$ long and clearance between two passes is $0.25D_h$.

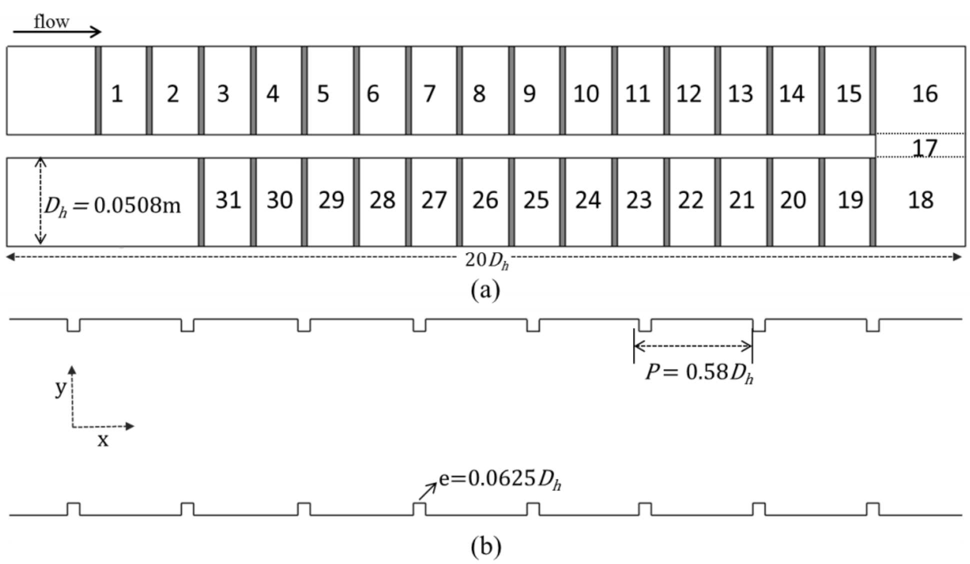

Figure 2.1 Computational domain (a) Side view of two pass with pitch numbering shown (b) Bottom view, ribs at a section

2.3.2.2 Computational grid

An LES grid is constructed using a multi-block topology. Each rib unit is the section from center of one pitch to the next. In total, each rib unit is discretized into 38×68×64 cells (Figure 2.2) and was divided into 7 blocks to facilitate parallel processing. The 180^o bend was discretized into 64×68×144 cells and 9 blocks. The second pass has an outlet region which is around 5 hydraulic diameters long. Near wall grid spacing of an approximate y+ of 30 is used for the wall model, as used in our previous studies on a ribbed duct[31]. All these sum to 5.8 million cells distributed on 153 blocks.

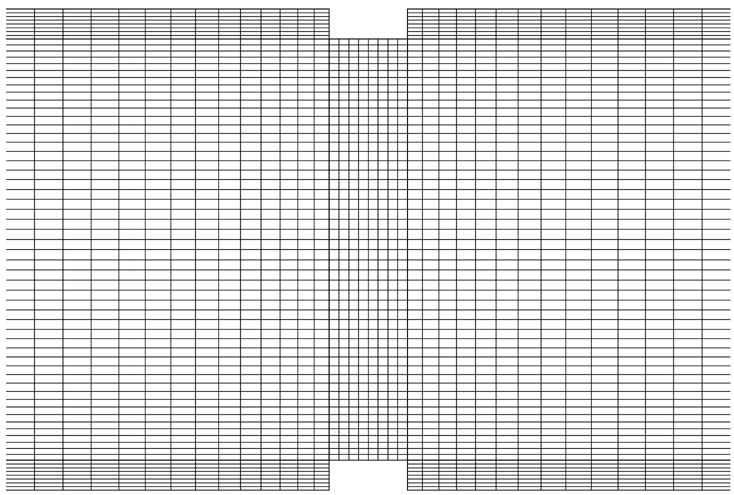

Figure 2.2 Computational grid for one repeated pitch element

2.3.2.3 Boundary conditions

In the present study, the flow Reynolds number is 25,000, based on the mean velocity at the inlet and hydraulic diameter of the duct. The non-dimensional velocity at the inlet is set to 1 and convective outflow boundary condition is used at the outlet. The duct inlet has constant velocity profile normal to the boundary. For heat transfer computations, constant wall temperature boundary condition is used.

2.3.2.4 Solver control

The convergence criteria for the momentum and pressure are 1E-5 and 1E-5 respectively, at each time step. The time step is set at 2E-4. The flow is first allowed to develop and reach a statistically stationary state, which takes nearly 20 non-dimensional time units.

2.4 Results

In this section, first, the calculated flow field in the two pass duct with 180^o turn is discussed and second, the heat transfer augmentation results are presented.

2.4.1 Flow field.

Calculations of flow field in a fully developed and developing ribbed duct have been published before [24, 32], the flow is identical to fully developed case after fifth rib in the first pass. Figure 2.3 shows mean streamlines distribution at the mid-plane parallel to ribbed wall. The flow begins to feel the presence of the 180^o turn about $1D_h$ upstream of the last rib. At upstream of the edge of the bend, a strong shear layer is formed due to considerable flow acceleration on the inside of the turn. A large recirculation zone is formed at the upstream corner as the bulk of the flow is pushed towards the downstream side of the bend. Similarly, a smaller recirculation region forms at the downstream outer corner. Flow separation at the tip of the dividing wall also leads to a recirculation zone. After hitting the back wall of the bend, the flow impinges the outer wall of the second pass while coming out of the bend.

Figure 2.4(a) shows mean streamline pattern in a rib unit at a fully developed location (pitch number 8) in the first pass. Flow patterns observed by the earlier LES studies[16, 33], the RANS model[6] and the experiments[34] show similar pattern. The mean flow is characterized by a leading edge eddy at the rib-wall junction, a recirculation zone at the top of the rib, a counter rotating eddy in the wake of the rib wake and the main recirculation region behind the rib. The reattachment length is calculated as $4.8\mathrm{e}$ compared to experimentally observed values $4.0\mathrm{e} - 4.25\mathrm{e}$ $(\mathrm{P/e} = 10, \mathrm{e/D_h} = 0.1)$. An important characteristic of ribbed duct flow is the presence of secondary flows, which have large impact on the heat transfer augmentation on side walls.

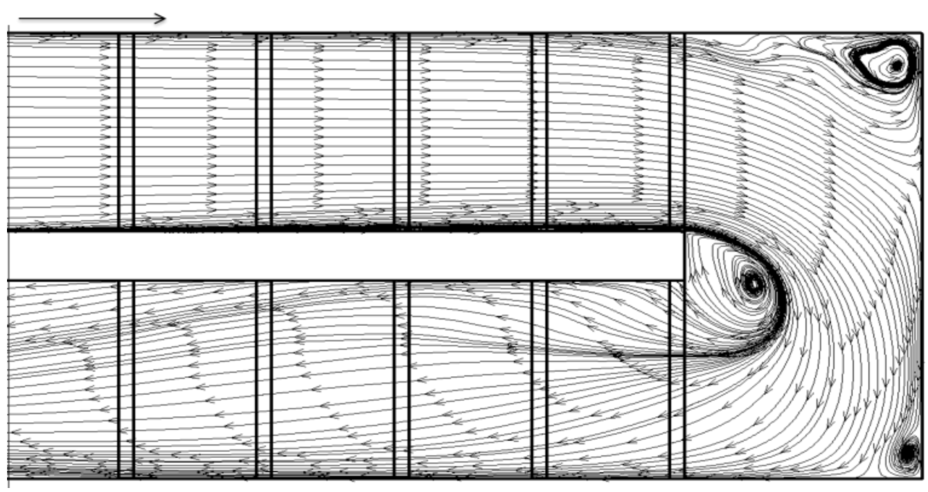

Figure 2.3 Mean streamline distribution at a plane parallel to ribbed wall, $0.5D_h$ away (entire geometry not shown)

These secondary flows are driven by the periodic flow disturbance caused by the ribs and the junction flow where the ribs meet the side wall [16]. In the vicinity of rib-sidewall junction, strong localized unsteady vertical structures are generated. Figure 2.4(b) shows contours of spanwise velocity in the vicinity of the rib-sidewall junction. Lateral impingement velocities as high as 18%

are found in this region, indicating a strongly three dimensional flow. Except in the immediate vicinity of the rib, the secondary flow is weak. The high spanwise velocities in this region are also result of highly unsteady vortices that are formed in the region

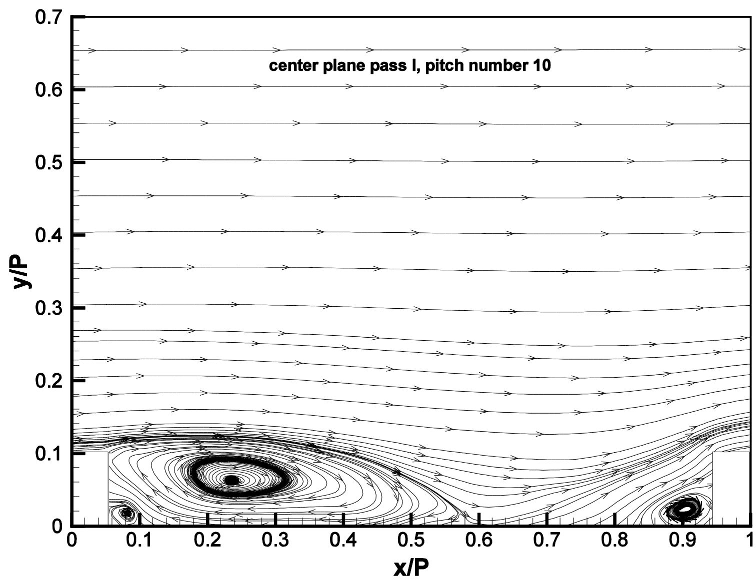

(a)

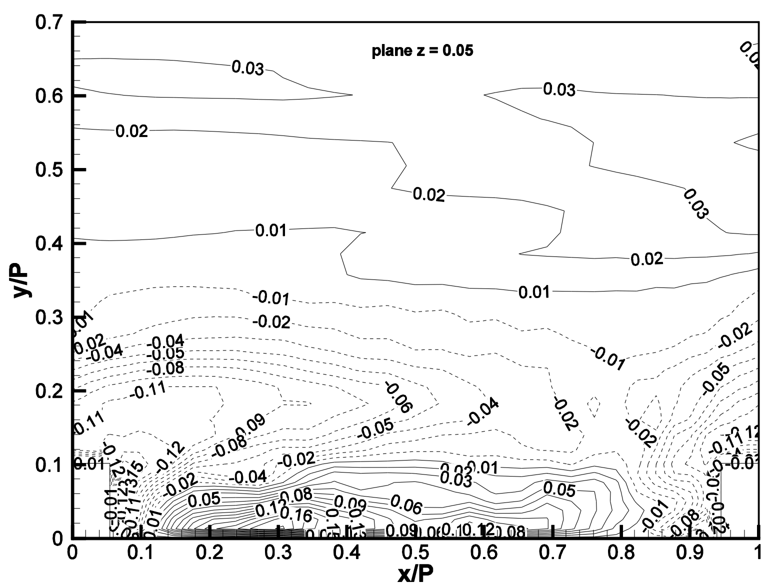

(b)

Figure 2.4 (a) Mean streamline distribution in a pitch length (10) at the z symmetry plane. (b) Mean spanwise velocity in the vicinity of the smooth wall

Figure 2.5 shows the coherent structures (iso-vorticity) in the computational domain. The figure shows large number of coherent structures and hence turbulence intensity in the first half of second pass after the 180^o turn. Highly turbulent flow in the second pass is consistent with previous studies on similar geometries [24, 33, 35] .

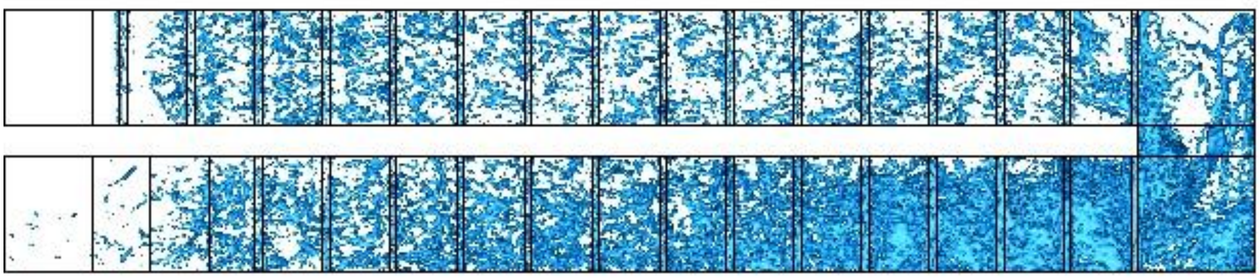

Figure 2.5 Coherent structures in the computational domain

Figure 2.6(a)-(c) show contours of resolved turbulent u_{rms} , v_{rms} and w_{rms} at centerplanes (z = 0.5) at pitch number 14 in pass-I and pitch 20 in pass-II. The streamwise fluctuations u_{rms} are highest in the separated shear layer at the leading edge of the rib, with values between 28% to 33% in first pass (pitch # 14)and 38% to 43% in second pass (pitch # 20). They are lowest in the stagnating flow at the rib and in the recirculation region immediately behind the rib. The transverse fluctuations v_{rms}, at the centerplane in shown pitches, fig 2.6(b), exhibit values of 15%-20% in first pass and 23%-25% in the second pass, in the stagnation region of the rib as well as in the separated shear layer downstream of the rib. The predicted values are much higher in the second pass, showing highly three dimensional nature and strong secondary flows in second pass. The lateral fluctuations w_{rms}, in the centerplane in the shown pitches fig 2.6(c), exhibit a maximum value of 34% in first pass and 38% in second pass at the top leading edge of the rib.

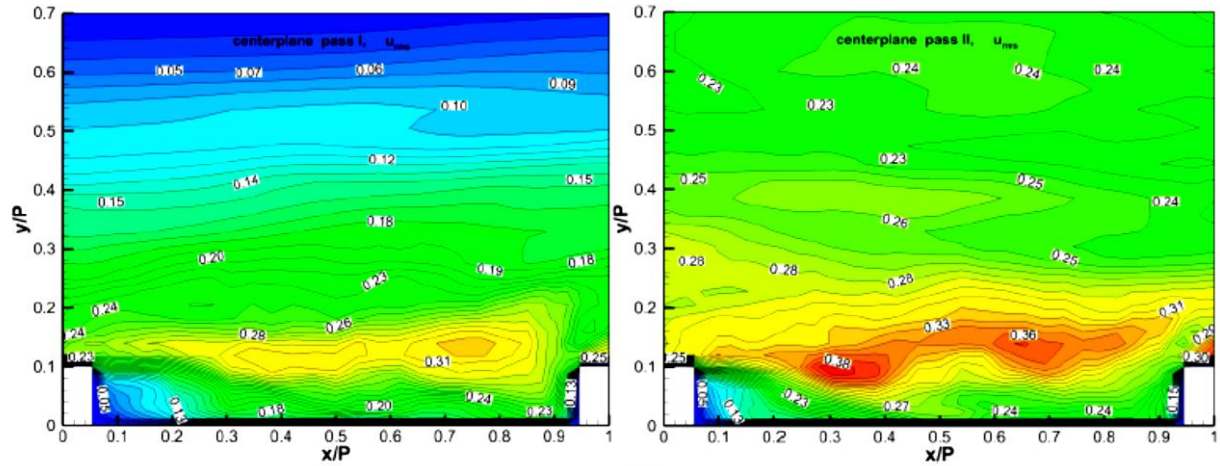

(a)

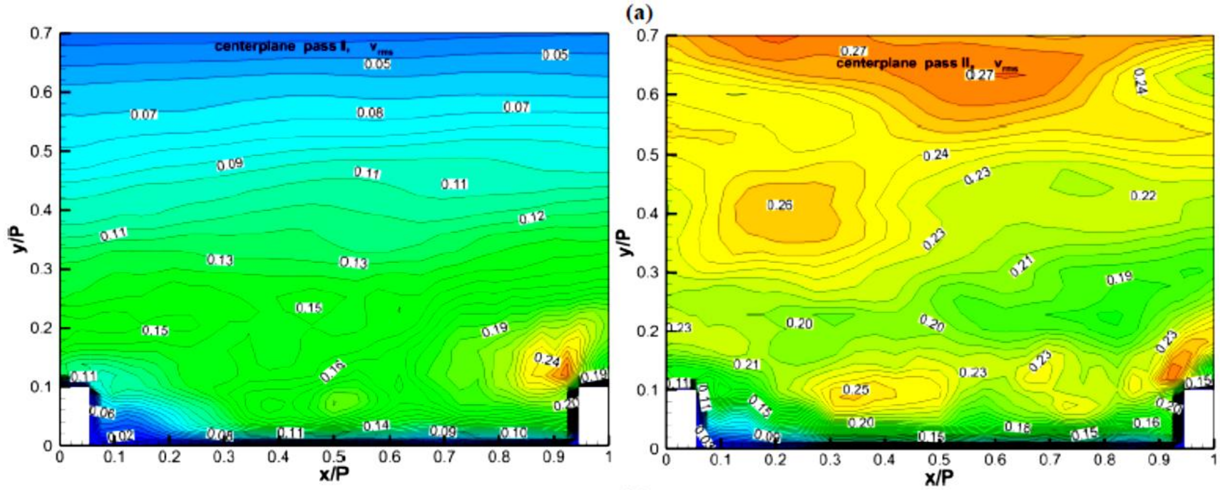

(b)

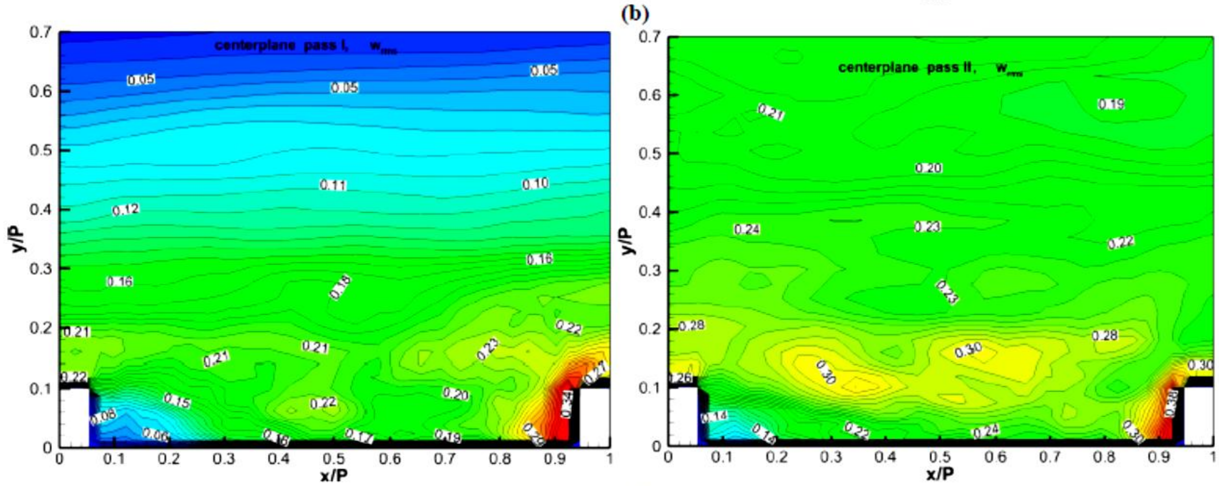

(c)

Figure 2.6 Resolved turbulent quantities at centerplane in pass-I (left) and pass-II (right); (a) u_{rms}, (b) v_{rms} and (c) w_{rms} pitch 14 and 20.

The high lateral intensities are a result of impingement of eddies at the leading edge of the rib leading to strong secondary flows. The lateral fluctuations are also high in the shear layer downstream of the rib with intensities reaching 22% and 32% in pass-I and pass-II respectively. The trends in these plotted quantities are qualitatively similar to reported by Tafti[16] and Rau[34], but not as high due to different e/P ratio of the present study.

2.4.2 Heat Transfer.

The heat transfer augmentation develops till the fifth rib, after which the distribution exhibits a quasi-periodic state. Similar observations can be made at the side wall. Figure 2.7(b) shows pitch averaged augmentation for the ribbed wall. Highest heat transfer augmentation ($< Nu >/Nu_o = 2.85$) is observed in the downstream half of the U-bend and the region just downstream of the bend. This observation is consistent with the prediction of high turbulence in the flow field in this region. The heat transfer augmentation is nearly identical in all pitch lengths after the fifth rib and starts increasing just few pitches upstream of the bend where the flow starts turning due to the presence of the bend. Hence, in the first pass highest heat transfer augmentation is observed

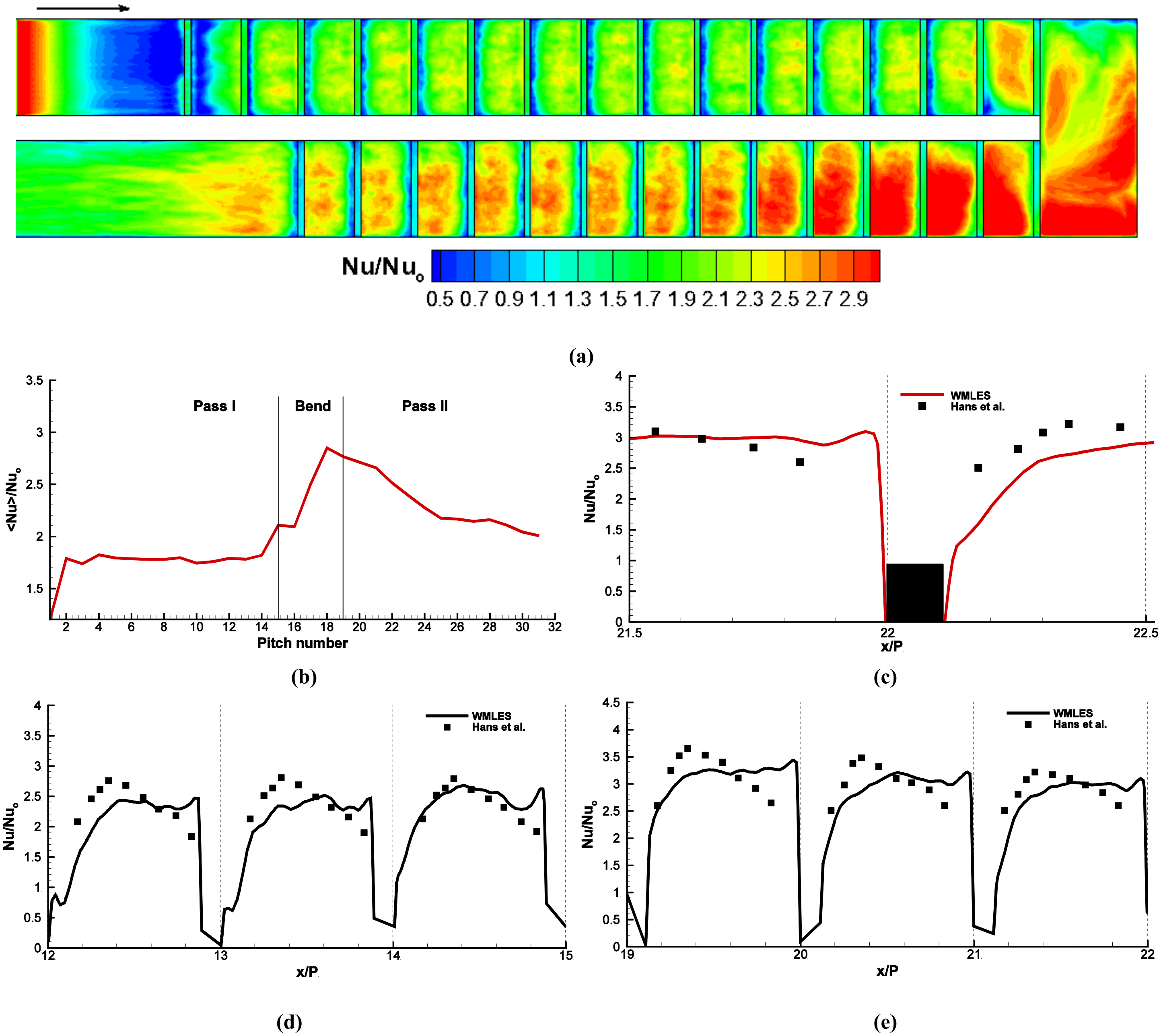

Figure 2.7 (a) Normalized Nusselt number countours on ribbed wall (b) Pitch averaged heat transfer augmentation; Normalized Nusselt number variation in (c) representative fully developed pitch length in the second pass (d) upstream region of bend (e) downstream region of bend

in the pitch length just upstream of the U-bend. Also, in this region the flow and heat transfer is no more symmetric in the span-wise direction due to turning of flow. As the flow enters the bend after passing over the final rib in the pass, regions of high heat transfer are observed. Low heat transfer regions, hot spots, are predicted in the upstream corner of the bend due to presence of recirculation zones. In the downstream corner of the bend, high heat transfer is observed on all walls due to direct flow impingement. Heat transfer in the second pass is highest in the region immediately downstream of the first rib and falls gradually with distance from the 180^{o} bend. While the flow is effectively symmetric in the first pass, the flow in second pass is highly asymmetric immediately downstream of the bend. The flow tries to regain symmetry gradually but it is observed that asymmetry prevails in the whole second pass. This asymmetry can be seen in heat transfer augmentation also, observed heat transfer is higher towards the outer smooth wall compared to the divider wall. Heat transfer on the smooth side walls in second pass is also higher than compared to first pass, consistent with higher turbulence and much stronger secondary flows along with direct flow impingement in second pass.

The predictions are compared to experiments of Han et al.[36]. The experiments were performed in similar geometry with slight differences ($\mathrm{P/e} = 10, \mathrm{e/D_h} = .063,\ \mathrm{Re} = 30{,}000$). Figure 2.7(c) shows heat transfer augmentation across a representative rib in second pass (between pitch # 22 and 23). High heat transfer is predicted immediately upstream of the rib, which is result of highly unsteady vortical flow in this region. These secondary vortices transfer heat from the hot wall to the core of the duct by entraining fluid from the main stream. A region of low heat transfer is predicted immediately downstream of the rib, which is caused by the presence of secondary trapped eddies. Further downstream the heat transfer from the wall is gradually enhanced in the primary recirculation zone and reaches a maximum around the point of reattachment, where the surface shear is maximum. The WMLES were not able to predict accurately the peak in heat transfer just before attachment. Figure 2.7(d) shows normalized Nusselt number variation in the region upstream of the U-bend (Pitch number 13,14 and 15) and fig. 2.7(e) shows the region downstream of the bend (Pitch number 20, 21 and 22). It can be observed that heat transfer augmentation in the regions shown is nearly 40% higher in second pass compared to the first pass. Also, heat transfer augmentation decreases with distance away from the U-bend in both the passes, though the fall is more rapid in second pass than the first pass. Reasonable agreement with experiments is observed for all heat transfer results.

2.5 Conclusions

Predicting complex flow physics and heat transfer in internal cooling passages of turbine blades presents significant challenges. Due to their ease of use and fast turnaround time for calculations, RANS simulations with various turbulence models, are current industry standard. These turbulence models involve lot of approximations and hence are seldom able to accurately reproduce the range of physics encountered in the serpentine internal cooling ducts. Though LES studies have been quite successful in predicting turbulent flow and heat transfer in these geometries, the grid requirements for wall resolved LES still limit their applications to relatively simpler geometries. The wall model approach results in significant saving in computational resources by virtue of the coarser grids that can be used in wall bounded flows. The present study validates the use of WMLES for predicting flow and heat transfer with experiments and elucidates on the detailed flow physics and heat transfer in two pass duct.

2.6 Acknowledgments

The calculations were performed on Virginia Tech's Terascale computing facility, System-X and NICS computing facility, Nautilus. The authors would like to thank the Commonwealth of Virginia and Rolls-Royce for their support and especially N. Wagers, B. Barker, and H. Kwen for thoughtful discussion, analysis and advice.

References

[1] Prakash, C., and Zerkle, R., 1995, "Prediction of Turbulent-Flow and Heat-Transfer in a Ribbed Rectangular Duct with and without Rotation," J Turbomach, 117(2), pp. 255-264.

[2] Jia, R., Saidi, A., Sunden, B., 2002, "Heat transfer enhancements in square ducts with V-shaped ribs of various angles," Proc. ASME Turbo Expo(30209).

[3] Liou, T. M., Chang, Y., and Hwang, D. W., 1990, "Experimental and Computational Study of Turbulent Flows in a Channel with 2 Pairs of Turbulence Promoters in Tandem," J Fluid Eng-T Asme, 112(3), pp. 302-310.

[4] Acharya, S., Dutta, S., Myrum, T. A., and Baker, R. S., 1993, "Periodically Developed Flow and Heat-Transfer in a Ribbed Duct," Int J Heat Mass Tran, 36(8), pp. 2069-2082.

[5] Saidi, A., and Sunden, B., 2001, "On prediction of thermal-hydraulic characteristics of square-sectioned ribbed cooling ducts," J Turbomach, 123(3), pp. 614-620.

[6] Ooi, A., Iaccarino, G., Durbin, P. A., and Behnia, M., 2002, "Reynolds averaged simulation of flow and heat transfer in ribbed ducts," Int J Heat Fluid Fl, 23(6), pp. 750-757.

[7] Liou, T. M., and Hwang, J. J., 1992, "Turbulent Heat-Transfer Augmentation and Friction in Periodic Fully-Developed Channel Flows," J Heat Trans-T Asme, 114(1), pp. 56-64.

[8] Liou, T. M., Hwang, J. J., and Chen, S. H., 1993, "Simulation and Measurement of Enhanced Turbulent Heat-Transfer in a Channel with Periodic Ribs on One Principal Wall," Int J Heat Mass Tran, 36(2), pp. 507-517.

[9] Iacovides, H., and Raisee, M., 2001, "Computation of flow and heat transfer in two-dimensional rib-roughened passages, using low-Reynolds-number turbulence models," Int J Numer Method H, 11(2-3), pp. 138-155.

[10] Sleiti, A. K., Kapat, J.S., 2004, "Comparison between EVM and RSM turbulence models in predicting flow and heat transfer in ribroughened channels," Proceedings of the 2004 ASME Heat Transfer/Fluids Engineering Summer Conference.

[11] Rigby, D. L., 1998, "Prediction of heat and mass transfer in a rotating ribbed coolant passage with a 180 degree turn," International Gas Turbine and Aeroengine Congress and Exhibition(98-GT-329).

[12] Menter, F. R., 1992, "Improved two-equation k–w turbulence models for aerodynamic flows," NASA Technical Memorandum(103975).

[13] Menter, F. R., 1993, "Zonal Two Equation k–w Turbulence Models for Aerodynamic Flows," AIAA(93), p. 2906.

[14] Murata, A., and Mochizuki, S., 2001, "Comparison between laminar and turbulent heat transfer in a stationary square duct with transverse or angled rib turbulators," Int J Heat Mass Tran, 44(6), pp. 1127-1141.

[15] Watanabe, K., Takahashi, T., 2002, "LES simulation and experimental measurement of fully developed ribbed channel flow and heat transfer," Proceedings of the ASME Turbo Expo.

[16] Tafti, D. K., 2005, "Evaluating the role of subgrid stress modeling in a ribbed duct for the internal cooling of turbine blades," Int J Heat Fluid Fl, 26(1), pp. 92-104.

[17] Abdel-Wahab, S., and Tafti, D. K., 2004, "Large eddy simulation of flow and heat transfer in a 90 deg ribbed duct with rotation: Effect of Coriolis and centrifugal buoyancy forces," J Turbomach, 126(4), pp. 627-636.

[18] Abdel-Wahab, S., Tafti, D.K., 2004, "Large eddy simulation of flow and heat transfer in a staggered 45 degree ribbed duct," Proceedings of the ASME Turbo Expo.

[19] Sewall, E. A., Tafti, D.K., 2004, "Large eddy simulation of the developing region of a stationary ribbed internal turbine blade cooling channel," Proceedings of the ASME Turbo Expo.

[20] Sewall, E. A., Tafti, D.K., 2004, "Large eddy simulation of the developing region of a rotating ribbed internal turbine blade cooling channel," Proceedings of the ASME Turbo Expo.

[21] Spalart, P. R., Jou, W.H., Streletes, M., Allmaras, S.R., 1997, "Comments on the feasibility of LES for wings and a hybrid RANS/LES approach," Conf. on DNS/LES.

[22] Viswanathan, A. K., and Tafti, D. K., 2005, "Detached Eddy Simulation of turbulent flow and heat transfer in a ribbed duct," J Fluid Eng-T Asme, 127(5), pp. 888-896.

[23] Patil, S., and Tafti, D., 2012, "Wall modeled large eddy simulations of complex high Reynolds number flows with synthetic inlet turbulence," Int J Heat Fluid Fl, 33(1), pp. 9-21.

[24] Sewall, E. A., Tafti, D. K.,Graham, A. B.,Thole, K. A., 2006, "Experimental validation of large eddy simulations of flow and heat transfer in a stationary ribbed duct," Int J Heat Fluid Fl, 27(2), pp. 243-258.

[25] Najjar, F. M., and Tafti, D. K., 1996, "Study of discrete test filters and finite difference approximations for the dynamic subgrid-scale stress model," Phys Fluids, 8(4), pp. 1076-1088.

[26] Lilly, D. K., 1992, "A Proposed Modification of the Germano-Subgrid-Scale Closure Method," Phys Fluids a-Fluid, 4(3), pp. 633-635.

[27] Cabot, W., Moin, P., 1999, "Approximate wall boundary conditions in the large eddy simulation of high Reynolds number flow," Flow, Turbulence and Combustion(63), pp. 269–291.

[28] Kays, W. M., 1992, "Turbulent Prandtl number–where we are?," Max Jacobs Memorial Award Lecture(1-12).

[29] Tafti, D. K., 2001, "GenIDLEST – A scalable parallel computational tool for simulatingcomplex turbulent flows," Proc. ASME Fluids Engineering Division, 256.

[30] Patil, S., Abraham, S., Tafti, D., Ekkad, S., Kim, Y., Dutta, P., Moon, H. K., and Srinivasan, R., 2011, "Experimental and Numerical Investigation of Convective Heat Transfer in a Gas Turbine Can Combustor," J Turbomach, 133(1).

[31] Patil, S., Tafti, D., 2013, "Large-Eddy Simulation With Zonal Near Wall Treatment of Flow and Heat Transfer in a Ribbed Duct for the Internal Cooling of Turbine Blades," Journal of Turbomachinery, 135(3), p. 031006.

[32] Shah, A., and Tafti, D. K., 2007, "Transport of particulates in an internal cooling ribbed duct," J Turbomach, 129(4), pp. 816-825.

[33] Sewall, E. A., and Tafti, D. K., 2008, "Large eddy simulation of flow and heat transfer in the developing flow region of a rotating gas turbine blade internal cooling duct with coriolis and buoyancy forces," J Turbomach, 130(1).

[34] Rau, G., Cakan, M., Moeller, D., and Arts, T., 1998, "The effect of periodic ribs on the local aerodynamic and heat transfer performance of a straight cooling channel," J Turbomach, 120(2), pp. 368-375.

[35] Viswanathan, A. K., and Tafti, D. K., 2006, "A comparative study of DES and URANS for flow prediction in a two-pass internal cooling duct," J Fluid Eng-T Asme, 128(6), pp. 1336-1345.

[36] Han, J. C., Chandra, P. R., and Lau, S. C., 1988, "Local Heat Mass-Transfer Distributions around Sharp 180 Deg Turns in 2-Pass Smooth and Rib-Roughened Channels," J Heat Trans-T Asme, 110(1), pp. 91-98.

Chapter 3

Sand Transport in a Two Pass Internal Cooling Duct with Rib Turbulators[2]

Jet engines often operate under dirty conditions where large amounts of particulate matter can be ingested, especially, sand, ash and dirt. Particulate matter in different engine components can lead to degradation in performance. The focus of this study is to investigate the sand transport and deposition in the internal cooling passages of turbine blades.

A two pass stationary square duct with rib turbulators subjected to sand ingestion is studied using Large Eddy Simulations (LES). Each pass has ribs on two opposite walls and aligned normal to the main flow direction. The rib pitch to rib height (*P/e*) is 9.28, the rib height to channel hydraulic diameter (e/D_h) is 0.0625 and calculations have been carried out for a bulk Reynolds number of 25,000. Particle sizes in the range 0.5-25 μm are considered, with the same size distribution as found in Arizona Road Dust (medium). Large Eddy Simulation (LES) with a wall-model is used to model the flow and sand particles are modeled using a discrete Lagrangian framework.

Results quantify the distribution of particle impingement density on all surfaces. Highest particle impingement density is found in the first quarter section of the second pass after the 180^{o} turn, where the recorded impingement is more than twice that of any other region. It is also found

[2] A part of this chapter is reproduced from published work in International Journal of Heat and Fluid Flow, Volume 46, pp 158-167, with permissions from Elsevier

that the average particle impingement per pitch is 28% higher in the second pass than the first pass. Results show lower particle tendency to impact the region immediately behind the rib in the first pass compared to the second pass where particle impingement is more uniform in the region between two ribs. The rib face facing the flow is by far is the most susceptible to impingement and hence deposition and erosion. The results of this simulation are compared to experiments conducted on an identical two pass geometry with Arizona Road Dust particles. The numerical predictions showed good qualitative agreement with experimental measurements. These results identify the damage prone areas in the internal cooling passages of a turbine blade under the influence of sand ingestion. This information can help modify the geometry of the blade or location of film cooling holes to avoid hole blockage and degradation of heat transfer at the walls.

3.1 Introduction

Jet engines operating under dirty conditions are exposed to fine particulate matter such as sand, ash and dirt. This particulate matter can cause severe erosion of compressor blades and when exposed to high temperatures can soften and stick to turbine components in the hot gas path. Large amounts of particles can be ingested at takeoff and landing when engines are running at full power and are in ground proximity[1]. For an aircraft flying through volcanic dust clouds, particles can also be ingested at cruising altitudes [2]. Operation in these environments has led to serious aircraft accidents due to jet engine failures[3]. The problem of particulate ingestion in the engine has worsened with the use of high bypass ratio turbofan engines [4]. According to studies by Edwards and Rouse[5], high sand ingestion can reduce engine stability by eroding blade profiles and lowering the compressor efficiency, as a result of which the line of operation is closer to the surge line. The operating line also rises as a result of decrease in turbine efficiency or a reduction in nozzle throat due to glazing.

Different aspects of the problem of sand and volcanic ash ingestion have been studied in the literature, with the majority of the work focused on erosion and deposition of particles on a wide range of materials and under different operating conditions.

Erosion on blade surfaces and advanced coatings has been well documented by Hamed[1], who tested the impact of aluminum oxide, fly ash, quartz, sand and chromite particles on different blade materials and coatings for a range of temperatures from ambient to 704 ^{o}C. Harris[6] examined a number of natural dust samples and observed that quartz is usually the most abundant erosive constituent, often above 70% by weight. Hamed and Tabakoff [7] showed that the volcanic ash causes four times more damage than quartz particles. Tabakoff et al.[8] conducted experiments in an erosion wind tunnel at temperatures as high as 2000 ^{o}F, to investigate high temperature effects on the rate of erosion. Sand ingestion was shown to affect leading edge of rotor blades, blade surfaces and increase surface roughness[9]. While the transport of sand and ash particles in the flow path is similar, they might result in different failure modes. Finnie[10] studied the wear mechanism on ductile and brittle surfaces and concluded that the flow field and the vane surface properties influence the amount of erosion on the surface. Richardson et al.[11] showed that the erosion effects are more pronounced on the outer 50% of the span of the high pressure compressor blade. Tabakoff and Sugiyama[12] used laser Doppler velocimetry to study the particle surface interaction and observed that the impact angle was the primary factor affecting the restitution ratio. Ghenaiet et al.[13] observed a 6-10% loss in adiabatic efficiency of an axial fan for 6 hours of sand ingestion. Schmucker and Schaffer[14] reported that erosion lead to 1% loss in tip clearance leading to a 7.5% reduction in surge margin and a 2% loss in efficiency.

Particle deposition in turbomachinery has also been extensively studied. Kim et al.[2] conducted experiments investigating the effects of volcanic ash on turbine components and found that film cooling holes are susceptible to deposition and clogging. Dunn et al.[15] also reported that particulate deposition can clog film cooling holes and hence deposition is a major issue for modern aircraft engines. Walsh et al.[16] studied the effect of sand ingestion on film cooling hole blockage, using a leading edge coupon over a range of sand particle size, particle loading and metal temperatures. Metal temperatures were shown to be the most important parameter for particle deposition. At temperatures above 1000 ^{o}C, sand particles started melting and promoted blocking of cooling holes. Land et al.[17] investigated a double walled cooling design to reduce sand blockage. It was found that impingement air-flow holes and staggered arrangement of cooling holes could aid in breaking up of larger particles to pass through cooling holes. El-Batsh[18] developed a sticking model to investigate particle sticking and detachment on turbine blades. The model was used for a numerical investigation of the effect of ash particle deposition on the flow field through turbine cascades. This model was further modified and calibrated to match experimental results by Ai et al.[19], for their ash deposition study on a 45^{o} inclined flat plate with film cooling. Tafti et. al.[20] proposed a sticking model using the coal ash composition to determine the sticking probability of ash particles. More recently, Brun et al.[21], numerically investigated sand transport over a NACA 009 airfoil and a high speed centrifugal compressor. Comparison with experiments showed that the semi-empirical model predicted particle impact locations with a miss rate of approximately 20%.

The presence of particulates in ingested air affects the three major components of jet engines: compressor, combustor and turbine. The blade damage is possible through direct impingement of large particles and even by recirculation of fine particles in the secondary flows through the blade passage.[22] While many previous studies have investigated the effect of particulates on compressors [23-30], the focus of the present work is to study the effect of sand transport in the internal cooling ducts of turbine blades. Experiments by Schneider et al.[31] showed that even with a filter upstream of the turbine, ingested particles can reach the internal air cooling passages of turbine blades. Cooling air which is bled from the compressor can carry along significant amounts of sand particles to the internal cooling passages. These can deposit in cooling passages and also clog film cooling holes, leading to degradation in cooling performance and blade metal failure. The problem is exacerbated by ribbed serpentine cooling passages which are dominated by recirculation regions and secondary flows, making them more susceptible to deposition.

The objective of current study is to understand sand transport in a two pass internal cooling duct with rib turbulators. An effort is made to answer the following questions:

1. How do sand particles impinge the walls and ribs in a two pass duct?
2. Which regions in the two pass duct are most prone to erosion and deposition under prolonged sand ingestion?

3.2 Methodology

The solution methodology used to solve for particle transport in the two pass duct has two components. The fluid transport in the two pass duct configuration is computed using LES with a wall model to limit the computational time. Second, a Lagrangian tracking algorithm is used to track individual sand particles which are injected in the flow field. In this section the governing equations are discussed for the carrier phase and dispersed phase along with details of computational model, flow conditions and sand particle properties.

3.2.1 Carrier phase.

The turbulent flow field is simulated using Wall Modeled Large Eddy Simulations (WMLES) with a conservative finite volume code, Generalized Incompressible Direct and Large Eddy Simulations of Turbulence (GenIDLEST). The governing transport equations for the carrier phase (fluid) are discretized using a second-order central (SOC) difference scheme on a nonstaggered grid topology. The SOC discretization has been shown to be suitable for LES computations due to its minimal dissipation. The Cartesian velocities and pressure are calculated and stored at the cell center, whereas contravariant fluxes are stored and calculated at cell faces. The discretized continuity and momentum equations are integrated using a projection method. The subgrid stresses are modeled using the Dynamic Smagorinksy Model (DSM)[32].The temporal advancement is performed in two steps, a predictor step to compute intermediate velocities, and a corrector step, which calculates the updated velocity at the new time step by satisfying discrete continuity. The computer program, GenIDLEST, used for the current study has been applied and validated for numerous complex heat transfer and fluid flow problems. Details about the algorithm, functionality, and capabilities can be found in[33], the wall model development in [34], and LES application to rib duct flow in[35]. Further, wall-modeled LES flow and heat transfer results in the two-pass ribbed duct geometry used in this paper are available in[36].

3.2.2 Dispersed Phase.:

The dispersed phase is modeled by following the trajectories of individual particles subjected to fluid forces in a Langrangian framework. The model is implemented in an unstructured multiblock, multiprocessor framework and the verification and validation in turbulent channel flow has been reported in[37, 38]. The following equations are used to track the particle velocity and location

$$m_p^* \frac{du_i^{*p}}{dt^*} = \sum F_i^{*p} \tag{1}$$

$$\frac{dx_i^{*p}}{dt^*} = u_i^{*p} \tag{2}$$

The typical forces acting on a particle are drag, gravitational forces, the Saffman lift [32] force caused by the shear of the surrounding fluid, added mass, pressure and viscous forces, Basset forces due to fluid acceleration, Magnus lift force due to particle rotation, and forces due to inter-particle collisions. For submicron sized particles, Brownian and thermophoretic forces which are a result of random molecular motion and temperature gradients, respectively, can also be important. For the range of particle size considered in this study (0.5-25μm), and for high density ratio of dispersed to carrier phase, the only significant forces are Stokes drag and gravitational forces[33]. Due to the low volume fraction of particles, inter-particle collisions and effect of particles on fluid motion are neglected [34]. It is also assumed that subgrid scales have negligible effect on particle transport [35, 36]. Lastly, in order to avoid additional complexity, the effect of material roughness is not considered during particle-wall interaction. Under the above assumptions, the simplified equation of motion of particles can be written as

$$\frac{du_i^{*p}}{dt^*} = -\frac{\rho_f^*}{\rho_p^*}\frac{3}{4}\frac{C_D}{d_p^*}\left|u^{*p} - u^{*f}\right|\left(u_i^{*p} - u_i^{*f}\right) \tag{3}$$

The drag coefficient C_D is given by Clift et al. [37] and is valid for particle Reynolds number up to 700

$$C_D = \frac{24}{\mathrm{Re}_p}(1 + 0.15\mathrm{Re}_p^{0.687}) \tag{4}$$

The particle Reynolds number is given by $|u^{*p} - u^{*f}|\, d_p^* / \nu$. The particle transport equation can be written in dimensionless form using the mean bulk velocity u_b^* and hydraulic diameter, D_h, as the characteristic velocity and length scale, respectively.

$$\frac{du_i^p}{dt} = -\frac{1}{St_p}(1 + 0.15\mathrm{Re}_p^{0.687})(u_i^p - u_i^f) \tag{5}$$

$$\frac{dx_i^p}{dt} = u_i^p \tag{6}$$

Where St_p is the particle Stokes number, which is the ratio of the particle time scale τ_p^* to the flow time scale, D^*/u_b^*

$$St_p = \frac{\tau_p^*}{D^*/u_b^*} = \frac{\rho_p^* d_p^{*2}/18\mu^*}{D^*/u_b^*} \tag{7}$$

The particle Stokes number gives an estimate as to how quickly a particle responds to the flow field [38]. Stokes number much larger than unity implies slow inertial response of the particle to the surrounding flow field, while particles with Stokes number much lower than unity respond almost instantaneously to the carrier phase, resulting in nearly identical particle and fluid velocity. The above particle transport equations are integrated in time using third-order Adams-Bashforth scheme, to advance the particle location [39]. The modeled coupling is one way from flow field to particles only.

3.2.3 Computational Model.

3.2.3.1 Geometry description

A simplified geometry for the two pass internal cooling duct is considered in the present study. The geometry is a U-shaped duct with square cross section as shown in Fig. 1. All dimensions are based on the characteristic length, the hydraulic diameter of the duct (width of square cross section, D_h = 0.0508m), as used in experiments. Each pass has ribs on two opposite walls and aligned normal to the main flow. Rib height (*e*) is $0.0625D_h$and pitch length (*P*) is $0.58D_h$and hence rib pitch to rib height ratio is 9.28. The first pass has 16 and the second pass has 14 equally spaced ribs. Each pass is $20D_h$ long and clearance between two passes is $0.25D_h$. The flow leaves the computational domain in the direction of the second pass, contrary to experiments, in which it turns at a right angle and leaves normal to the second pass.

3.2.3.2 Computational grid

The grid is constructed using a multi-block topology. Each rib unit is the section from center of one pitch to the next. In total, each rib unit is discretized into 38×68×64 cells (Fig. 2) and was divided into 7 blocks to facilitate parallel processing. The 180° bend was discretized into 64×68×144 cells and 9 blocks. The second pass has an outlet region which is around 5 hydraulic diameters long. Near wall grid spacing of an approximate y+ of 30 is used for the wall model, as used in our previous studies on a ribbed duct[40]. The total size of the grid is 5.8 million cells distributed over 153 blocks.

3.2.3.3 Boundary conditions

In the present study, the flow Reynolds number is 25,000, based on the mean velocity at the inlet and hydraulic diameter of the duct. The non-dimensional velocity at the inlet is set to unity and convective outflow boundary condition is used at the outlet. The duct inlet has a constant velocity profile normal to the boundary. Particles are injected in the inlet blocks uniformly with a frequency of 10,000 particles every 0.2 non-dimensional time units with 22 injections for 220,000 particles in total. Initially upon injection, the particle velocities are set to be the same as the fluid velocity. Particle size distribution (Figure 3.1) is identical to Arizona Road Dust obtained from Powder Technology Inc. Mean particle diameter is 1μm and standard deviation is 0.9μm. The range of particle diameters considered is 0.5μm-25μm, which corresponds to a Stokes number of 0.0003 to 0.75. From the particle size distribution obtained from Powder Technology, only 0.01% particles are larger than 25μm. As the main focus of this study is to look at the impingement pattern of the particles in the two pass duct, the particle wall collision is assumed to be perfectly elastic.

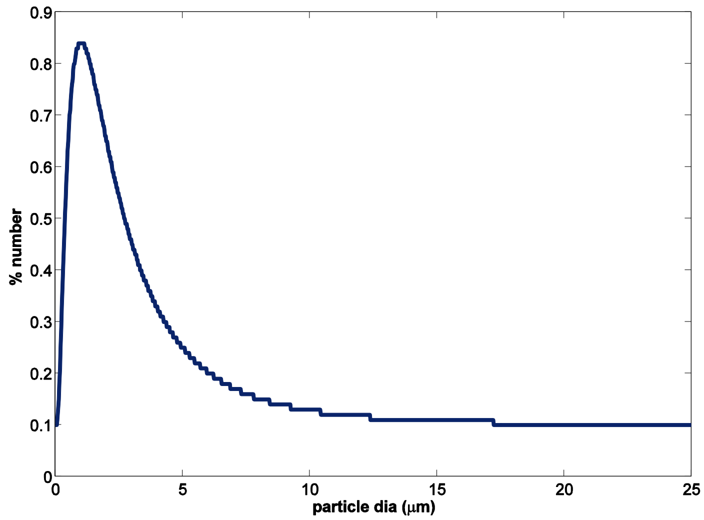

Figure 3.1 Particle size distribution

3.2.3.4 Solver control

The convergence criteria for the momentum and pressure are 1E-5 and 1E-5 respectively, at each time step. The time step is set at 2E-4. For every fluid time step, the particle transport equations are integrated through 5 sub-steps, for better resolution of particle trajectories. The flow is first allowed to develop and reach a statistically stationary state, which takes 20 non-dimensional time units. Then 10,000 particles are injected every 0.2 time units for 22 injections. The particles are tracked and the calculation is run until the last particle injected leaves the computation domain. Wall collision statistics are recorded during the run. The calculation was run on 153 processors with 2.0 GHz speed. For carrier phase only, one time unit takes 8-10 hours and with particles the same takes 12-14 hours. The calculations were run for approximately 50 time units, which took around 550 computational hours. Fluid time-averaged quantities are obtained by averaging the velocity field for 10 time units.

3.2.4 Experimental setup.

Experiments are conducted in an identical geometry at identical flow conditions. 3M™ Very High Tack Foam Tape is used on all surfaces except the ribs, to capture the particles impacting the walls. The tape is transparent and 0.020” thick. The two pass channel is assembled and installed into the test rig shown in figure 3.2. Bleed air is regulated through a sand blaster design where particles are fed from a hopper through a control valve and entrained in the air flow. Both air streams are regulated and metered to match the target Reynolds number. Then, 2.0 grams, approximately 47 million particles of Arizona Road Dust medium grade are injected and accelerated to the bulk flow speed in a 4ft long tube before entering the two pass channel.

The particles travel into the geometry and either pass through or impact a surface. If the particle impacts a surface that is taped, it is assumed that the adhesion force from the high tack tape will overcome the elastic rebound force stored during impact forcing the particle to stick to the tape. After running the experiment, the setup is carefully dissembled and high resolution images are taken of all the walls with the high tack tape on a black backdrop. Lighter areas indicate high sand impingement, darker areas low impingement. These images are compared directly to the CFD predicted impingement pattern.

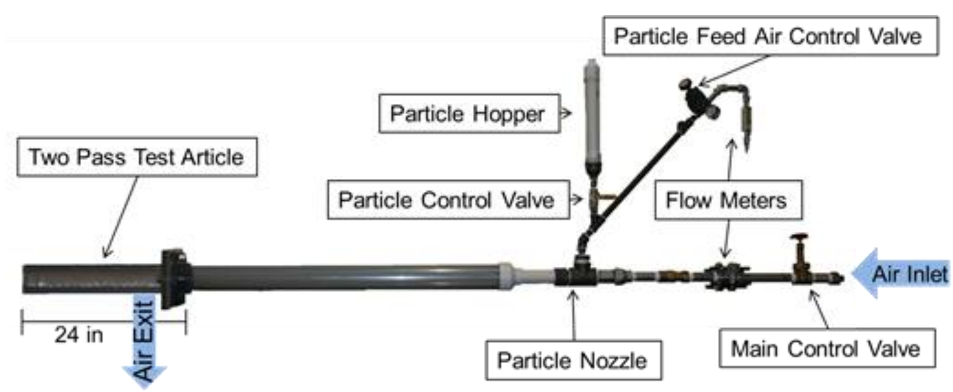

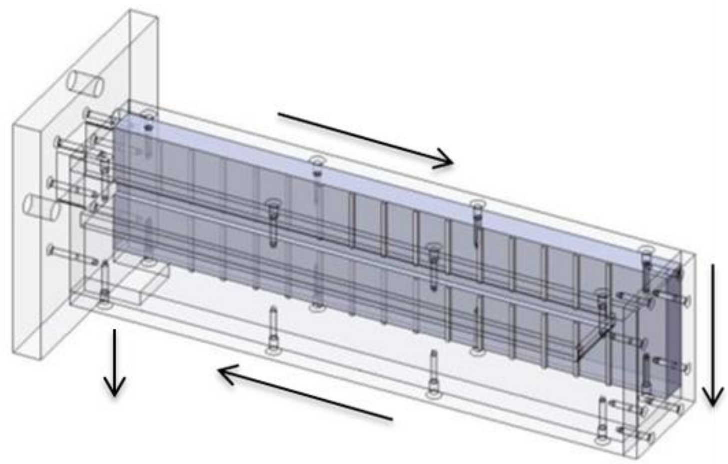

Figure 3.2 Experimental Setup (top), two pass section (bottom)

3.3 Results

In order to understand and analyze the particle transport and impingement pattern efficiently, it is important to look at the flow field that leads to the observed particle transport. In this section, first, the calculated flow field is discussed and second, the particle impingement pattern is presented. An effort is made to explain the observed particle impingement pattern based on the observed flow field.

3.3.1 Flow field.

Calculations of flow field in a fully developed and developing ribbed duct have been published before [38, 47]; the flow is fully developed after the fifth rib in the first pass. Figure 5 shows the mean streamline distribution at the mid-plane parallel to the ribbed wall. The flow begins to feel the presence of the 180o turn about 1D_h upstream of the last rib. At the upstream edge of the bend, a strong shear layer is formed due to considerable flow acceleration on the inside of the turn. A large recirculation zone is formed at the upstream corner as the bulk of the flow is pushed towards the downstream side of the bend. Similarly, a smaller recirculation region forms at the downstream outer corner. Flow separation at the tip of the dividing wall also leads to a recirculation zone. After impinging on the back wall of the bend, the flow impinges on the outer wall of the second pass while coming out of the bend

Figure 6(a) shows mean streamline pattern in a rib unit at a fully developed location (pitch number 10) in the first pass. Flow patterns observed by the earlier LES studies[41, 42], RANS modeling [43] and experiments [44] show a similar pattern. The mean flow is characterized by a leading edge eddy at the rib-wall junction, a recirculation zone at the top of the rib, a counter rotating eddy in the wake of the rib and the primary recirculation region behind the rib. The mean reattachment length is calculated as 4.8e compared to experimentally observed values 4.0e-4.25*e* (P/e=10,e/D_h=0.1). An important characteristic of ribbed duct flow is the presence of secondary flows, which have a large impact on the heat transfer augmentation on side walls. Identically, these secondary flows are expected to affect the particle transport to side walls leading to higher deposition and reduction in heat transfer augmentation.

These secondary flows are driven by the periodic flow disturbance caused by the ribs and the junction flow where the ribs meet the side wall [41]. In the vicinity of rib-sidewall junction, strong localized unsteady vortical structures are generated. Figure 6(b) shows contours of spanwise velocity in the vicinity of the rib-sidewall junction. Lateral impingement velocities as high as 18% are found in this region, indicating a strongly three dimensional flow. Except in the immediate vicinity of the rib, the secondary flow is weak. These unsteady structures have a large impact on low Stokes number particles, investigated in the current study.

Figure 7 shows the coherent structures (iso-vorticity) in the computational domain. The figure shows a large number of coherent structures and hence high turbulence intensity in the first half of the second pass after the 180^o turn. Highly turbulent flow in the second pass is consistent with previous studies on similar geometries [42, 45, 46] . The figure also shows that flow becomes essentially periodic after fifth rib in the first pass. These turbulent structures and hence turbulence intensity plays important role in the particle transport as discussed later.

3.3.2 Particle Transport.

In this section, the detailed particle impingement pattern is presented and compared with experimental results. Ribbed wall, sidewalls, and rib faces are discussed separately.

3.3.2.1 Ribbed wall

Ribbed walls by far are the most important surfaces for heat transfer augmentation. Any particle deposition and damage on ribbed wall will cause severe loss in cooling performance of the internal cooling duct. In figure 3.3, particle impingement patterns (n is the number of particle collisions) are presented at three different sections; near bend region, fully developed region, and inlet/outlet region, in the two passes along with experimental results. Left hand side figures show experimental results, in which light areas indicate high sand impingement and darker areas indicate low sand impingement. It is observed that particle impingement is similar on both the ribbed walls, so only one wall is shown for analysis. For both CFD and experiments, Fig. 3.3(a), shows high particle impingement in the downstream end wall corner of the bend (pitch # 18). This is the region where the turning flow impinges on the end wall and the smooth side wall. Though there is small recirculation in the corner, direct impingement of flow is essentially responsible for higher number of particle impacts. Higher particle impingement is also observed in the region where the flow enters the bend just downstream of first pass (pitch # 16).

If the particle impacts in the four pitches upstream of the bend are compared with the same downstream of the bend, it is found that particle impingement is more uniform in between two ribs, in the second pass, while in the first pass particles show lower tendency to impact the region immediately behind the rib. The higher impingement immediately behind the rib in the second pass (pitch 19 &20) is due to higher turbulence in this region, accompanied by stronger secondary flows due to the turning flow, which results in smaller particles being easily entrained into the turbulent eddies. Also, higher particle impingement is seen near the sidewalls in pitch 15 in the first pass because of the turning flow.

Numerical computations are in good agreement with the experiments except in the region in front of the first rib where flow enters the second pass (pitch # 18). While the experiments show high levels of deposition in this region, the CFD does not. One reason for this discrepancy could

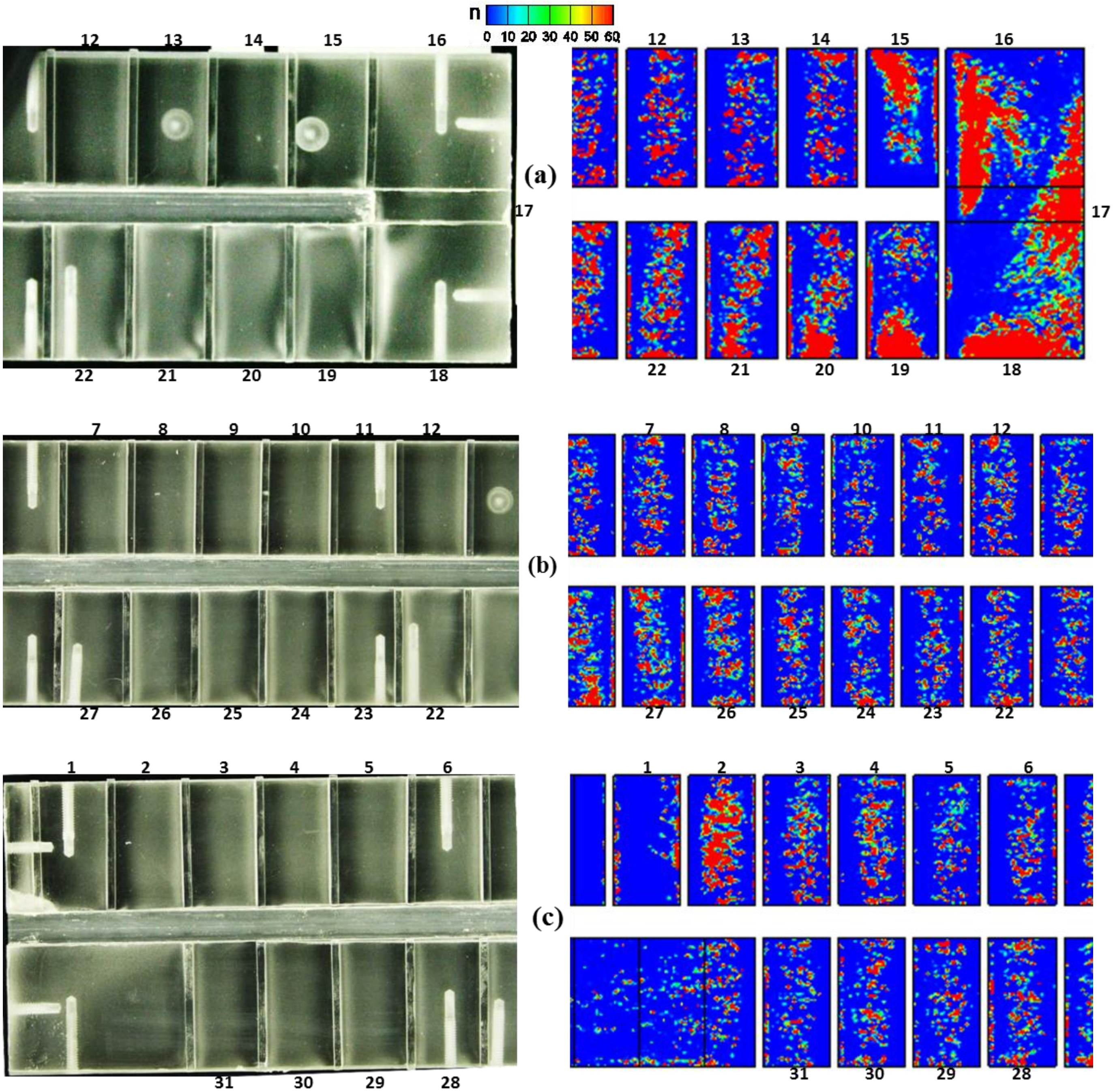
n
0 10 20 30 40 50 60
(a)
12 13 14 15 16
17
22 21 20 19 18
(b)
7 8 9 10 11 12
27 26 25 24 23 22
(c)
1 2 3 4 5 6
31 30 29 28

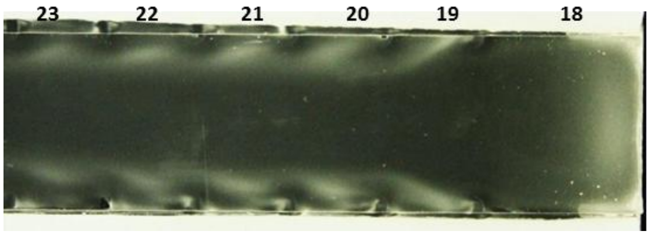

(d)

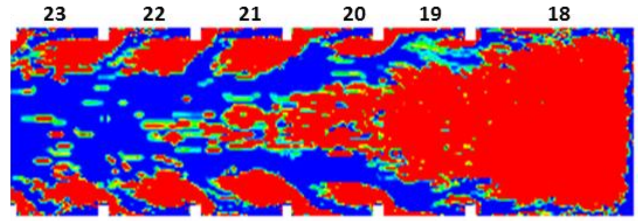

Figure 3.3 Particle impingement recorded in simulations at the ribbed wall, at different sections, experimental on left and CFD on right (a) 180^{o} turn (b) mid-section (c)

be that the flow turns much faster through the U-bend in the experiments than predicted by the numerical model. Another possible reason could be due to the deposition and subsequent erosion of particles from the upstream corner of the bend in the experiments. Again, regions directly downstream of the ribs and near the outer wall in pitches 19 through 22 show higher deposition in the experiment that is not perceptible in the CFD. This could be caused by the presence of more particles in the recirculation region immediately downstream of the ribs due to quicker turning of the flow compared to CFD. Figure 3.3(b) shows the mid-section of both the passes. Again, higher and more uniform impingement is observed in the second pass compared to the first pass where the regions immediately behind the ribs are nearly free from particle impingement. In the inlet/exit regions, figure 3.3(c), similar impingement patterns are observed in the experiments and CFD, except just next to the inlet or exit. This is because in the CFD, the particles are uniformly distributed at the inlet during injection with uniform velocities, while they are not uniform in the experiments.

3.3.2.2 Smooth side walls

Not much particle impingement is observed on the smooth side wall in the first pass and the divider walls, except in small regions in the vicinity of the rib-sidewall junctions. The sidewall in the second pass experiences significantly high particle impingement due to direct flow impingement of turning flow in the bend. Distinct patterns of particle impingement are observed at the rib-sidewall junctions at all the sidewalls. This particle impingement is a manifestation of high secondary flows causing spanwise velocities as high as 18% of the mean bulk velocity. Very small particles (low Stokes number) are very sensitive to the flow field and hence easily carried to the walls by these highly unsteady three dimensional structures. Also, very high particle impingement is observed at the side wall toward the downstream end of the bend, due to direct flow impingement at this wall. Some disagreement between numerical and experimental results can be seen in pitch number 18 and 19, Fig. 3.3(d). This could be due to CFD predicting a slower turning of the flow in the bend compared to experimental observation. The more gradual turning of the flow in the CFD leads to direct flow impingement on a larger area on the sidewall compared to experiments in which the flow turns quickly without directly impacting the sidewall, after pitch number 18.

3.3.2.3 Ribs

Very high particle impingement is observed on the rib faces facing the flow in both the passes. In addition, the trailing side of the rib also experiences particle impingement (Figure 3.4). Particles impinging the back of the rib are mostly a result of them bouncing off of the front face of the following rib with enough momentum to travel backward against the flow[47]. Comparatively higher impingement is seen at the back of the rib in the second pass than the first pass. This is due to the higher velocities of the particles coming out of the bend and also due to increased transport by turbulent eddies, both of which combine to increase particle impingement at the trailing face of ribs in the second pass. Additionally, the top surface of the ribs did not experience much impingement. Sticky tape was not used on rib faces to capture particle impingement and hence no comparisons can be made with experiments.

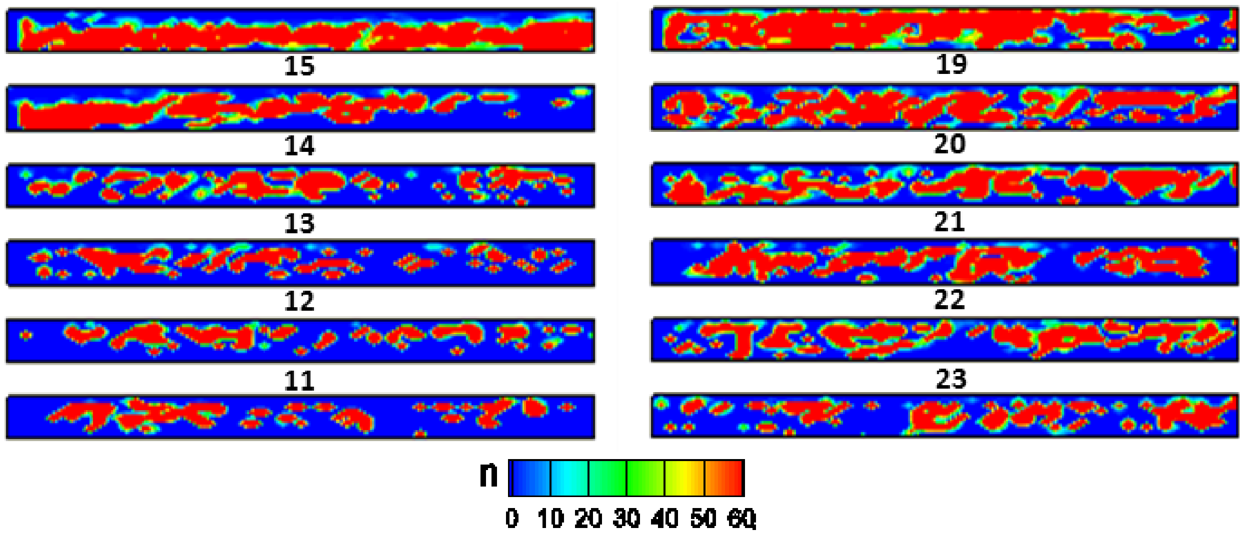

Figure 3.4 Particle impingement on rib back faces in 6 ribs upstream and downstream of the bend (Pitch # shown)

Overall, much higher impingement is seen in the second pass compared to the first pass due to highly turbulent flow in the region. Figure 3.5 shows the number of particle impacts on all the surfaces per pitch normalized by the area and total number of particles injected at the inlet. Highest particle impingement density is found in the first quarter section of the second pass after the 180^{o} turn, where the recorded impingement is more than twice that of any other region. It can also be seen that the average particle impingement per pitch is 28% higher in the second pass than the first pass. Rib faces are by far the most susceptible to impingement, though in the second pass rib backs are also exposed to significant particle impingement. Particle impacts in the first pass is more or less same in each pitch, while the impingement decreases in the second pass from bend to the outlet. This is a result of the combination of two major flow features in this region; the direct flow impingement on the walls and high turbulence. The effect of both of these mechanisms decreases as we move downstream of the bend.

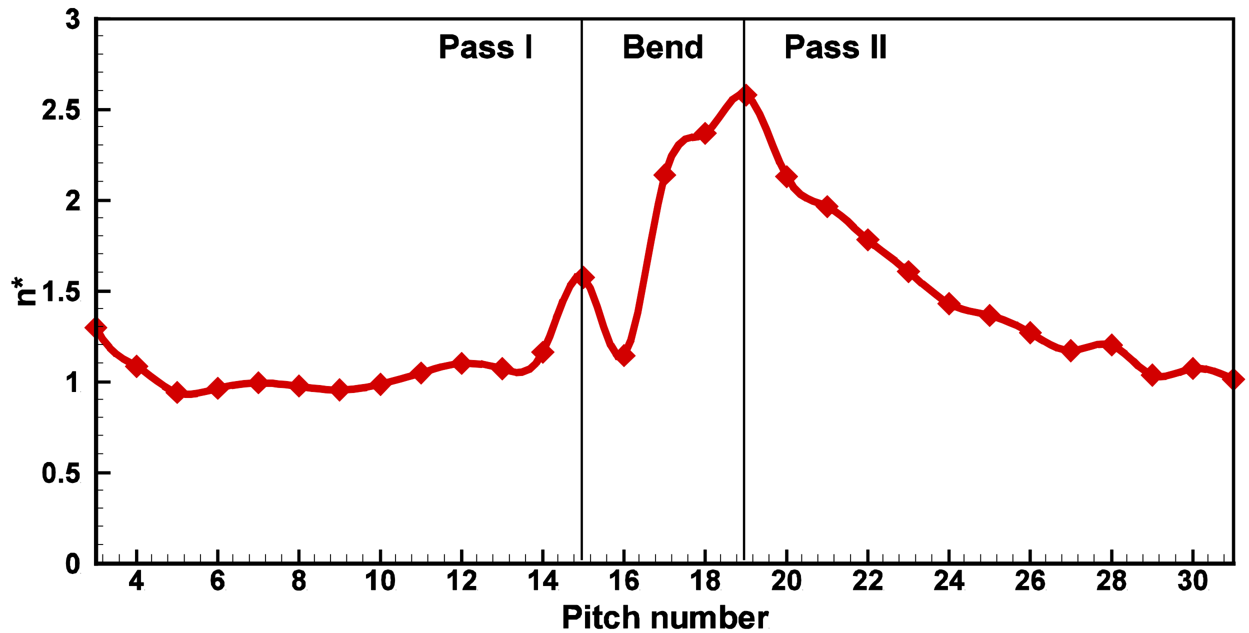

Figure 3.5 Total number of particle impacts per pitch normalized by pitch area and number of particles injected (CFD results)

3.4 Wall collision Model and Particle size effects

The above comparisons used perfectly elastic particle-wall collisions in the computational model to simulate experiments which used an adhesive tape to capture the particles (perfectly inelastic). To simulate the inelastic wall collisions, the CFD calculations were also performed with the perfectly inelastic particle wall collisions. Two separate calculations were carried out for low Stokes number of 0.2 (d_p^* = 12 microns) and very high Stokes number of 2.0 (d_p^* = 41 microns) to compare the effect of Stokes number and hence particle size on the particle transport and impingement. The number of particles injected was still restricted to 220,000 to limit the computational time. For *St* =0.2, 76.5% of all the injected particles are deposited in the two passes while for *St* = 2.0, 82.6% of particles are deposited. For *St* = 0.2, 26.9% of injected particles are deposited in the first pass, 44.3% in the bend, and 5.3% in the second pass. It can be determined from this that 18.4% particles that enter the second pass are deposited, which is less than the 26.9% in the first pass. For *St* = 2.0, 12.9% of the injected particles are deposited in the first pass, 69.4% in the bend and 0.3% in the second pass, which implies that only 1.7% of the particles entering the second pass are deposited. This result is counter to the observations made for perfectly elastic collisions at the wall and primarily is a result of the less number of particles reaching the second pass for the results to be statistically accurate. Figure 3.6 shows the number of particles deposited on all the surfaces per pitch *normalized by the number of particles entering the pitch* for the two Stokes numbers. For *St* = 0.2, a fully-developed deposition fraction is established very quickly in the first pass, whereas *St* = 2.0 particles take about 10-11 pitches to exhibit a fully-developed behavior. This is expected for the larger diameter particles which take longer to respond to flow perturbations. It is also observed that a larger fraction of the smaller diameter particles deposit in the first pass and in pitch 18, while a smaller fraction of the larger particles deposit in the first pass with a large deposition fraction in pitch 16 of the bend. Endwall deposition in the bend is shown in more detail in figure 3.7. The low Stokes number particles are able to negotiate the sharp turn better than the heavier particles which directly impinge the endwall. For this reason, a much large fraction of particles of the high Stokes number particles are deposited in the bend. For the same reason, the particle impingement is more uniform between the ribs for lower Stokes number.

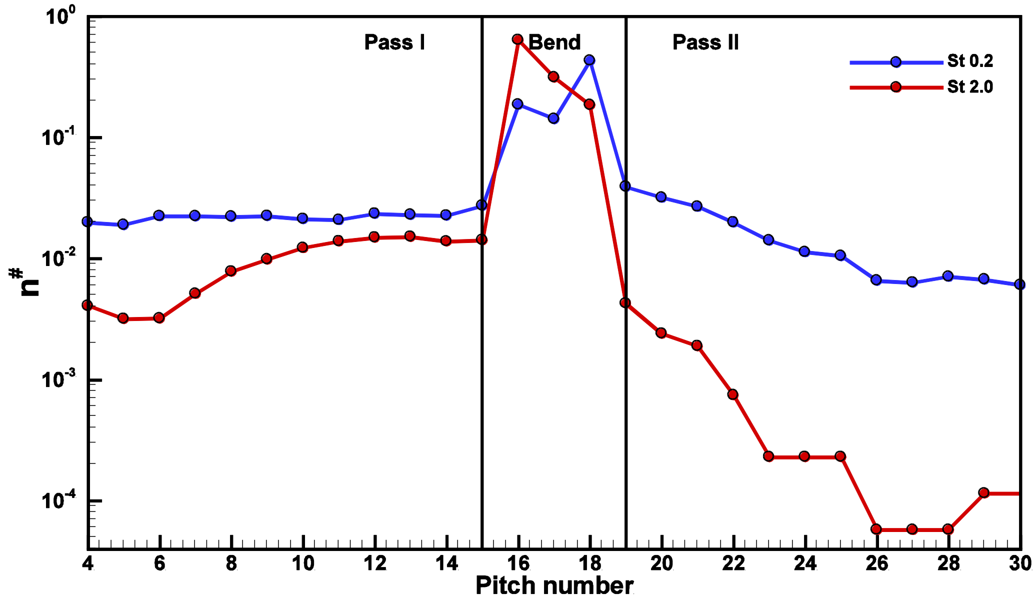

Figure 3.6 Number of particles deposited on all the surfaces per pitch normalized by the number of particles entering the pitch (inelastic collisions, CFD)

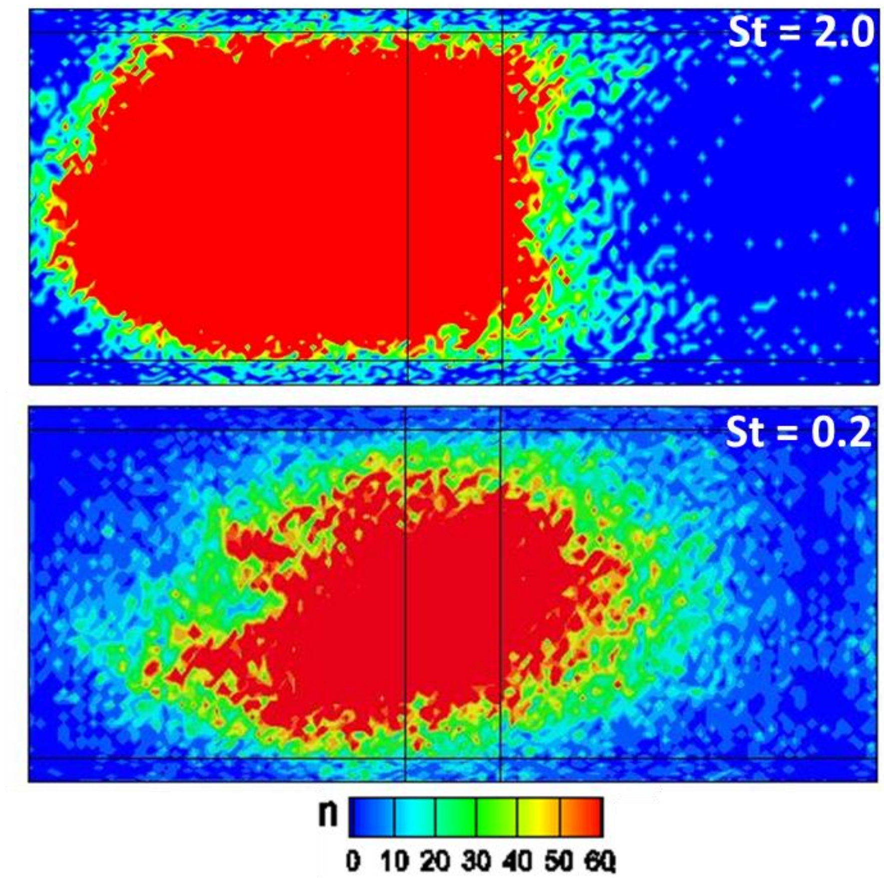

Figure 3.7 Endwall deposition for two Stokes numbers (inelastic collisions, CFD)

Since nearly 80% of the injected particles are captured in the first pass and the bend region with a perfectly inelastic wall collision model, a significantly higher particle loading (more than 1 million particles) would be required to get statistically significant number of particles in the second pass. In lieu of this, the computations have used perfectly elastic collisions, which maintain the same population of particles throughout the channel, to emulate the deposition process in the two pass channel by counting the number of impacts on a surface as an indication of the deposition. Bearing in mind that the actual process of deposition will depend on many factors and will neither be perfectly elastic nor perfectly inelastic but somewhere in between the two idealizations, the current study is a good indicator of deposition patterns and propensity.

3.5 Conclusions

The paper investigates sand transport in the internal cooling passages of a turbine blade. LES calculations are performed for bulk Reynolds number of 25,000 to investigate particle transport in a two pass channel with rib turbulators. Particle sizes in the range 0.5-25 μm are considered, with the same size distribution as found in Arizona Road Dust (medium). Particle impingement patterns obtained from CFD are compared with the experimental data. It is found that the sand particles in the size range considered in the current study tend to follow the flow field quite closely. From the above analysis it is clear that the first quarter of the second pass is most susceptible to deposition and erosion, as the highest particle impingement is observed in this region. All side-walls experience minimal particle impingement except the outer side-wall in the second pass. Average particle impingement per pitch is 28% higher in the second pass compared to the first pass. Rib faces are exposed to particle impingement in both the passes, while rib backs only experience higher impingement in the second pass due to high turbulence intensity and secondary flows. The particle impingement pattern is more uniform in the first pass compared to second pass, as is the case with flow field. Through a separate study, it is also concluded that particle size and wall collision model are important in determining the particle transport and deposition. While larger particle impacts are through direct particle impingement, smaller particles tend to follow the flow. These results identify the damage prone areas in the internal cooling passages of a turbine blade under the influence of sand ingestion. This information can help modify the geometry of the blade or location of film cooling holes to avoid hole blockage and degradation of heat transfer at the walls. For example, a bend geometry with gradual turning can reduce the direct flow impingement on the smooth side wall in the second pass. Similarly, if possible, the placement of cooling holes in the vicinity of the downstream end of the bend, should be avoided to prevent hole clogging. Though this study is simplified under the assumptions of perfectly elastic wall collisions and no heat transfer, it is nevertheless an important step in understanding the effect of particulate transport in serpentine ribbed internal cooling passages.

3.6 Acknowledgments

The calculations were performed on Virginia Tech's Terascale computing facility, System-X and NICS computing facility, Nautilus. The authors would like to thank the Commonwealth of Virginia and Rolls-Royce for their support and especially Dr. V. Rajendran, N. Wagers, B. Barker, and H. Kwen for thoughtful discussion, analysis and advice.

References

[1] Hamed, A., Tabakoff, W., and Wenglarz, R., 2006, "Erosion and deposition in turbomachinery," J Propul Power, 22(2), pp. 350-360.

[2] Kim, J., Dunn, M. G., Baran, A. J., Wade, D. P., and Tremba, E. L., 1993, "Deposition of Volcanic Materials in the Hot Sections of 2 Gas-Turbine Engines," J Eng Gas Turb Power, 115(3), pp. 641-651.

[3] Tabakoff, W., 1987, "Compressor Erosion and Performance Deterioration," J Fluid Eng-T Asme, 109(3), pp. 297-306.

[4] Alge T. L., M. J. T., 1994, "Modern Transport Engine Experience with Environmental Ingestion Effect," Propulsion and Energetic Panel (PEP), Symposium, Rotterdam, Netherlands. AGARD.

[5] Edwards, V. R., Rouse, P.L., 1994, "U.S. Army Rotorcraft Turboshaft Engines Sand & Dust Erosion Considerations," AGARD, Erosion, Corrosion and Foreign Object Damage Effects in Gas Turbines, Quebec, Canada.

[6] P.K, H., 1996, "Erosion in Centrifugal Compressor impellers," PhD Thesis Cranfield University.

[7] Hamed, A., Tabakoff W, 1990, "Jet Engines Performance Deterioration," International Congress of Fluid Mechanics 3 RD Proceeding, 2.

[8] Tabakoff, W., Grant, G., Ball, R., 1974, "An Experimental Investigation of Certain Aerodynamic Effects on Erosion," AIAA, Paper No. 74-639.

[9] Grant, G., and Tabakoff, W., 1975, "Erosion Prediction in Turbomachinery Resulting From Environmental Particles," J Aircraft, 12(5), pp. 471-478.

[10] Finnie, I., 1960, "Erosion of surfaces by wear," Wear, 3, pp. 87-103.

[11] Richardson, J. H., Sallee, G. P., Smakula, F. K., 1979, "Causes of High Pressure Compressor Deterioration in Service," Proceedings of AIAA/SAE/ASME Joint Propulsion Conference, Las Vegas, NV.

[12] Tabakoff, W., Sugiyama Y. , 1980, "Experimental Methods of Determining Particle Restitution Coefficients," On Polyphase Flow and Transport, ASME, Century 2-Engineering Technology Conferences.

[13] Ghenaiet, A., Tan, S. C., and Elder, R. L., 2004, "Experimental investigation of axial fan erosion and performance degradation," P I Mech Eng a-J Pow, 218(A6), pp. 437-450.

[14] Schmucker, J., Schaffler, A., 1994, "Performance Deterioration of Axial Compressors Due to Blade Defects," Propulsion and Energetic Panel, Symposium, Rotterdam, the Netherlands, April 25– 28.

[15] Dunn, M. G., Baran, A. J., and Miatech, J., 1996, "Operation of gas turbine engines in volcanic ash clouds," J Eng Gas Turb Power, 118(4), pp. 724-731.

[16] Walsh, W. S., Thole, K. A., Joe, C., 2006, "Effects of Sand Ingestion on the Blockage of Film-Cooling Holes," ASME Paper No. GT2006-90067, Proceedings of ASME Turbo Expo, Barcelona, Spain.

[17] Land, C. C., Joe, C., and Thole, K. A., 2010, "Considerations of a Double-Wall Cooling Design to Reduce Sand Blockage," J Turbomach, 132(3).

[18] El-Batsh, H., Haselbacher, H., 2002, "Numerical Investigation of the Effect of Ash Particle Deposition on the Flow Field through Turbine Cascades," IGTI, Amsterdam, Netherlands, GT-2002-30600.

[19] Ai, W. G., and Fletcher, T. H., 2012, "Computational Analysis of Conjugate Heat Transfer and Particulate Deposition on a High Pressure Turbine Vane," J Turbomach, 134(4).

[20] Sreedharan, S. S., and Tafti, D. K., 2011, "Composition dependent model for the prediction of syngas ash deposition in turbine gas hotpath," Int J Heat Fluid Fl, 32(1), pp. 201-211.

[21] Brun, K., Nored, M., and Kurz, R., 2012, "Particle Transport Analysis of Sand Ingestion in Gas Turbine Engines," J Eng Gas Turb Power, 134(1).

[22] Neilson, J. H., Gilchrist, A., 1968, "An Experimental Investigation into Aspects of Erosion in Rocket Motor Tail Nozzles," Wear, 11(2), pp. 123-143.

[23] F.K., R. J. H. a. S., 1979, "Causes of High Pressure Compressor Deterioration in Service," 15 Joint Propulsion Conference

[24] Zaita, A. V., Buley, G., and Karlsons, G., 1998, "Performance deterioration modeling in aircraft gas turbine engines," J Eng Gas Turb Power, 120(2), pp. 344-349.

[25] Scala, S. M., Konrad, M., and Mason, R.B., 2003, "Predicting the performance of a gas turbine undergoing compressor blade erosion," 39th AIAA/ASME/SAE/ASEE Joint Propulsion Conference and Exhibit, Huntsville, Alabama, July 20-23, 2003, AIAA 2003-5259.

[26] Hathaway, M. D., Chen, J., and Webster, R., 2003, "Time accurate unsteady simulation of the stall inception process in the compression system of a US Army helicopter gas turbine engine," DoD HPCMP User's Group Conference (UGC), Bellevuew, Washington, June 9-13.

[27] Tabakoff, W., and Hamed, A., 1984, "Installed engine performance in dust-laden atmosphere," AIAA/AHS/ASEE Aircraft Design Systems and Operations Meeting, San Diego, CA, October 31 – November 2, AIAA-84-2488.

[28] Tabakoff, W., Lakshminarasimha, A. N., and Pasin, M., 1989, "Simulation of compressor performance deterioration due to erosion," 34th International Gas Turbine and Aeroengine Congress and Exhibition, Toronto, Canada, June 4-8.

[29] Tabakoff, W., 1986, "Compressor erosion and performance deterioration," AIAA/ASME 4th Joint Fluid Mechanics, Plasma Dynamics and Laser Conference, Atlanta, GA, May 12-14.

[30] Balan, C., Tabakoff, W., 1983, "A method of predicting the performance deterioration of a compressor cascade due to sand erosion," AIAA 21st Aerospace Sciences Meeting, Reno, Nevada, January 10-13, AIAA-83-0178.

[31] Schneider, O., Dohmen, H. J., Benra, F.-K., Brillert, D.,, 2003, "Investigations of Dust Separation in the Internal Cooling Air System of Gas Turbines," ASME Paper No. GT2003-38293.

[32] Saffman, P. G., 1965, "The lift on a small sphere in a slow shear flow," J. Fluid Mech(22), pp. 385-400.

[33] Elghobashi, S., and Truesdell, G. C., 1992, "Direct Simulation of Particle Dispersion in a Decaying Isotropic Turbulence," J Fluid Mech, 242, pp. 655-700.

[34] Wang, Q., Squires, K. D., Chen, M., and McLaughlin, J. B., 1997, "On the role of the lift force in turbulence simulations of particle deposition," Int J Multiphas Flow, 23(4), pp. 749-763.

[35] Wang, Q., and Squires, K. D., 1996, "Large eddy simulation of particle deposition in a vertical turbulent channel flow," Int J Multiphas Flow, 22(4), pp. 667-683.

[36] Armenio, V., Piomelli, U., and Fiorotto, V., 1999, "Effect of the subgrid scales on particle motion," Phys Fluids, 11(10), pp. 3030-3042.

[37] Clift, R., Grace, J. R., and Weber, M. E., 1976, "Stability of Bubbles in Fluidized-Beds," Ind Eng Chem Fund, 15(1), pp. 87-87.

[38] C.T. Crowe, R. A. G. a. T. R. T., 1985, "Particle Dispersion by Coherent Structures in Free Shear Flows," Part. Sci. Technol. J, 3(3-4), p. 149.

[39] Shah, A., 2005, "Development and Application of Dispersed Two Phase Capability in a General Multi-Block Navier Stokes Solver," Thesis, Virginia Polytechnic Institute and State University, Blacksburg, VA.

[40] Patil, S., Tafti, D., 2013, "Large-Eddy Simulation With Zonal Near Wall Treatment of Flow and Heat Transfer in a Ribbed Duct for the Internal Cooling of Turbine Blades," Journal of Turbomachinery, 135(3), p. 031006.

[41] Tafti, D. K., 2005, "Evaluating the role of subgrid stress modeling in a ribbed duct for the internal cooling of turbine blades," Int J Heat Fluid Fl, 26(1), pp. 92-104.

[42] Sewall, E. A., and Tafti, D. K., 2008, "Large eddy simulation of flow and heat transfer in the developing flow region of a rotating gas turbine blade internal cooling duct with coriolis and buoyancy forces," J Turbomach, 130(1).

[43] Ooi, A., Iaccarino, G., Durbin, P. A., and Behnia, M., 2002, "Reynolds averaged simulation of flow and heat transfer in ribbed ducts," Int J Heat Fluid Fl, 23(6), pp. 750-757.

[44] Rau, G., Cakan, M., Moeller, D., and Arts, T., 1998, "The effect of periodic ribs on the local aerodynamic and heat transfer performance of a straight cooling channel," J Turbomach, 120(2), pp. 368-375.

[45] Sewall, E. A., Tafti, D. K.,Graham, A. B.,Thole, K. A., 2006, "Experimental validation of large eddy simulations of flow and heat transfer in a stationary ribbed duct," Int J Heat Fluid Fl, 27(2), pp. 243-258.

[46] Viswanathan, A. K., and Tafti, D. K., 2006, "A comparative study of DES and URANS for flow prediction in a two-pass internal cooling duct," Transactions of the ASME - Journal of Fluids Engineering-, 128(6), pp. 1336-1345.

[47] Shah, A., and Tafti, D. K., 2007, "Transport of particulates in an internal cooling ribbed duct," J Turbomach, 129(4), pp. 816-825.

Chapter 4

Predicting the Coefficient of Restitution for Particle Wall Collisions in Gas Turbine Components[3]

Jet engines often operate under dirty atmospheric conditions and are increasingly exposed to fine particulate matter such as sand, ash and dirt. Fine particulate ingestion, sand in particular, over prolonged periods can damage different engine components through deposition and erosion. The coefficient of restitution which is the ratio of rebound velocity to impact velocity encapsulates the energy losses occurring during a collision and is an indicator of erosion damage and deposition. In this work, a model for predicting the coefficient of restitution is developed as a function of material properties, particle impact velocity and angle, and particle diameter. The model combines elastic-plastic deformation losses and adhesion losses on impact with the surface. The modeled coefficient of restitution increases initially as a function of impact velocity in the regime in which adhesion forces dominate, and then starts decreasing as deformation losses increase. For all particle sizes the model coefficient of restitution appears to settle down in the range 0.25-0.4 at high velocities. The predictive capability of the model is demonstrated by comparing with various experimental and FEM data for a range of particle sizes and contact materials.

[3] A part of this chapter is reproduced from published work in ASME IGTI 2013 Conference, paper number, GT2013-95623, with permissions from ASME

4.1 Introduction

Increasing energy demands and mission challenges often require jet engines to operate in particle laden hostile environments. Large amounts of particle ingestion, sand in particular, can lead to severe damage to various engine components. Particle ingestion is excessive while takeoff and landing when engines are in ground proximity and running at full power[1]. Particles can also be ingested at cruising altitudes for an aircraft flying through volcanic dust clouds[2]. Operations in these hostile environments has led to serious aircraft accidents due to jet engine failure[3]. With the development of high bypass ratio turbofan engines, particle ingestion exposure has substantially increased[4]. The presence of particulates in the ingested air affects three major components of jet engine: compressor, combustor and turbine. Thermal barrier coatings (TBC) are also very susceptible to CMAS (Calcium-Magnesium Alumino Silicate) sand deposits. At elevated temperatures these deposits melt and degrade the TBC layer via a repeated freeze-thaw action and to a certain extent, direct chemical reaction with TBC constituents. These interactions can lead to TBC failure, accelerated oxidation and hot corrosion of underlying metallic bond coat and superalloys[5, 6]. According to studies by Edwards and Rouse[7], high sand ingestion can reduce engine stability by eroding blade profiles and lowering the compressor efficiency, as a result of which the line of operation is closer to the surge line. The operating line also rises as a result of decrease in turbine efficiency or a reduction in nozzle throat due to glazing.

To investigate the particle transport and its effect on different engine components, it is of prime importance to first understand the underlying physics of particle-wall interaction and quantify the energy losses in a particle-wall collision. Modeling the process of particle-surface impact is intricate, primarily because it is dynamic and nonlinear. A plethora of physical forces are involved during particle-wall collision, including elastic-plastic stress, electrostatic forces, thermophoresis, capillary forces and Van der Waals adhesion forces. For a dry collision, plastic deformation and adhesion losses are major contributors to energy losses; contribution of either mechanism depends on impact parameters: particles size, impact velocity and material properties of surfaces in contact. For spherical particles of typical engineering materials, and diameters well above 100 μm, the collisions are almost perfectly elastic. As the impact velocity increases, the coefficient of restitution decreases usually monotonically and often significantly. Even for particle diameter in the range 1-100 μm, the coefficient of restitution follows the same trend at relatively high impact velocities[8]. But for much smaller impact velocities (less than 10 m/s), the coefficient of restitution drops considerably with the decrease in velocity[9]. For larger particles at lower impact velocities, deformation losses and adhesion losses are insignificant. As the impact velocity increases the deformation and hence plastic losses increase. For much smaller particles, the adhesion losses are significant while deformation is minimal. As velocity decreases, adhesion becomes the dominant mechanism and the rebound velocity decreases. Several past studies have focused on modeling and predicting the deformation, adhesion and stress wave propagation losses during an impact, depending upon the particle size or velocity range investigated.

A basic elastic contact model , or " asperity based model" for the contact of two rough surfaces was introduced by Greenwood and Willamson (GW)[10]. A collection of scattered spherical asperities were used to represent roughness of the contacting surfaces. To calculate the asperity deformation, the GW model assumed the asperities deformed according the Hertz elastic contact theory. This basic elastic model was further extended to include the factors such as curved surfaces[11], curvature of asperities[12], elliptic paraboloidal asperities[13] and anisotropic surfaces[14]. Chang, Etsion, and Bogy (CEB)[15, 16] proposed an elastic-plastic model as an improvement to GW model by including the plastic deformation beyond the elastic limit of contacting spheres. CEB model enables the calculation of the plastic contact area for interferences larger than the critical deformation. The GW model and contemporary models for purely the plastic contact were ascertained to be special cases of the CEB model.

Several previous studies have investigated impact of spheres on a flat surface. Categorically, contact models have been based on principles of energetics, mechanics and correlations guided by experiments. Tabor[17] divided the process of impact into three stages of elastic deformation, plastic deformation and rebound, and considered energy losses during each stage to calculate the coefficient of restitution. By applying the original load several times, it was also shown that the unloading stage of the impact is reversible and essentially elastic[18]. While Tabor's approach was that of macroscopic surface physics, Johnson[19] investigated elastostatics, elastic impact of spheres, oblique impact of spheres, wave propagation during an impact, and plastic impact at moderate speeds, among other factors, before leading to a coefficient of restitution. In conjunction with elaso-plastic CEB model[16], Chang and Ling[15] introduced a model for coefficient of restitution for the impact of spheres when the deformation is beyond the elastic limit. This model showed better coefficient of restitution predictions when compared to results from Tabor's and Johnson's models.

Thornton[20] investigated the collision by dividing the impact into a perfectly elastic phase and perfectly plastic phase, and provided an analytical relation for coefficient of restitution as a function of normal impact velocity. Li et al.[21] modified the Johnson's model[19] to include more detailed load variation and presented a theoretical model for coefficient of restitution for the normal impact of a rigid sphere with an elastic-perfectly plastic half space or an elastic-perfectly plastic sphere with a rigid wall. The proposed contact force-displacement relations and restitution coefficients predictions showed good agreement with finite element analysis. Wu et al. [22] investigated the impact of an elastic sphere with elastic and elastic-plastic surface for only finite plastic deformation using finite element method (FEM). This study observed two major energy dissipation mechanisms – stress wave propagation and plastic deformation. It was also shown that for impacts involving plastic deformation, plastic deformation is dominant energy dissipation mechanics, as the energy loss due to stress wave propagation is relatively small. Another important observation was sharper decrease of coefficient of restitution with an increasing normal impact velocity for finite plastic deformation impacts. Weir and Tallon[23] also proposed an equation to predict the coefficient of restitution for normal particle impacts at lower velocity. This study predicted that the coefficient of restitution for equally sized sphere-sphere impact to be 19% smaller than for sphere-plate impacts. The developed theory also predicted increase in restitution coefficient following identical impacts at the same point, which was also confirmed experimentally. Vu-Quoc and Zhang[24] presented an elasto-plastic normal force displacement model for spheres in collision. This model extends the Hertzian contact theory to account for plastic deformation, but the model parameters have to be obtained from finite element analysis or experiments.

Brach and Dunn[25] presented a mathematical model for adhesion losses in a particle-wall collision for microspheres. Microspheres of diameter range 1-10 μm are studied where energy loss is primarily adhesion dominated. While the particle is in contact with the surface it forms an adhesion bond with the surface which fractures during rebound. Bowling[26], discusses the variety of forces such as the Van der Waals force that contribute to adhesion. The adhesion force often is quantified through the use of an adhesion energy which is distributed over the contact surface of the two bodies in contact. It is assumed that all the adhesion energy, W_A, required to separate the particle from a surface is lost in separation process. Some researchers associate the Van der Waals force exclusively with the process of separation. Among others, this view has been proposed by Billings and Wilder[27], Clift[28] and Hinds[29].

The impact of particles on flat surfaces has been also examined through several experimental studies. Hunter[30] showed that for a steel ball impinging on a large block of steel or glass, less than 1 per cent of the kinetic energy of the ball is lost to elastic wave propagation. Tillett[31] investigated the impact of steel ball on plates of glass and plastics, and reported that energy losses to stress wave propagation were of the order of 3 per cent for steel ball impacting on glass. Goldsmith and Lyman[32] calculated the coefficient of restitution from impact and rebound velocities measured with a stroboscopic camera, and reported results for the collision of a hard steel sphere against a plane target of various metals. Bridges et al.[33] conducted experiments with ice particles and reported coefficient of restitution is proportional to the impact velocity to a power of -0.23. Measurements of the coefficient of restitution were also reported by Kharaz and Gorham[34] for the impact of 5 mm aluminium oxide spheres on thick plates of a steel and alluminium alloy for wide range of impact velocity. Dahneke[35] and Loeffler[36] measured and classified the probability of capture. They also proposed an expression for critical or capture velocity, below which rebound does not occur. Rogers and Reed[37] combined the elastic theories and adhesion theories for impact of elastic-plastic materials, and conducted experiments to validate the proposed models. A method for determining the adhesive surface energy from the measurements of impacts leading to elastic deformations was also presented. Transverse elastic deformation of spheres was investigated by Mindlin and Deresiewics[38] and has been observed in discs during impact by Maw et al.[39]. Wall[8] reported experiments on impact of ammonium fluorescein microspheres on various target materials, using laser Doppler velocimetry. Plastic deformation was found to be dominating energy loss mechanism for the velocity range considered. Additional experiments conducted with and without continuous discharge of the impact surface indicated insignificant electrostatic contribution to particle adhesion. More recently particle-wall collisions have also been investigated by M. Sommerfeld[40, 41] and O. Simonin[42].

4.2 Objective

The objective of the current study is to develop a model to predict the coefficient of restitution for particle wall collisions with a focus on sand transport in gas turbine engines. The current work presents a model that builds on separate theories of deformation and adhesion losses to develop an integrated model applicable over a wide range of particle sizes from a few microns to a few hundred microns which is critical for application to gas turbines. The study presents a novel model that identifies deformation and adhesion as the dominant energy loss mechanisms for a dry particle-wall collision and analytically calculates these losses to determine the total energy loss during an impact. For sand transport in gas turbine engines, either of these two or both the mechanisms can be important during collisions due to the wide range of particle sizes and flow conditions experienced by the particles.

4.3 Methodology

The current model builds on existing models on elastic, elastic-plastic deformations[43] and adhesion theories of particle–wall interaction[25]. First these existing theories are discussed briefly, followed by their application in predicting the collision losses in a particle-wall interaction.

4.3.1 Impact Models

4.3.1.1 Elastic contact model

Geometrical effects on local elastic deformation properties have been considered as early as 1880 with the *Hertzian Theory of Elastic Deformatio*[44]. Hertz theory relates the circular contact area and stresses of two spheres (or a sphere with a plane) in a purely elastic contact. In this theory plastic deformation and any other surface interactions such as near contact Van der Waals or contact adhesive interactions are neglected. Since no energy losses are considered, Hertz contact theory is only applicable to a perfectly elastic collision leading to coefficient of restitution equal to unity. The contacting bodies are assumed to be isotropic and homogeneous, and area of contact is assumed very small compared to radii of curvature. Hertz theory can be used to study the elastic impact of a sphere with a rigid wall. Hertzian theory readily provides a relationship between applied load, P, and contact radius, a, of the sphere with the wall. The distance by which the sphere is displaced normally into the rigid wall can be described as interference, ω, as shown in figure 4.1.

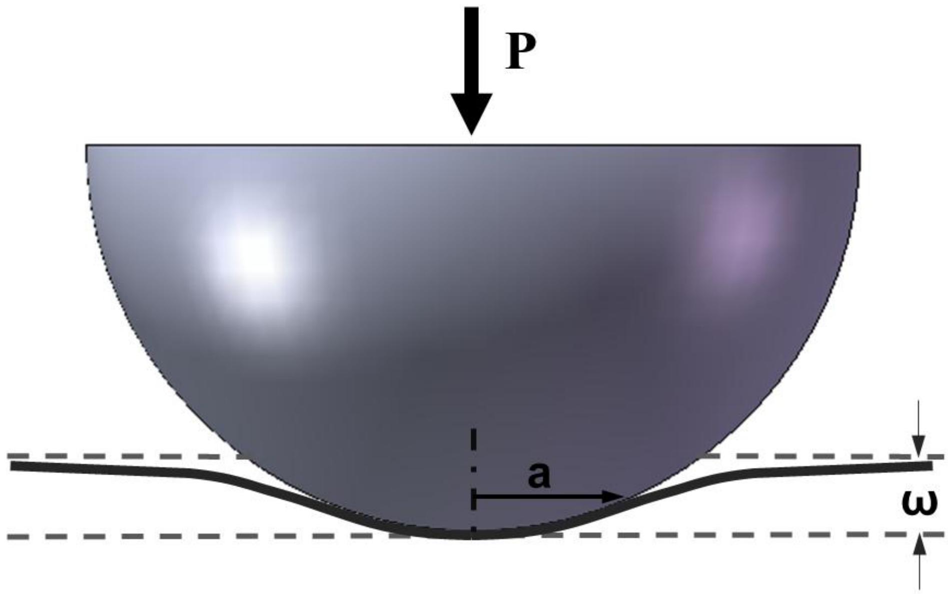

Figure 4.1 Hertz Elastic Contact

4.3.1.2 Elastic-plastic contact model

The sphere-wall collision can be considered elastic only for relatively small loads or interferences. With increasing load the stresses within the contact increase, eventually causing the material within the sphere to yield. The deformation in the sphere is no longer elastic, and the interference at this point of yielding is known as the critical interference, ω_c. This yield point and critical interference have been investigated in previous works. Jackson and Green[45] (JG) proposed critical interference as a function of yield strength. The resulting equation is.

$$\omega_c = \left(\frac{\pi C S_y}{2E'}\right)^2 R \qquad (1)$$

where $C = 1.295\exp(0.736\eta)$

And equivalent elastic modulus $E^{'}$ is calculated as

$$\frac{1}{E^{'}} = \frac{1-\nu_1^2}{E_1} + \frac{1-\nu_2^2}{E_2}$$

where E_1, E_2, ν_1 and ν_2 are the elastic moduli and Poisson's ratios of the materials in contact.

The equation uses Poisson's ratio and yield strength of the material that yields first. CS_y is calculated for both the materials in contact and the smaller of the two values is chosen, i.e., $CS_y = \min\left(C(\eta_1)S_{y1}, C(\eta_2)S_{y2}\right)$.

The critical interference, ω_c, can be used to calculate critical load or force, P_c, from Hertz theory. The resulting critical contact load at the point of initial yielding can be written as

$$P_c = \frac{4}{3}\left(\frac{R}{E'}\right)^2 \left(\frac{\pi}{2} CS_y\right)^3 \qquad (2)$$

Hertz theory also gives the contact area at the critical interference, critical contact area

$$A_c = \pi^3 \left(\frac{CS_y R}{2E'}\right)^2 \qquad (3)$$

The JG model predicts the contact load and contact area between an elastic plastic hemisphere and a flat surface. At $0 < \omega/\omega_c < 1.9$, the JG model effectively coincides with the Hertzian solution, even though onset of plastic deformation occurs at $\omega = \omega_c$. For modeling the elasto-plastic impact, the following JG relations are used:

$$A_{ep} = \pi R\omega\left(\frac{\omega}{1.9\omega_c}\right)^B \tag{4}$$

$$P_{ep} = P_c\left\{\left[\exp\left(-\frac{1}{4}\left(\frac{\omega}{\omega_c}\right)^{\frac{5}{12}}\right)\right]\left(\frac{\omega}{\omega_c}\right)^{\frac{3}{2}} + \frac{4H_G}{CS_y}\left[1-\exp\left(-\frac{1}{25}\left(\frac{\omega}{\omega_c}\right)^{\frac{5}{9}}\right)\right]\frac{\omega}{\omega_c}\right\} \tag{5}$$

Where

$$B = 0.14\exp\left(23.\varepsilon_y\right) \tag{6}$$

$$\varepsilon_y = \frac{S_y}{E'} \tag{7}$$

$$\frac{H_G}{S_y} = 2.84 - 0.92\left(1-\cos\left(\pi\frac{a}{R}\right)\right) \tag{8}$$

$$\frac{a}{R} = \frac{\pi C e_y}{2}\left\{\frac{\omega}{\omega_c}\left(\frac{\omega}{1.9\omega_c}\right)^B\right\}^{1/2} \tag{9}$$

These results were validated by Quicksall et al.[46] for a wide range of materials by varying E, S_y and η. The predicted loads also compare well with some experimental results available.

Critical values defined in Equation (1-3) can be used to normalize the results for general application. The same normalization scheme has been employed in many previous works. The normalized parameters are:

$$\omega^* = \omega / \omega_c \tag{10}$$

$$P_e^* = P_e / P_c = (\omega^*)^{3/2} \tag{11}$$

$$A_e^* = A_e / A_c = \omega^* \tag{12}$$

The elasto-plastic relations can be normalized in the same way.

4.3.1.3 Adhesion model

The adhesion model proposed by Brach and Dunn[25] for impact of microspheres is adopted in the current study to calculate the adhesion losses during a particle-wall collision. The model assumes spherical particles and adhesion losses to be significant only during the rebound phase of the impact corresponding to the breakup of adhesion bond. It must be noted that the impact velocities at this stage are the velocities after accounting for the deformation losses. The energy loss of deformation is included by employing the coefficient of restitution, e_{ep}, for the deformation losses, calculated by using the elastic and elasto-plastic model for deformation analysis. Also, the elasto-plastic deformation losses are analyzed only in terms of normal impact velocity. It is assumed that only the normal impact velocity and normal loads govern the deformation and hence the plastic losses.

4.3.2 Coefficient of Restitution

The coefficient of restitution quantifies the energy losses during an inelastic particle-wall collision. For a collision of a particle against a fixed rigid wall, the coefficient of restitution, e, is defined as the ratio of the magnitudes of the rebound velocity to the impact velocity. Similarly normal and tangential coefficients of restitution are defined in terms of corresponding velocity components.

$$e = \frac{V_2}{V_1}, \quad e_n = \frac{V_{2n}}{V_{1n}}, \quad e_t = \frac{V_{2t}}{V_{1t}} \qquad (13)$$

Where V_1 is the magnitude of the impact velocity and V_2 is magnitude of the rebound velocity. The coefficient of restitution is, however, not a fundamental material or particle property. Instead, the particle-wall interaction forces and hence, losses involved in collision dynamics determine the coefficient of restitution. The coefficient of restitution varies from 0 for a perfectly plastic collision to a value of unity for a perfectly elastic collision.

For relatively small impact loads, no energy is lost to plastic deformation and contact area is too small to cause any adhesion losses, and the collision remains elastic. As the load increases, one or both the surfaces in contact can yield leading to elasto-plastic dynamics. The current work investigates elastic, elasto-plastic and adhesive interaction during a spherical particle-wall collision. The motion of the center of the sphere during a collision can then be described by following four collision stages: Elastic stage, until the loads are not high enough to cause any plastic deformation. Elasto-plastic stage, the loads and resulting stresses are large enough to cause plastic deformation. This stage continues until the maximum load and hence maximum interference is reached. Restitution stage, this is the rebound stage when the sphere begins to unload to the point when surfaces are no longer in contact. Adhesion stage, while the sphere is leaving the surface, energy is lost due to adhesive interaction. Though this stage is concurrent with the restitution stage, the losses in this stage are studied exclusively, assuming deformation losses and adhesion losses are independent. Also, it is assumed that deformation is governed by the normal velocity only and the tangential velocity remains unchanged during the first three stages. The change in tangential velocity takes place through the frictional loss at the contact, which is calculated in the adhesion stage. These stages will be discussed in more detail in the following sections.

4.3.3 Stage I. Elastic compression stage

The first stage starts with the contact instant ($P=0$) and ends when the contact force reaches the known value of the critical load ($P=P_c$). At the critical load the interference is critical interference ($\omega=\omega_c$). Since the sphere deforms elastically during this stage, Hertz theory can be employed to calculate load and kinetic energy of the sphere as follows:

$$\frac{1}{2}mv_n^2-\frac{1}{2}mV_{1n}^2=-\int_0^{\omega}P_e d\omega \tag{14}$$

where ω represents instantaneous interference when the instantaneous normal velocity is v_n . P_e is the instantaneous Hertzian load. The right hand side of the equation represents the part of the kinetic energy of the sphere that is stored as strain energy in the sphere. Substituting the contact force from Hertz model results in

$$\frac{1}{2}mv_n^2-\frac{1}{2}mV_{1n}^2=-\frac{4}{3}E'\sqrt{R}\int_0^{\omega}\omega^{3/2}d\omega \tag{15}$$

And then integrating

$$\frac{1}{2}mv_n^2-\frac{1}{2}mV_{1n}^2=-\frac{8}{15}E'\sqrt{R}\omega^{5/2} \tag{16}$$

Rearranging the term to get instantaneous normal velocity

$$v_n = \sqrt{V_{1n}^2 - \frac{16}{15}\frac{E'}{m}\sqrt{R}\omega^{5/2}} \tag{17}$$

This stage ends at the onset of plastic deformation, at $\omega = \omega_c$. Substituting $\omega = \omega_c$ into Equation (17) provides a relation for the critical velocity at which the sphere begins to yield plastically.

$$v_{nc} = \sqrt{V_{1n}^2 - \frac{16}{15}\frac{E'}{m}\sqrt{R}\omega_c^{5/2}} \tag{18}$$

This critical velocity, v_{nc}, is the instantaneous normal velocity of the sphere when it starts to deform plastically. Hence, by requiring $v_{nc} = 0$, the above relation also gives the maximum normal impact velocity, V_{1nc}, for which the collision is perfectly elastic.

$$V_{1nc} = \sqrt{\frac{16}{15}\frac{E'}{m}\sqrt{R}\omega^{5/2}} = \sqrt{\frac{4\omega_c P_c}{5m}} \tag{19}$$

4.3.4 Stage II. Elasto-plastic compression stage

After the first stage the contact load is greater than the critical load, P_c, and plastic deformation begins to appear. For this stage, the current model employs the elasto-plastic contact analysis purposed by Jackson and Green[46].

Using the JG model the equations are solved numerically. During elasto-plastic deformation the strain energy accumulated in the sphere, W_{ep}, can be described in terms of active load, P_{ep}. The instantaneous velocity during this stage can be written as

$$\frac{1}{2}mv_n^2 = \frac{1}{2}mV_{1n}^2 - \frac{8}{15}E'\sqrt{R}\omega_c^{5/2} - \int_{\omega_c}^{\omega} P_{ep}d\omega \tag{20}$$

P_{ep} is not a Hertzian load anymore but an elasto-plastic contact load from JG spherical contact model (Equation (5)).

The sphere will deform until the center of the sphere comes to an instantaneous stop. The maximum interference, ω_m, can be found as a function of V_{1n}, by setting $v_n = 0$ in the above equation.

$$\frac{1}{2}mV_{1n}^2 = \frac{8}{15}E'\sqrt{R}\omega_c^{5/2} + \int_{\omega_c}^{\omega_m} P_{ep}d\omega \tag{21}$$

The above equation can be solved to provide ω_m, as a function of V_{1n}. As expected, ω_m increases with V_{1n}.

4.3.5 Stage III. Restitution stage

After the sphere comes to a full stop and maximum interference has been achieved, the sphere begins to rebound and recover its kinetic energy. The sphere will not fully recover its original shape, but inherit a permanent residual interference, ω_{res}, and the radius of curvature will change to R_{res}. It is assumed that this recovery from ω_m to ω_{res} is completely elastic and Hertz solution can be used to model the contact load as the sphere rebounds. The contact load decreases from the maximum value, P_m, to zero. The elastic force of restitution will start from the maximum elasto-plastic force at $\omega = \omega_m$ such that:

$$\left(P_{ep}\right)_m = \frac{4}{3}E'\sqrt{R_{res}}\left(\omega_m - \omega_{res}\right)^{3/2} \tag{22}$$

R_{res} and ω_{res}, can be calculated in two different ways. First, from Etsion et al.[47].

$$\frac{\omega_{res}}{\omega_m} = 1 - \frac{3\left(P_{ep}\right)_m}{4E' a_m \omega_m} \tag{23}$$

$$R_{res} = \frac{4E'\left(a_m\right)^3}{3\left(P_{ep}\right)_m} \tag{24}$$

a_m is the contact radius at the maximum interference, ω_m. The second method is by fitting an equation to the finite element results of Jackson, Chusoipin , and Green[48]. R_{res} can be obtained as :

$$\frac{\omega_{res}}{\omega_m} = 1.02\left(1 - \left(\frac{\left(\omega^*\right)_m + 5.9}{6.9}\right)^{-0.54}\right) \tag{25}$$

$$R_{res} = \frac{1}{\left(\omega_m - \omega_{res}\right)^3}\left(\frac{3}{4}\frac{\left(P_{ep}\right)_m}{E'}\right)^2 \tag{26}$$

The normal velocity recovered, $V_{2n'}$, as the sphere leaves the surface can be solved from

$$\frac{1}{2}mV_{2n'}^2 = \int_{\omega_m - \omega_{res}}^{0}\left(\frac{4}{3}E'\sqrt{R_{res}}\,\omega^{3/2}\right)d\omega \tag{27}$$

Giving

$$V_{2n'} = \sqrt{\frac{16E'}{15m}} \left(R_{res}\right)^{1/4} \left(\omega_m - \omega_{res}\right)^{5/4} \tag{28}$$

The coefficient of restitution up to this stage, e_{ep}, can be calculated as

$$e_{ep} = \frac{V_{2n'}}{V_{1n}} \tag{29}$$

4.3.6 Stage IV. Adhesion breakup stage

While the sphere is rebounding under the influence of elastic contact load in the restitution stage, it also experiences additional adhesive contact force from the surface which tries to keep it on the surface. The sphere has to break this adhesion bond to rebound. In the current work, this adhesion breakup is considered independent of other stages, though it coincides with the restitution stage. Under this assumption, the process of adhesion energy loss and deformation energy loss are independent.

Following Brach and Dunn[25], from momentum and energy conservation analysis of an oblique impact of a particle with a rigid wall, rebound velocities can be written in terms of impact velocities and elaso-plastic coefficient of restitution, e_{ep}, as follows:

$$V_{2n} = e_{ep} V_{1n} \left(1 + 2W_A / e_{ep}^2 m V_{1n}^2\right)^{1/2} \tag{30}$$

$$V_{2t} = V_{1t} - \mu V_{1n} \left\{1 + e_{ep} \left(1 + 2W_A / e_{ep}^2 m V_{1n}^2\right)^{1/2}\right\} \tag{31}$$

W_A is the work of adhesion. For the special case of normal impact this yields

$$W_A = \frac{1}{2} m V_{1n}^2 \left[\left(\frac{V_{2n}^2}{V_{1n}^2} \right) - e_{ep}^2 \right] \tag{32}$$

Work of adhesion is calculated from JKR adhesion theory which uses the contact area during impact and the surface energy to calculate work required to break the adhesion bond. As discussed by Brach and Dunn[25], the adhesion bond is fractured during the rebound phase through a force distributed over the periphery of the receding circular contact area. This force can be represented as an idealized line force, $F_A = 2\pi a f_0$, f_0 is circumferential tension of the adhesion fracture force. The work of adhesion, W_A, can be expressed by:

$$W_A = -\left[\frac{5}{4} \rho \pi^{9/2} \left(k_1 + k_2 \right) \right]^{2/5} \gamma R^2 V_{1n}^{4/5} \tag{33}$$

Where $k_i = (1-\eta_i^2)/\pi E_i$, and γ is the surface adhesion parameter which depends upon the two surfaces in contact.

Hence, the final coefficient of restitution can be written as

$$e_n = \frac{V_{2n}}{V_{1n}} = e_{ep} \left(1 + 2W_A \big/ e_{ep}^2 m V_{1n}^2 \right)^{1/2} \tag{34}$$

$$e_t = \frac{V_{2t}}{V_{1t}} = 1 - \mu \tan\alpha \left(1 + e_{ep} \right) \left(1 + 2W_A \big/ e_{ep}^2 m V_{1n}^2 \right)^{1/2} \tag{35}$$

Where α is the impact angle with the surface.

For the case of a normal impact

$$e = \frac{V_2}{V_1} = e_{ep}\left(1 + 2W_A / e_{ep}^2 m V_1^2\right)^{1/2} \tag{36}$$

For a given particle-wall pair, the Equation (21) is integrated numerically to get ω_m. The results of integration and Equation (23) or Equation (25) are substituted in Equation (30) to obtain V_{2n}.

4.4 Results

The calculated coefficient of restitution from the current model is first compared with experimental results in two extreme regimes where only deformation or only adhesion losses are dominant. All the results discussed show the variation of normal coefficient of restitution with normal impact velocity. The normal coefficient of restitution is referred to as just e from this point on.

For deformation dominated regime, the model is compared with experimental results provided by Kharaz and Gorham[49]. To compare these experimental results with the current model, the material properties used are from reference[43]. In the deformation dominated regime adhesion is insignificant, and the model is essentially JG model. The results are compared for 0.005 m diameter aluminum oxide spheres impacting an aluminum surface. Figure 4.2. shows that the model results compare very well with experimental results. Figure 4.3. shows the model predictions compared with Kharaz and Gorham[34] experiments for aluminum oxide spheres impacting a steel surface. The coefficient of restitution predictions are in good agreement with the experiments in the lower velocity range only. The disagreement at higher velocities can be attributed to the fact that steel has a considerably higher strain hardening ratio (ultimate strength/yield strength) compared to aluminum. The strain hardening effect was also reported by Kharaz and Gorham[34]. As shown by recent studies[50, 51], this strain hardening effect for spherical contact is more pronounced at higher velocities compared to lower velocities.

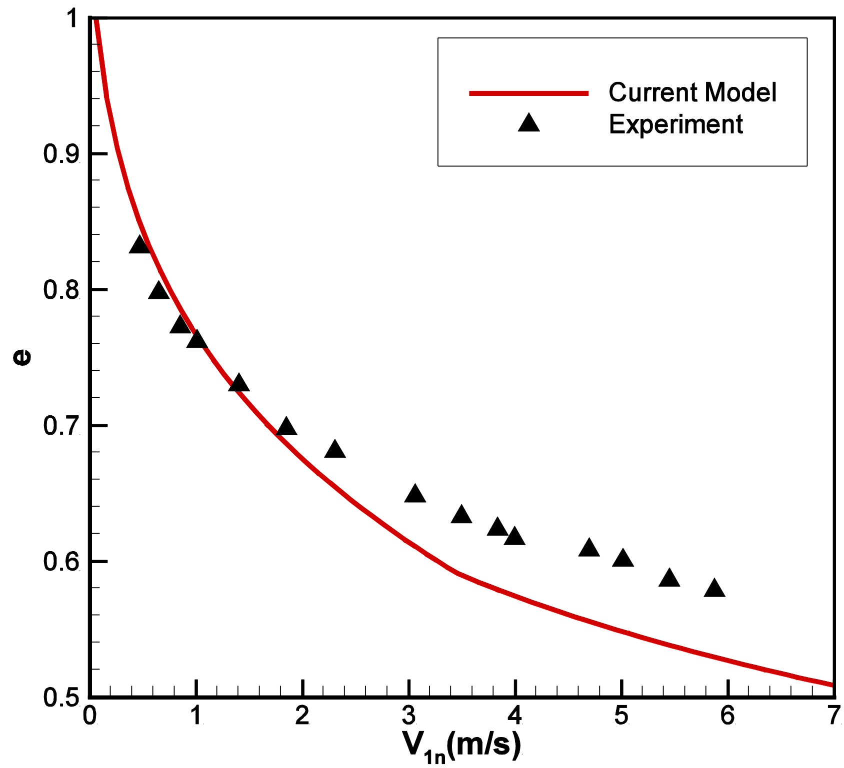

Figure 4.2 Model comparison with experimental results from Kharaz and Gorham[34] for aluminum oxide spheres impacting an aluminum surface

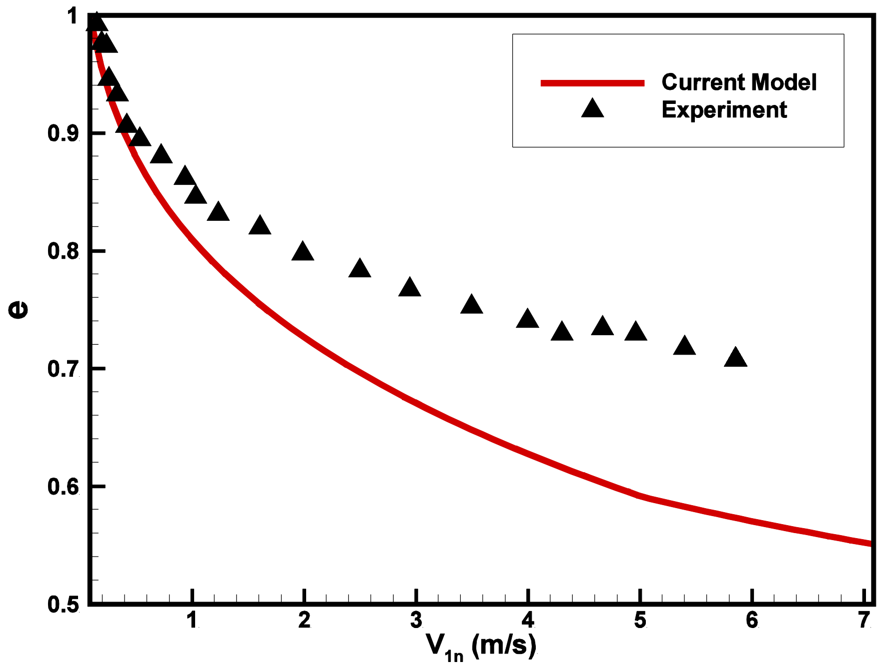

Figure 4.3 Model comparison with experimental results from Kharaz and Gohram[34] for aluminum oxide spheres impacting a steel surface

For the adhesion dominated regime, the model is compared with experimental data of Wall et al.[8] and the adhesion model of Brach and Dunn[25]. The results are compared for 4.9 μm diameter Ammonium fluorescein (NH_4Fl) spheres impacting a Molybdenum surface. In Figure 4.4, the current model compares well with experimental data and the Brach and Dunn adhesion model. It can be observed that Brach and Dunn predicted a higher overall coefficient of restitution at higher velocities by using a constant e_{ep} value of 0.909 in their application of the model. In the current model, the restitution coefficient , e_{ep}, is calculated from deformation losses and decreases as the velocity increases. At lower velocities both the models are identical because deformation losses are insignificant. As the velocities increase the deformation losses start increasing and e_{ep} decreases. Subsequently, this model is expected to predict the energy losses better at higher velocities, compared to Brach and Dunn model as deformation becomes significant.

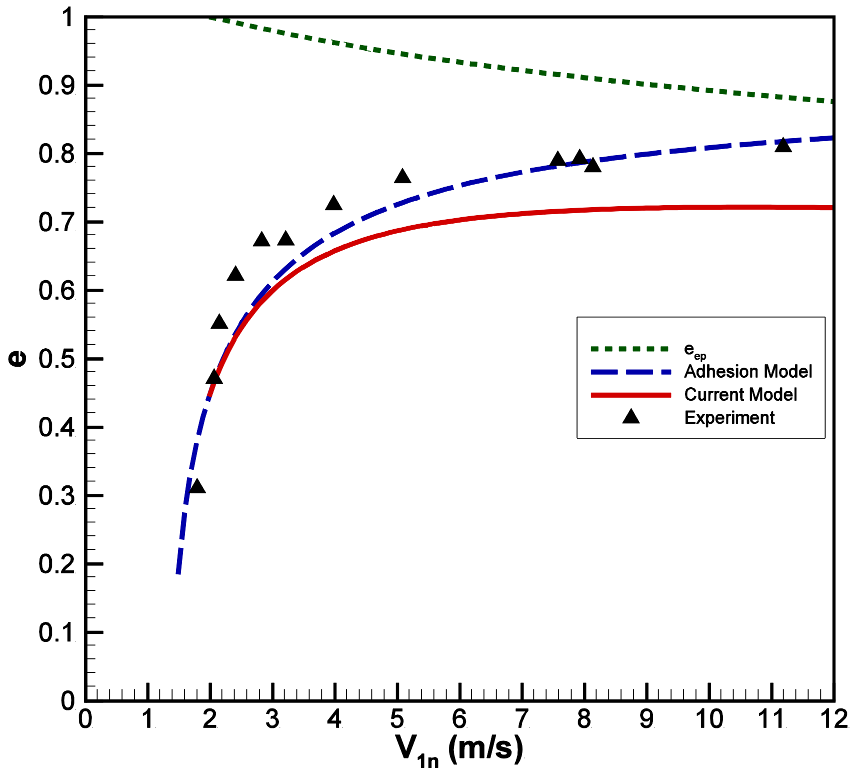

Figure 4.4 Model comparison with experiments for NH_4Fl spheres impacting a molybdenum surface

The real test for the current model is in the regime where both deformation and adhesion mechanisms are significant as would be encountered in gas turbine components. Typically, ingested sand particles sizes can vary from 1 micron to 200 µm depending on the source of sand particles and the location in the engine flow path. In this range, both deformation and adhesion losses are important. First, the model predictions for sand particles of size 1 micron to 100 µm impacting a steel surface are presented in Fig. 4.5.

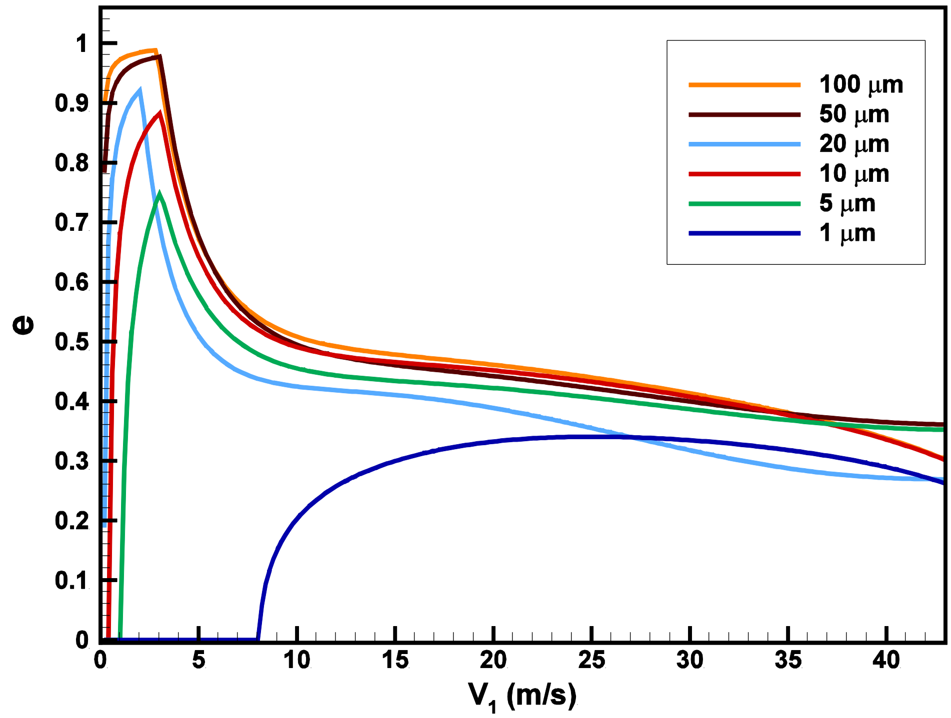

Figure 4.5 Model predictions for sand particles impacting steel surface for different particle sizes

The predictions show that for 1 micron particles, the coefficient of restitution remains zero for very low velocities (< 8 m/s). This is due to adhesion being dominant in this velocity range, and the particle does not have enough kinetic energy to break the adhesion bond and rebound. A general trend in the coefficient of restitution is observed in the size range considered. For lower velocities the coefficient of restitution increases with velocity to a point after which the deformations losses become significant and the restitution coefficient starts to decrease and eventually settles to a value between 0.25 to 0.4 at higher velocities. The predictions also show that the velocity range for which adhesion is dominant decreases with an increase in the particle size. This trend was also observed in previous studies and can be attributed to the fact that deformation becomes significant at lower velocities as the particle size increases.

Figure 4.6. compares the coefficient of restitution for sand particles impacting Al 2024 surface with experimental data from Tabakoff[52]. The current model uses the particle diameter of 150 μm and 200 μm for the coefficient of restitution calculations. The restitution characteristics from experiments are presented showing mean values with ± 1 standard deviation. Considering all the assumptions in the current model and the large spread in the experimental data, the restitution predictions from the model are in very good agreement with the experiments. It can be observed that predictions are better at higher velocities than at lower velocities. This is because a single particle diameter of 150 μm is used in the model. In the experiments more than 65% of the particles are in the size range 150-200 μm. At lower impact velocities the coefficient of restitution increases with particle size and at higher impact velocities the coefficient of restitution is less sensitive to particle size. This observation can be verified from the coefficient of restitution variation with size presented later (Figure 7.). Hence, using a larger particle diameter in the current model will predict even closer agreement with the experiments at lower velocities while remaining unchanged at higher velocities.

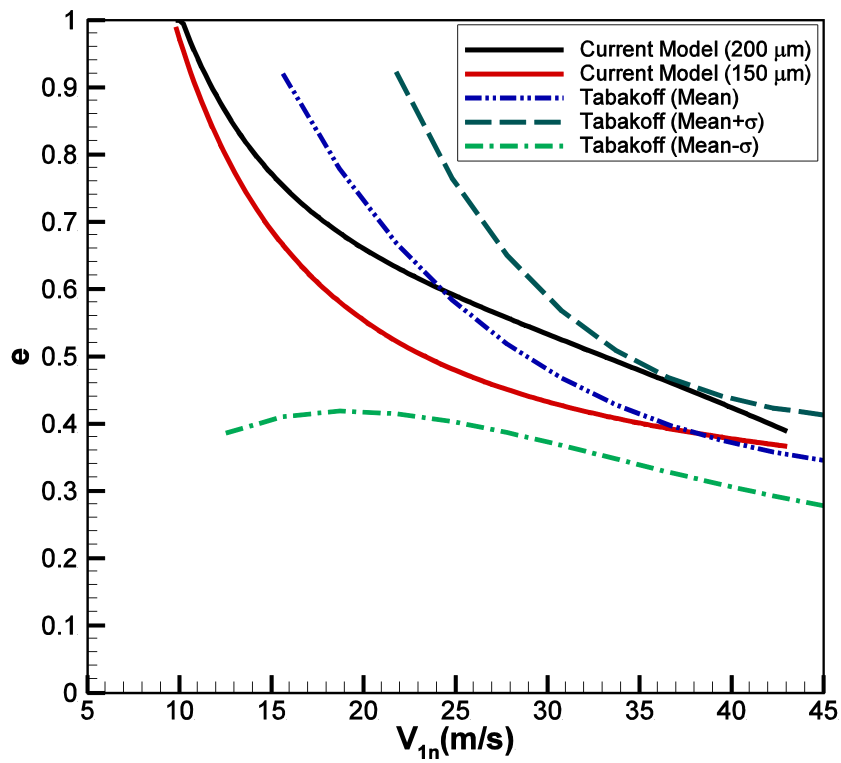

Figure 4.6 Model comparison with experiments for sand impacting Al 2024 surface

Finally, the current model is compared with the experiments conducted at Virginia Tech for sand particles impacting a steel surface. Arizona road test dust, with nominal particle size range 20-40 μm is used in the experiments. The details of the experimental setup and results are presented in [53]. Figure 4.7. shows current model predictions for 10 μm, 20 μm and 50 μm size; and mean results from the experiments. Considering the challenges in measurements of coefficient of restitution in the experiments, the predictions are in reasonable agreement.

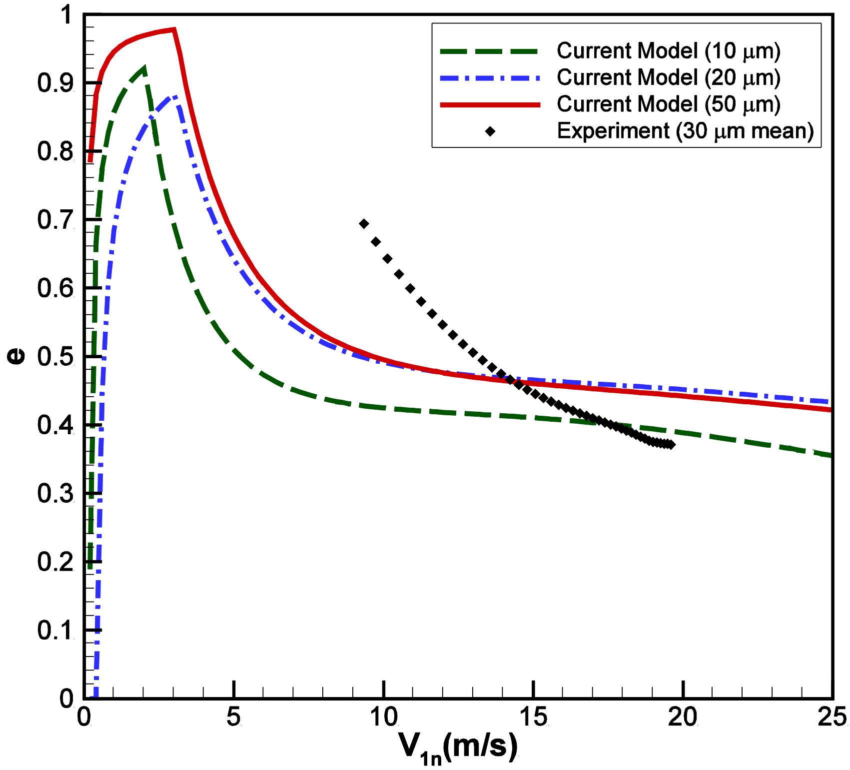

Figure 4.7 Model comparison with experiments for sand impacting steel surface

4.5 Conclusions

A model for particle-wall collision based on deformation and adhesion losses is presented. The model builds upon the available theories of deformation and adhesion for a spherical contact with a flat surface. The model calculates deformation losses and adhesion losses from particle-wall material properties and impact parameters. The model is broadly applicable to spherical particles undergoing oblique impact with a rigid wall and successfully predicts the general trends observed in experiments. The model coefficient of restitution increases initially as a function of impact velocity and then starts to decrease. At low impact velocities, adhesion losses are significant, whereas at high velocities, deformation losses dominate. As particle diameter increases, the restitution coefficient starts decreasing at lower impact velocities because of larger deformation losses at the same impact velocity. For all particle sizes the coefficient of restitution appears to settle down in the range 0.25-0.4 at high velocities. The model's utility and accuracy is demonstrated by comparing with various experimental and FEM data for a range of particle sizes and contact materials. The proposed model can be conveniently implemented with any computational fluid dynamics (CFD) code to predict sand particle transport in gas turbine components and can be sensitized to temperature by using temperature dependent material properties which is important in the study of turbine hot gas path flows.

4.6 Acknowledgements

The current work would not be possible without the support and direction of Rolls-Royce, Indianapolis, IN. The authors would also like to thank Dr. Wing Ng, Dr. Srinath Ekkad, Colin Reagle and Jacob Delimont from Virginia Tech for their thoughtful discussion, analysis and advice.

References

[1] Hamed, A., Tabakoff, W., and Wenglarz, R., 2006, "Erosion and deposition in turbomachinery," J Propul Power, 22(2), pp. 350-360.

[2] Kim, J., Dunn, M. G., Baran, A. J., Wade, D. P., and Tremba, E. L., 1993, "Deposition of Volcanic Materials in the Hot Sections of 2 Gas-Turbine Engines," J Eng Gas Turb Power, 115(3), pp. 641-651.

[3] Tabakoff, W., 1987, "Compressor Erosion and Performance Deterioration," J Fluid Eng-T Asme, 109(3), pp. 297-306.

[4] Alge T. L., M. J. T., 1994, "Modern Transport Engine Experience with Environmental Ingestion Effect," Propulsion and Energetic Panel (PEP), Symposium, Rotterdam, Netherlands. AGARD.

[5] Borom, M. P., Johnson, C. A., and Peluso, L. A., 1996, "Role of environmental deposits and operating surface temperature in spallation of air plasma sprayed thermal barrier coatings," Surf Coat Tech, 86(1-3), pp. 116-126.

[6] Kramer, S., Yang, J., Levi, C. G., and Johnson, C. A., 2006, "Thermochemical interaction of thermal barrier coatings with molten CaO-MgO-Al2O3-SiO2 (CMAS) deposits," J Am Ceram Soc, 89(10), pp. 3167-3175.

[7] Edwards, V. R., Rouse, P.L., 1994, "U.S. Army Rotorcraft Turboshaft Engines Sand & Dust Erosion Considerations," AGARD, Erosion, Corrosion and Foreign Object Damage Effects in Gas Turbines, Quebec, Canada.

[8] Wall, S., John,W.,Wang, H. C., & Goren, S. L., 1990, "Measurements of kinetic energy loss for particles impacting surfaces," Aerosol Sci Tech, 12, pp. 926-946.

[9] Dahneke, B., 1975, "Further Measurements of Bouncing of Small Latex Spheres," J Colloid Interf Sci, 51(1), pp. 58-65.

[10] Greenwood, J. A., and Williamson, J. B. P., 1966, "Contact of Nominally Flat Surfaces," Proceedings of the Royal Society of London. Series A. Mathematical and Physical Sciences, 295(1442), pp. 300-319.

[11] Greenwood, J. A., and Tripp, J. H., 1967, "The Elastic Contact of Rough Spheres," Journal of Applied Mechanics, 34(1), pp. 153-159.

[12] Hisakado, T., 1974, "Effect of surface roughness on contact between solid surfaces," Wear, 28(2), pp. 217-234.

[13] Bush, A. W., Gibson, R. D., and Thomas, T. R., 1975, "The elastic contact of a rough surface," Wear, 35(1), pp. 87-111.

[14] McCool, J. I., 1986, "Closure to “Discussion of ‘Predicting Microfracture in Ceramics Via a Microcontact Model’” (1986, ASME J. Tribol., 108, pp. 385–386)," Journal of Tribology, 108(3), pp. 386-386.

[15] Chang, W. R., and Ling, F. F., 1992, "Normal Impact Model of Rough Surfaces," J Tribol-T Asme, 114(3), pp. 439-447.

[16] Chang, W. R., Etsion, I., and Bogy, D. B., 1987, "An Elastic-Plastic Model for the Contact of Rough Surfaces," J Tribol-T Asme, 109(2), pp. 257-263.

[17] Tabor, D., 1951, "The Hardness of Metals," Oxford Press.

[18] Tabor, D., 1948, "A Simple Theory of Static and Dynamic Hardness," Proceedings of the Royal Society of London. Series A, Mathematical and Physical Sciences, 192(1029), pp. 247-274.

[19] Johnson, K. L., 1985, "Contact Mechanics," Cambridge University Press.

[20] Thornton, C., 1997, "Coefficient of restitution for collinear collisions of elastic perfectly plastic spheres," J Appl Mech-T Asme, 64(2), pp. 383-386.

[21] Li, L. Y., Wu, C. Y., and Thornton, C., 2002, "A theoretical model for the contact of elastoplastic bodies," P I Mech Eng C-J Mec, 216(4), pp. 421-431.

[22] Wu, C. Y., Li, L. Y., and Thornton, C., 2005, "Energy dissipation during normal impact of elastic and elastic-plastic spheres," Int J Impact Eng, 32(1-4), pp. 593-604.

[23] Weir, G., and Tallon, S., 2005, "The coefficient of restitution for normal incident, low velocity particle impacts," Chem Eng Sci, 60(13), pp. 3637-3647.

[24] Vu-Quoc, L., and Zhang, X., 1999, "An elastoplastic contact force-displacement model in the normal direction: displacement-driven version," P Roy Soc Lond a Mat, 455(1991), pp. 4013-4044.

[25] Brach, R. M., and Dunn, P. F., 1992, "A Mathematical-Model of the Impact and Adhesion of Microspheres," Aerosol Sci Tech, 16(1), pp. 51-64.

[26] Bowling, R. A., 1988, "Particles on Surface 1:Detection, Adhesion and Removal," K.L. Mittal (Ed.), 2, 129, Plenum Press, New York, 78.

[27] Billings, C. E., Wilder, J., 1970, "Handbook of Fabric Filter Technology," Fabric Filter Systems Study, U.S Dept. H.E.W., GCA-TR-70-17-G.

[28] Clift, R., 1985, "I. CHEM. E. Symposium Series," 91, pp. 27-43.

[29] Hinds, W. C., 1982, "Aerosol Technology: Properties, Behavior, and Measurement of Airborne Particles," John Wiley, New York.

[30] C., H. S., 1957, "Energy absorbed by elastic waves during impact," J Mech Phys Solids, 8, pp. 162-171.

[31] Tillett, J. P. A., 1954, "A study of the impact on sphere of plates," Proc R Soc London, B69, pp. 677-688.

[32] Goldsmith, W., and Lyman, P. T., 1960, "The Penetration of Hard-Steel Spheres Into Plane Metal Surfaces," Journal of Applied Mechanics, 27(4), pp. 717-725.

[33] Bridges, F. G., Hatzes, A., and Lin, D. N. C., 1984, "Structure, stability and evolution of Saturn's rings," Nature, 309, pp. 333-335.

[34] Kharaz, A. H., Gorham, D. A., and Salman, A. D., 1999, "Accurate measurement of particle impact parameters," Meas Sci Technol, 10(1), pp. 31-35.

[35] Dahneke, B., 1971, "The capture of aerosol particles by surfaces," J Colloid Interf Sci, 37(2), pp. 342-353.

[36] Loeffler, F., 1973, "Adhesion Probablity in Fibre Filters," First World Filteration Congress, Paris.

[37] Rogers, L. N., Reed, J., 1984, "The adhesion of particles undergoing an elastic-plastic impact with a surface," Journal of Physics D: Applied Physics, 17(677), p. 6=.

[38] Mindlin, R. D. a. D., H., 1953, "Elastic Spheres in Contact Under Varying Oblique Forces," J Appl Mech-T Asme, 20, pp. 327-344.

[39] N. Maw, J. R. B., J.N. Fawcett, 1977, "The rebound of elastic bodies in oblique impact," Mechanics Research Communications, 4, pp. 17-22.

[40] Sommerfeld, M., 2003, "Analysis of collision effects for turbulent gas-particle flow in a horizontal channel: Part 1. Particle transport," Int J Multiphas Flow, 29(4), pp. 675-699.

[41] Sommerfeld, M., and Kussin, J., 2003, "Analysis of collision effects for turbulent gas-particle flow in a horizontal channel. Part II. Integral properties and validation," Int J Multiphas Flow, 29(4), pp. 701-718.

[42] Simonin, O., Zaichik, L. I., Alipchenkov, V. M., and Fevrier, P., 2006, "Connection between two statistical approaches for the modelling of particle velocity and concentration distributions in turbulent flow: The mesoscopic Eulerian formalism and the two-point probability density function method," Phys Fluids, 18(12).

[43] Jackson, R. L., Green, I., Marghitu, D. B., 2010, "Predicting the coefficient of restitution of impacting elastic-perfectly plastic spheres," Nonlinear Dynamics, 60(3), pp. 217-229.

[44] Hertz, H., 1896, "Miscellaneous Papers," Macmillan, New York.

[45] Jackson, R. L., and Green, I., 2005, "A Finite Element Study of Elasto-Plastic Hemispherical Contact Against a Rigid Flat," Journal of Tribology, 127(2), pp. 343-354.

[46] Quicksall, J. J., Jackson, R. L., Green, I., 2004, "Elasto-plastic hemispherical contact models for various mechanical properties," Journal of Engineering Tribology, 218(4).

[47] Etsion, I., Kligerman, Y., Kadin, Y., 2005, "Unloading of an elastic-plastic loaded spherical contact," International Journal of Solids and Structures, 42(13), pp. 3716-3729.

[48] Jackson, R., Chusoipin, I., and Green, I., 2005, "A finite element study of the residual stress and deformation in hemispherical contacts," J Tribol-T Asme, 127(3), pp. 484-493.

[49] Kharaz, A. H., and Gorham, D. A., 2000, "A study of the restitution coefficient in elastic-plastic impact," Phil Mag Lett, 80(8), pp. 549-559.

[50] Kogut, L., and Etsion, I., 2002, "Elastic-Plastic Contact Analysis of a Sphere and a Rigid Flat," Journal of Applied Mechanics, 69(5), pp. 657-662.

[51] Shankar, S., and Mayuram, M. M., 2008, "Effect of strain hardening in elastic–plastic transition behavior in a hemisphere in contact with a rigid flat," International Journal of Solids and Structures, 45(10), pp. 3009-3020.

[52] Tabakoff, W., Hamed, A., and Murugan, D. M., 1996, "Effect of target materials on the particle restitution characteristics for turbomachinery application," J Propul Power, 12(2), pp. 260-266.

[53] Reagle, C. J., Delimon J. M., Ng, W. F., Ekkad, S. V., 2013, "Study of Microparticle Rebound Characteristics Under High Temperature Conditions," Proceedings of ASME Turbo Expo 2013, San Antonio, Texas, USA.

Chapter 5

Particle Deposition Model for Particulate Flows at High Temperatures in Gas Turbine Components

This study proposes an improved physical model to predict sand deposition at high temperature in gas turbine components. This model differs from its predecessor[1] by improving the sticking probability by accounting for the energy losses during a particle wall collision based on our previous work[2]. This model predicts the probability of sticking based on the critical viscosity approach and collision losses during a particle-wall collision. The current model is novel in the sense that it predicts the sticking probability based on the impact velocity along with the particle temperature. To test the model, deposition from a sand particle laden jet impacting on a flat coupon geometry is computed and the results obtained from the numerical model are compared with experiments[3] conducted at Virginia Tech, on a similar geometry and flow conditions, for jet temperatures of 950 ^{o}C, 1000 ^{o}C and 1050 ^{o}C . Large Eddy Simulations (LES) are used to model the flow field and heat transfer, and sand particles are modeled using a discrete Lagrangian framework. Results quantify the impingement and deposition for 20-40μm sand particles. The stagnation region of the target coupon is found to experience most of the impingement and deposition. For 950 ^{o}C jet temperature, around 5% of the particle impacting the coupon deposit while the deposition for 1000 ^{o}C and 1050 ^{o}C is 17% and 28% respectively. In general, the sticking efficiencies calculated from the model show a very good agreement with the experiments for the temperature range considered.

5.1 Introduction

Jet engines are increasingly required to operate in hostile environments and thus exposed to fine particulate matter such as sand, ash and dirt. Particle ingestion can cause severe erosion of compressor blades and due to extremely high temperatures can soften and stick to turbine components in the hot gas path. Large amounts of particles can be ingested at takeoff and landing when engines are running at full power and are in ground proximity[4]. For an aircraft flying through volcanic dust clouds, particles can also be ingested at cruising altitudes[5]. Operation in these environments has led to serious aircraft accidents due to jet engine failures[6]. The problem of particulate ingestion in the engine has worsened with the use of high bypass ratio turbofan engines[7]. According to studies by Edwards and Rouse[8], high sand ingestion can reduce engine stability by eroding blade profiles and lowering the compressor efficiency, as a result of which the line of operation is closer to the surge line. The operating line also rises as a result of decrease in turbine efficiency or a reduction in nozzle throat due to glazing. The gas path immediately downstream of the combustor is a very critical region in this context where the particle deposition can lead to degradation of heat transfer, reduction in engine life and even midair engine failure. The components most likely to experience deposition are first stage nozzle guide vane, the hub, tip regions along with internal cooling circuits of these components where the coolant, the bleed air from the compressor, can carry along with it significant amount of particulate matter. To accurately predict the extent of damage to these turbine components, it is important to identify and understand the underlying physical processes that lead to deposition.

Different aspects of the problem of sand and volcanic ash ingestion have been studied in the past, with the majority of the work focused on erosion and deposition of particles on a wide range of materials and under different operating conditions. It is very likely that a critical threshold temperature exists between erosion dominated and deposition dominated regimes. As the temperature increases the particles soften or become molten leading to increase in agglomeration rates with associated decrease in blade erosion rates and increase in deposition[9]. For aircraft engines this observed critical temperature for deposition is between 980 ^{o}C and 1150 ^{o}C[9-11]. This temperature threshold for deposition is still well below the turbine inlet temperature (TIT) of gas turbine engines.

Experiments have shown that ash deposition is sensitive to turbine inlet gas temperatures [4, 12, 13] which can be in the range of 1600–1900 K. Bons and co-workers have conducted extensive amount of research to investigate factors influencing flyash particle deposition in gas turbine components. Jensen et al.[14]described the Turbine Acceleration Deposition Facility (TADF) used to study the deposition of ash particles on the first stage turbine blades in land based turbines. The surface topography of the accelerated deposits closely resembled that of actual turbine blades under up to 25000 hours of service. For test conditions, the observed temperature threshold for accelerated deposition was between 900 ^{o}C and 1100 ^{o}C. Bons et al.[13] presented a comparative analysis of various alternative fuels like sawdust ash, coal, straw ash and petcoke at actual engine conditions. The particles injected had a mass mean diameter of 10 – 20 µm. For the same particle loading, coal and petcoke showed orders of magnitude higher deposition compared to biomass fuels. They observed penetration of particles into the cracks of the thermal barrier coating (TBC), consequently hampering the performance of the blade material system. Wammack et al.[15] investigated the physical characteristics of the evolution of surface deposition on a turbine blade at a gas temperature and velocity representative of first stage high pressure turbine. Their experiments concluded the following: first, the deposit roughness height and shape experience a temporary lull in growth during the deposit evolution. Second, the initial surface roughness has a significant effect on deposit growth. Third, thermal cycling combined with particle deposition caused extensive TBC spallation while thermal cycling alone caused none. Hence the deposit penetration into the TBC was a significant contributor to spallation. Crosby et al.[16] then studied the effect of particle size, gas temperature and metal temperature on the deposition from coal derived fuels. The main conclusions from their study are as follows. First, deposition rates were more than doubled as the mass mean diameter of the particle was increased from 3 μm to 16 μm. Second, particle deposition decreased with decreasing gas temperature and increased coolant flow. The threshold gas temperature at which ash particle deposition initiates was found to be approximately 960 °C. Furthermore, they showed decrease in TBC damage as the cooling levels were increased.

Anderson et al.[17] studied adhesion characteristics of flyash on a heated target for normal impingement. The observed sticking coefficients between 0.04 and 0.10 for bituminous coal ash. Ahluwalia et al.[18]investigated the adherence of flyash particles (15 and 40 microns) on a wedge shaped target (10°, 30° and 45°). The inferred sticking coefficients ranged from 0.04 to 0.11 at 1325 K gas temperature and from 0.0003 to 0.01 at 1256 K gas temperature. The sticking coefficient also increases with surface temperature but was found insensitive to the impact angle. These observations were further confirmed by studies from Wenglarz and Fox[12, 19]. Kim et al.[5] conducted experiments investigating the effects of volcanic ash on turbine components and found that film cooling holes are susceptible to deposition and clogging. Dunn et al.[20] also reported that particulate deposition can clog film cooling holes and hence deposition is a major issue for modern aircraft engines. Walsh et al.[21] studied the effect of sand ingestion on film cooling hole blockage, using a leading edge coupon over a range of sand particle size, particle loading and metal temperatures. Metal temperatures were shown to be the most important parameter for particle deposition. At temperatures above 1000 °C, sand particles started melting and promoted blocking of cooling holes. Land et al.[22] investigated a double walled cooling design to reduce sand blockage. It was found that impingement air-flow holes and staggered arrangement of cooling holes could aid in breaking up of larger particles to pass through cooling holes. All these studies imply that the physical state of particles plays a decisive role in the particle deposition.

To account for observed influences of various ash composition and temperature on deposition, Walsh et al.[23] used particle viscosity as a means to measure the physical state of the particle. They assumed that the sticking probability of the particle is inversely proportional to the viscosity of the particle and below a threshold viscosity the particle will stick with certainty. Huang et al.[24] also used a similar viscosity approach to predict the deposition of flyash particles. The model calculates the particle viscosity based on the chemical composition and the temperature of the flyash particles. An empirical value of reference or critical viscosity for a given ash sample is chosen, which then governs deposition of the flyash particles. If the ash particle viscosity is less than the reference viscosity then they are assumed to deposit upon impact. The deposition results showed good agreement with experiments for a class of fouling coal ash samples. An alternative to this approach is to use melt fractions. Ash particles are assumed to deposit when they acquire a minimum percentage of melt fraction (anywhere from 15% to 30%). Particle temperatures are computed for a range of melt fractions that form sticky particles. Zhou et al.[25] studied the deposition of hot molten flyash particles (0.27 μm, 8 μm and 58 μm) on a circular cooled probe. Their numerical deposition model, similar to Hansen et al.[26] and Kær[27] assumed particles to stick when the melt fraction was in the range of 10–70%. The particles above 70% were assumed to form molten slag. El-Batsh[28] developed a sticking model to investigate particle sticking and detachment on turbine blades. The model was used for a numerical investigation of the effect of ash particle deposition on the flow field through turbine cascades. This model was further modified and calibrated to match experimental results by Ai et al.[29], for their ash deposition study on a 45^{o} inclined flat plate with film cooling. However, to account for temperature changes in the deposition model, in a separate study, they developed a correlation of Young's modulus as a function of temperature by calibrating their deposition simulations with experimental data. This semi-empiricism in the deposition model showed good agreement with experimental results. Results showed that the capture efficiency increases with increasing blowing ratio. More recently, Sreedharan and Tafti[1] proposed an improved sticking model based on the critical viscosity approach of Walsh[23] and using the coal ash composition to determine the sticking probability of ash particles. To validate the model, deposition of ash particles impacts on a 45 degree wedge target are computed numerically and compared with the experimental data of Crosby[30]. The developed model was further extended to investigate deposition on the leading edge of a film-cooling turbine vane[31].

5.2 Objective

The objective of this study is to develop a particle deposition model based on the state of the impacting particle and the impacting parameters of velocity and angle of impact. This model builds upon the previous sticking model presented by Sreedharan and Tafti[1]. This study is novel in that it is the first study that accounts for the energy losses during an impact along with change in the physical state of particle due to change in the temperature, to predict the probability of sticking. In order to validate this model, numerical simulations of sand deposition were conducted on a flat plate coupon for a normal jet impingement. The deposition results were compared against experiments conducted at Virginia Tech. on identical geometry. This model facilitates the future studies on dynamics of sand deposition in hot gas path components in gas turbine engines.

5.3 Methodology

5.3.1 Deposition Model

In our previous work[1], a particle composition dependent deposition model was developed for prediction of syngas ash deposition in turbine hot gas path. The model predicts the sticking of a particle based on the particle composition and the particle temperature during an impact. The predictions showed good agreement with the measurements over a range of temperatures for ash and PVC particles. One shortcoming of this model and previous critical viscosity models is that it assumes only the physical state of the particle (temperature) to be the dominating factor in determining the sticking probability. This assumption is valid at very high temperatures when the particle has softened and is already sticky. However, at lower temperatures the energy losses due to impact of the particle with surface will determine if an impacting particle will be able to leave the surface. These energy losses are a function of impact parameters such as properties of particle/surface, impact velocity and angle. In order to account for these energy losses due to collision, an improved model is proposed in this study which accounts for both the mechanisms of collision losses and particle temperature, to predict final sticking probability.

5.3.2 Calculating the Sticking Probability of Sand

This model is an improvement upon our previous model of critical viscosity model by including the effect of impact velocity and angle along with temperature of the particle, on deposition. The model assumes that probability of sticking is a function of the fraction of the kinetic energy lost by the particle during an impact. Coefficient of restitution (e), the ratio of rebound velocity to the impact velocity, is a parameter which encapsulates all the energy losses incurred by the particle during a collision. Our previous work[2] proposed a model to predict the coefficient of restitution for sand particles in gas turbine components based on deformation and adhesion losses during a particle wall collision. Figure 5.1 shows the model prediction for coefficient of restitution for sand particle with normal impact velocity.

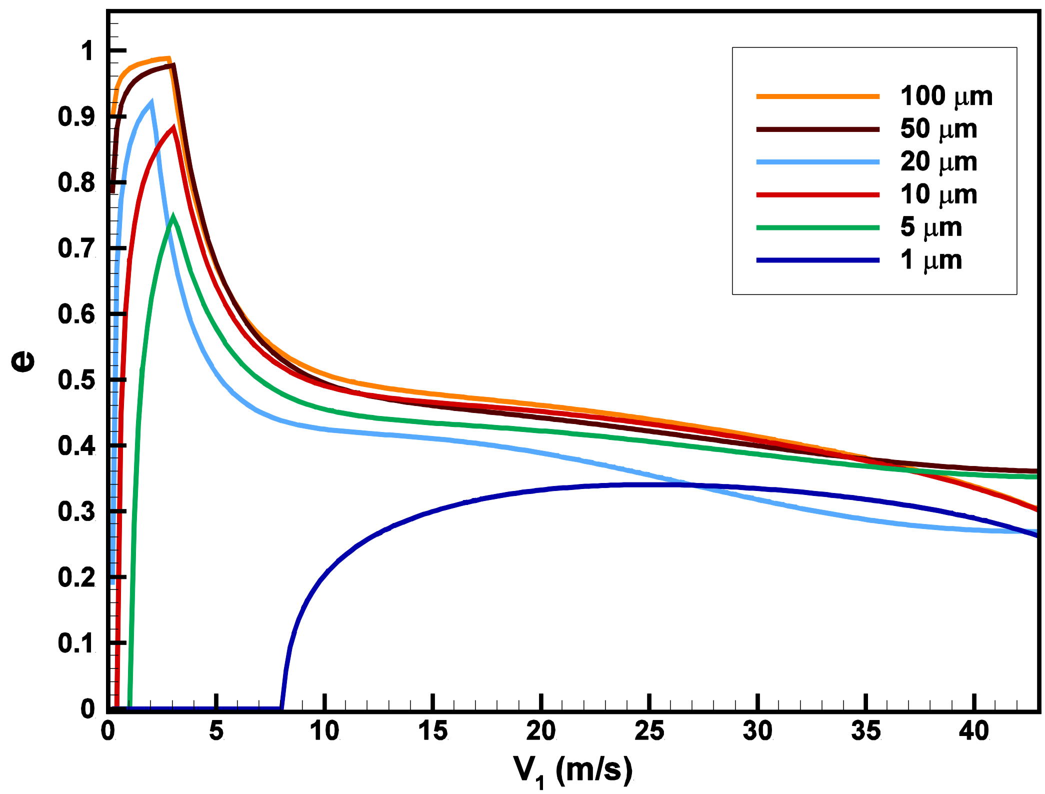

Figure 5.1 Coefficient of restitution for different particle sizes with normal impact velocity

The final coefficient of restitution can be written as

$$e_n = \frac{V_{2n}}{V_{1n}} = e_{ep}\left(1 + 2W_A / e_{ep}^2 m V_{1n}^2\right)^{1/2} \tag{1}$$

$$e_t = \frac{V_{2t}}{V_{1t}} = 1 - \mu \tan\alpha\left(1 + e_{ep}\left(1 + 2W_A / e_{ep}^2 m V_{1n}^2\right)^{1/2}\right) \tag{2}$$

$$e = \frac{V_2}{V_1}, \quad e_n = \frac{V_{2n}}{V_{1n}}, \quad e_t = \frac{V_{2t}}{V_{1t}} \tag{3}$$

where V_1 is the magnitude of the impact velocity and V_2 is magnitude of the rebound velocity. e_{ep} is coefficient of restitution after adhesion losses, W_A is work of adhesion, μ is coefficient of friction as discussed in our previous work[2]. Total coefficient of restitution, e, can be written in terms of e_n and e_t:

$$\text{Since } V_2 = \sqrt{V_{2n}^2 + V_{2t}^2} \tag{4}$$

$$\Rightarrow e = \sqrt{\frac{e_n^2 \tan^2\alpha + e_t^2}{\tan^2\alpha + 1}} \tag{5}$$

The probability of sticking should be a function of energy losses during a collision and is calculated from coefficient of restitution model as $P_e = f(e)$. Multiple relations were tried for sticking probability as a function of coefficient of restitution, and finally an exponential function was chosen such that the sticking probability based on e, becomes significant only when the particle loses more than half the initial kinetic energy during impact.

$$\text{Starting with } P_e = \exp(-c.e) \tag{6}$$

$$\text{if} \quad \mathrm{P}_e = 0.0 \; for\, 1 - e^2 \le 0.5 \;\; i.e. \;\; e \ge 0.707 \tag{7}$$

$$\Rightarrow c \approx 6.5 \;\; \Rightarrow P_e = 0.01 \;\; for \;\; e = 0.707 \tag{8}$$

Figure 5.2 shows the variation of P_e with e when the exponential function is used :

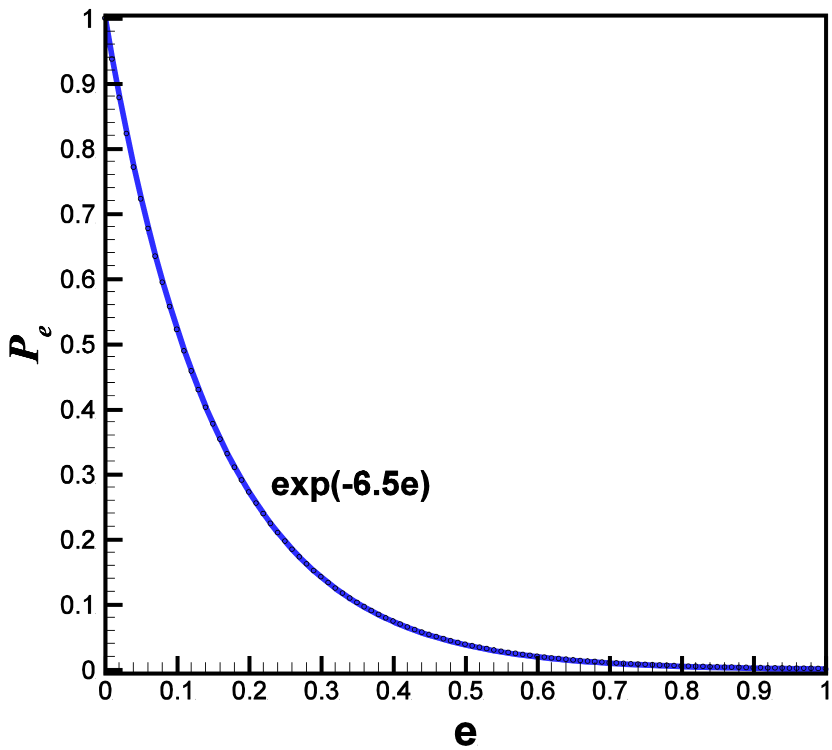

Figure 5.2 Probability of sticking as a function of coefficient of restitution

Probability of sticking (P_{visc}) is also calculated based on the critical viscosity model[1] to include the effect of temperature. This model assumes that sticking probability increases with decrease in viscosity of the particle as temperature increases. Above a critical temperature or the softening temperature (T_{soft}), the viscosity rapidly decreases and below this critical viscosity (μ_{cr}) sticking probability is assumed to be unity. Below the softening temperature sticking probability is calculated based on the following equation:

$$P_{visc} = \frac{\mu_{cr}}{\mu_T},\ \mu_{cr} = \mu_{soft} \tag{9}$$

where μ_T is the viscosity of the particle at the particle temperature. Sand is composed of multiple inorganic compounds and varies substantially with the type and source of sand, and a model by

Senior and Srinivaschar[32] is used to compute the sand viscosity as a function of temperature. The model was developed for ash and categorizes ash into constituents that increase the viscosity, constituents that decrease the viscosity, and some constituents which do both. Viscosity of the sand particle is calculated from the particle temperature from the following equation:

$$\log\left(\frac{\mu}{T}\right) = A + \frac{10^3 B}{T} \tag{10}$$

The terms A and B are calculated from the sand composition[32]. The softening temperature of the sand is calculated based on sand composition from an empirical relation proposed by Yin et al.[33].

Since the critical viscosity model was essentially developed for ash particles and is a composition based model, it can be used for sand particles if the composition is comparable. This was verified by comparing the composition of sand with different ash samples (Table 5.1).

Table 5.1 Chemical composition of some coal ash samples and sand[1]

	Lethabo	HN115	KL1	WY	ILL	Pitt	ND	ExBC	**Sand**
SiO_2	60.33	42.3	47.1	35.59	46.62	50.37	23.68	55.44	**68-76%**
Al_2O_3	29.73	34.5	35.3	15.15	14.41	21.04	7.94	18.39	**10-15%**
Fe_2O_3	2.68	6.17	4.72	7.53	26.80	21.23	9.82	5.00	**2-5%**
TiO_2	1.37	2.24	1.9	1.40	0.73	1.14	0.47	1.46	**0.5-1%**
P_2O_5	0.41	0.55	0.19	3.02	1.00	0.90	3.85	2.00	**-**
CaO	3.58	8.55	5.67	18.92	2.74	1.37	18.43	6.66	**2-5%**
MgO	1.19	1.00	0.75	4.76	0.72	0.65	7.44	3.26	**1-2%**
Na_2O	0.14	0.21	0.26	2.10	0.88	0.53	10.20	5.09	**2-4%**
K_2O	0.45	0.76	1.33	1.01	3.15	2.00	1.35	1.71	**2-5%**
S	0.10	0.04	0.03	10.53	2.94	0.78	16.82	0.98	**-**
MnO	0.02	0.00	0.00	0.00	0.00	0.00	0.00	0.00	**-**
T_{soft} (°C)	1453	1360	1500	1150	1457	1184	1057	1278	**1000-1200**

Based on the sand composition, the calculated softening temperature of sand lies in the range 1000 °C-1200 °C. For all the calculations in this study softening temperature is selected to be 1120 °C. This implies that temperature does not affect deposition at temperatures much lower than 1120 °C. Any deposition much below this temperature is due to energy losses due to deformation and adhesion losses. Figure 5.3 shows the sand viscosity variation as a function of temperature and compared with different ash samples[1]. Figure 5.4 shows the probability of sticking for sand particles based on viscosity $\left(P_{visc}\right)$ with temperature. Sticking probability rises exponentially as the particle approaches softening temperature.

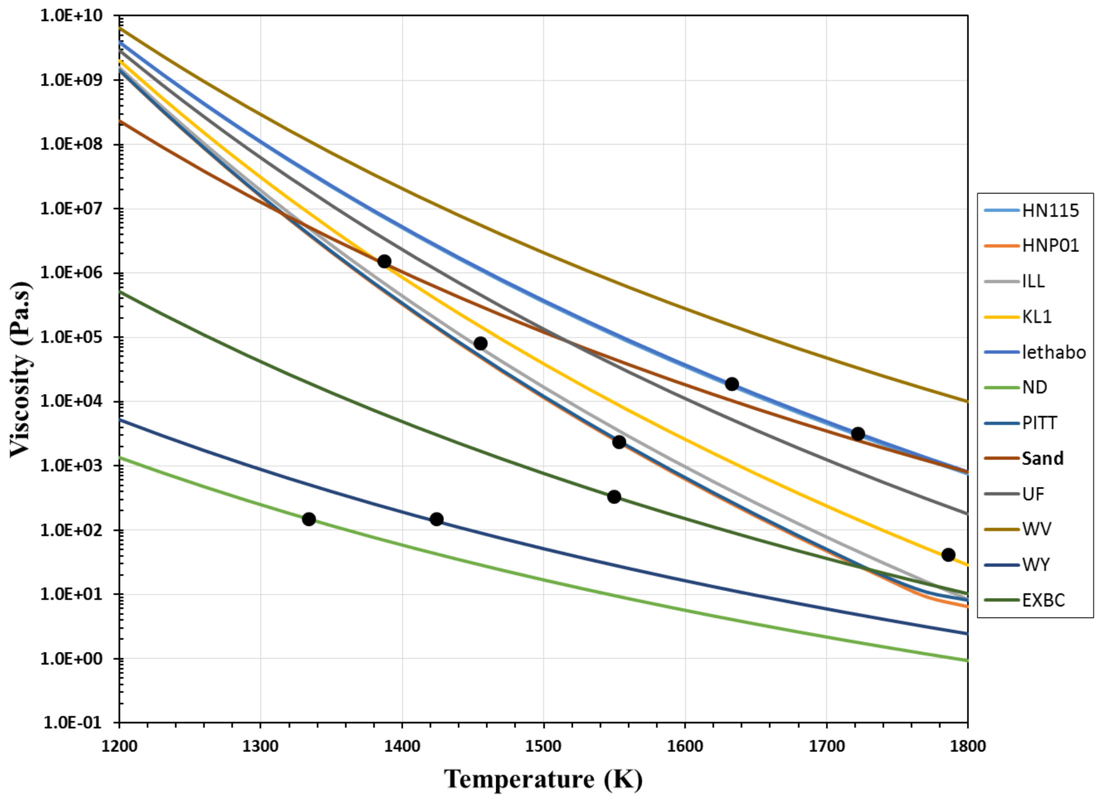

Figure 5.3 Viscosity variation with temperature for different ash samples and sand, black circles indicate the softening temperature

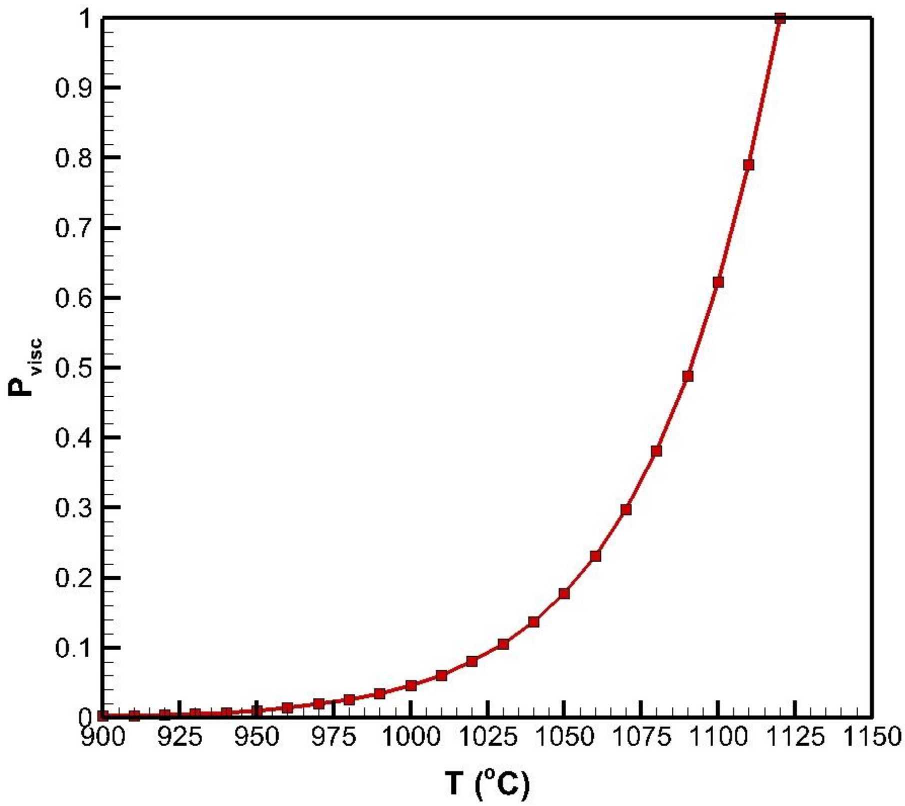

Figure 5.4 Probability of sticking based on viscosity (P_{visc}) with temperature

The current model emphasizes that both the mechanisms, the collision losses and the change in physical properties with temperature, should be accounted for to calculate the final sticking probability. The final probability of sticking is calculated based on above two sticking probabilities as:

$$P = \min\{P_e + P_{visc}, 1\} \tag{11}$$

The above equation simply means that depending upon the collision conditions, either of the two mechanisms can dominate the deposition or both mechanisms can combine together to determine deposition. For example, if the particle temperature is near sticking temperature, viscosity effect will dominate (high P_{visc}) while at much lower temperatures collision losses will dictate deposition.

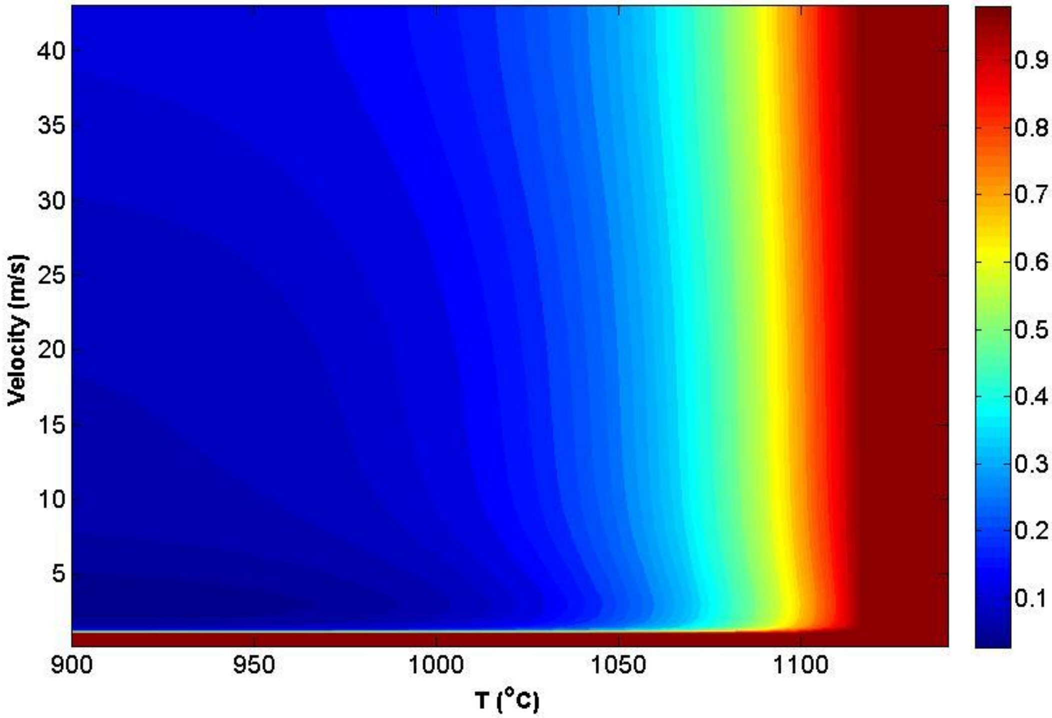

(a)

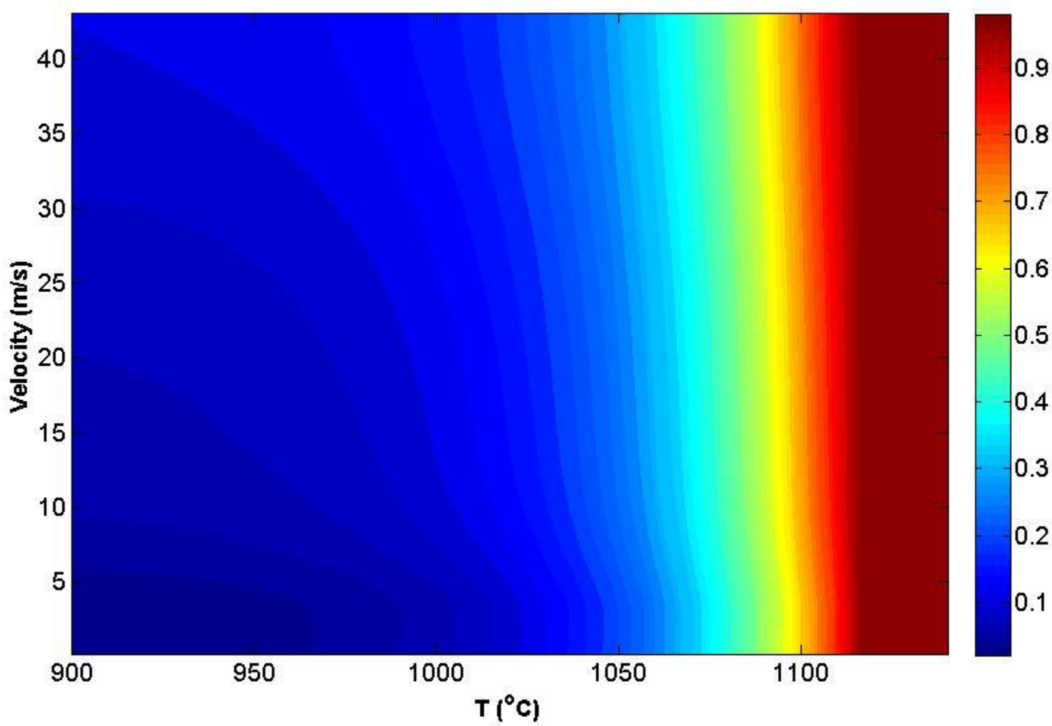

(b)

Figure 5.5 Sticking probability contours (a) 5 microns (b) 50 microns

There will still be a temperature range where the particle will be sticky but not enough to deposit, yet could have lost sufficient kinetic energy such that the combined probability of sticking is high. To discuss the effect of particle size on deposition, figure 5.5 shows the final sticking probability contours for two different particle sizes of 5 microns and 50 microns. It shows that for smaller 5 µm particles, even at temperatures much lower than the softening temperature the sticking probability is high at low velocities. This can be attributed to the observation that for smaller particles at lower velocity the energy losses can become significant due to low initial kinetic energy and hence leading to a much lower coefficient of restitution and higher sticking probability[2]. For larger particles of 50 µm, the collision losses only become significant at higher velocities. The contours also show that at temperatures below sticking temperatures, there can be a significant probability of sticking and deposition due to collision losses.

The above developed deposition model is used in the simulations to model sand particle laden jet impingement on a coupon at jet temperatures of 950 ^{o}C, 1000 ^{o}C and 1050 ^{o}C.

5.3.3 Experimental Setup

The Aerothermal Rig used in this study was donated to Virginia Tech by Rolls-Royce in September 2010. Before that, the rig was used at the Rolls-Royce in their Indianapolis, IN facility for various heat transfer studies. Hylton et al.[34] used the same facility to conduct a series of tests on shower head and film cooling heat transfer at a temperature of 700 K. Nealy et al.[35] used the rig to investigate heat transfer on nozzle guide vanes at different transonic Mach numbers. The operational specifications for this rig when installed in Indianapolis, IN were reported as 2.2 kg/s at a maximum of 16 atm and 2033 K by Rolls-Royce.

For the current study, the Aerothermal Rig had to be reconfigured to allow for sand injection as seen in figure 5.6. The rig was also used previously by Reagle[36, 37] to investigate sand particle impacts on a coupon at temperatures lower than 1073 K. Since the work by Reagle, the equilibration tube has been changed to allow for a higher operating temperatures. The current maximum test section temperature of the rig constrained by the limits of the uncooled equilibration tube is around 1323 K.

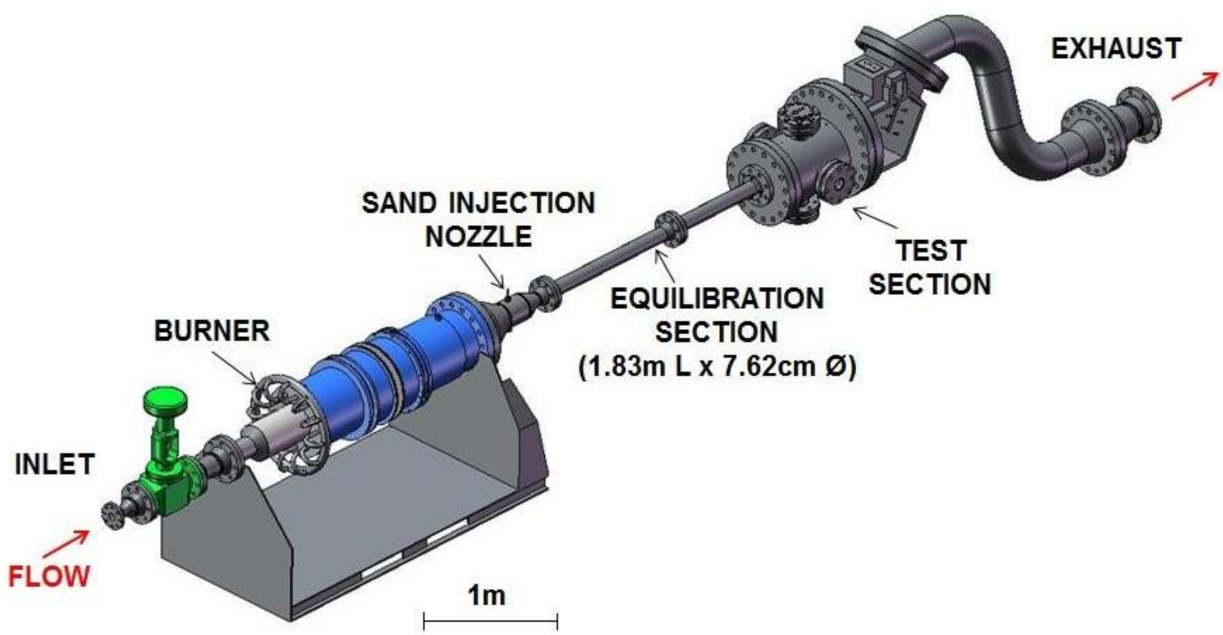

Figure 5.6 VT Aerothermal Rig configured for sand ingestion testing

A compressor supplies air to the rig at a constant rate of 0.15 kg/s. The flow is regulated upstream with a series of regulator valves, such that a constant jet velocity of 70 m/s is maintained. The air is then heated up as it passes through a sudden expansion burner. At the burner exit, the flow cross-section diameter is reduced from 30.5 cm to 7.62 cm. Test particles are injected into the mainstream flow in this contraction section. The injected particles get entrained in the compressed and heated mainstream flow. The particles laden flow then passes through a 1.83 m long, 7.62 cm diameter equilibration tube which enables particles of various sizes to accelerate to the same speed and temperature as the rest of the flow. The flow exits the equilibration tube as a free jet into the test section and impinges on the surface of the test coupon. The Pitot-Static probe survey was taken at a distance of 8.13 cm upstream from the coupon face to verify the fully developed velocity profile. For each test, a sufficient amount of time is allowed for the temperature of the rig to reach an equilibrium before the sand particles are injected and measurements of the particles are taken.

The test section contains a rectangular test coupon, on which the particles impact, and a support to allow for rotation of the coupon. The test section has a laser access port and an optical access for the camera to image the area in front of the coupon. The test coupon has a height of 3.81 cm and is 6.35 cm long as shown in figure 5.7. The coupon is made from Hastelloy X, a high temperature nickel alloy and can be rotated 360 degrees in 10 degree increments.

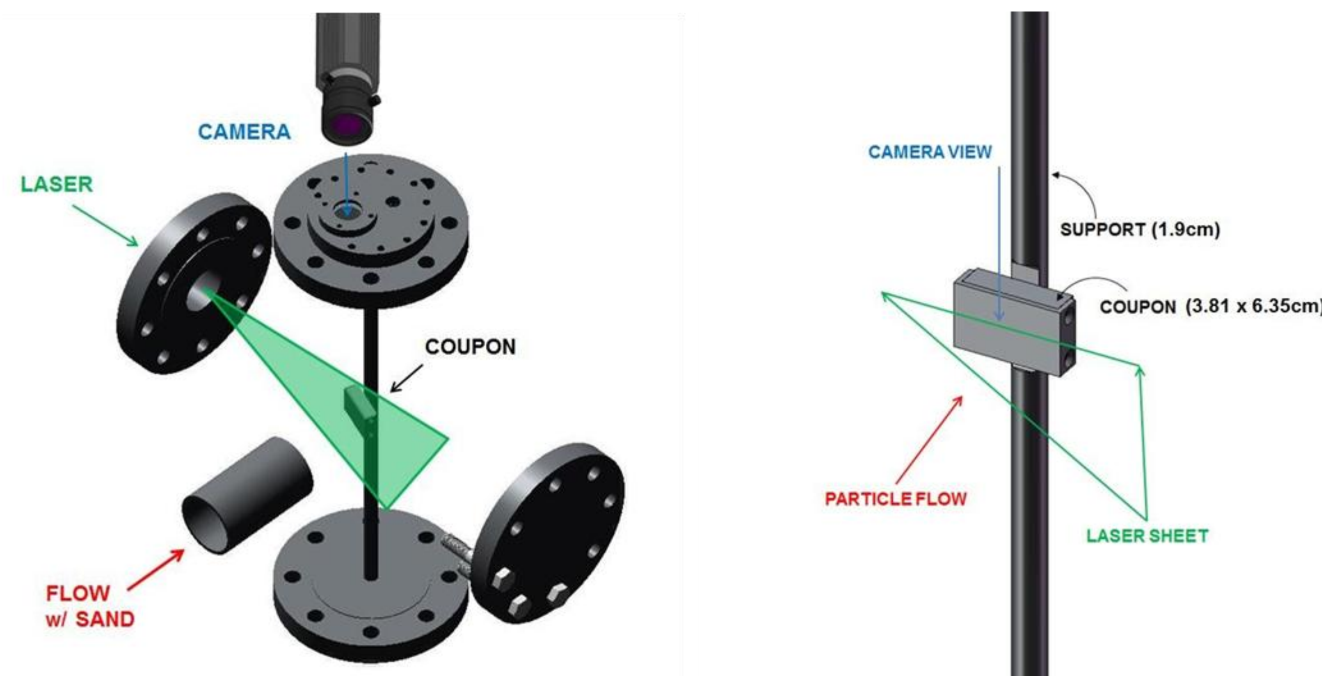

Figure 5.7 Schematic of instrumentation and test coupon setup

Arizona Test Dust (ARD) sand particles of nominal size range 20-40 µm were tested in this experiment for deposition. It is an excellent choice for studying sand ingestion in jet engines as it is has very similar properties to sands found throughout the world and is readily available. A twin head Litron Nd:YAG laser is used for illuminating particles and emits approximately 135 mJ at 532 nm wavelength. The laser is capable of emitting two pulses of light within a few microseconds. The laser light is projected in a plane at the center of the test coupon as shown in fig. 6. A Dantec Dynamics® FlowSense camera equipped with a Zeiss® Makro-Planar 2/50 lens is used to capture the particle images at 2048x2048 resolution. Both the laser and the camera are synced by a timer box ensuring illumination and imaging occur concurrently.

Data Reduction

The particle tracking and data reduction method developed by Reagle and Delimont [38, 39] is used to record the particle impacts and deposition. Data was recorded for impacts of 20-40 µm ARD impacting the coupon for angles ranging from 30° to 80° for different jet temperatures. In the reduction method used, there is a limit to how far a particle may be from the coupon surface to still be used in data reduction scheme. The particles can be up to 2 cm from the point of impact to be counted for analysis. Hence, it should be noted that the data reduction method does not calculate the deposition directly by counting the number of particles deposited on the coupon surface. The particles tracked in the plane of examination, near the surface are characterized as impacting or rebounding particles based on the velocity direction. The rebound ratio is defined as the ratio of the number of particles rebounding to the number of particles impacting the surface. It is very challenging to track every single particle, however, an estimate of rebound ratio can be made based on number of particles tracked in the plane of the laser sheet only. Along with uncertainties in estimating the number of impacting/rebounding particles, there is also some uncertainty involved due to the particles rebounding out of or in to the plane of examination. The data reduction method also assumes a mean diameter of 26 µm for all the particles and not the particle size distribution.

5.3.4 Geometry

A flat coupon similar to the experiments is used to test the deposition model. The experiments investigate coupon for angles ranging from 30° to 80° for different jet temperatures, but numerically only two angles of 45° and 90° are simulated. The geometry and grid resolution for both these cases is very similar and hence, only 90° case is used to discuss geometry and grid. The flat plate coupon is simulated by a semi-infinite body as shown in figure 5.8 and figure 5.9. The inlet tube is $8D_h$ long and has a square cross-section with side D_h. The target coupon is also a square plate with side $0.7D_h$ with flat after-body. The target surface is in line with the inlet tube, such that the particle laden jet hits the surface normally. The gap between the inlet tube exit and target coupon is $0.8D_h$. The computational domain extends $18.8D_h$ in streamwise direction and $10D_h$ for the other two directions.

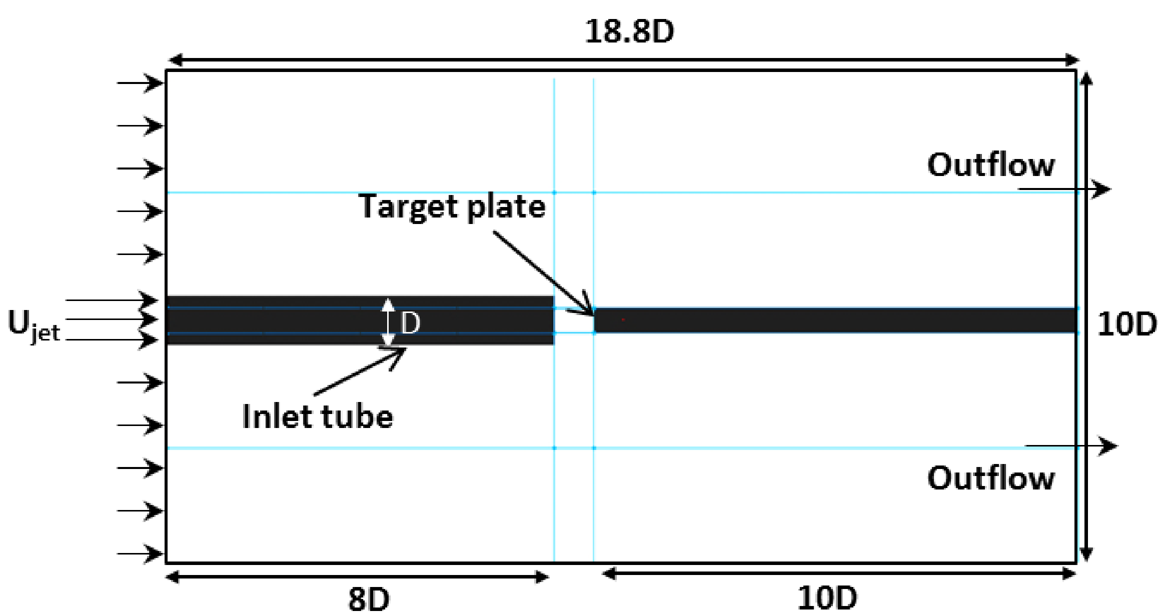

Figure 5.8 Computational domain, side view

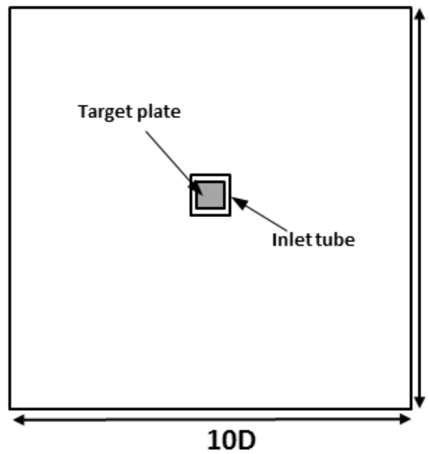

Figure 5.9 Computational domain, front view

5.3.5 Solution Method

Wall Modeled Large-Eddy Simulations (WMLES) are used to calculate flow and temperature fields. A Lagrangian approach is used to calculate particle dynamics in which each individual particle is tracked in the flow field based on a dynamic equation. The governing equations consisting of the incompressible mass, momentum and energy conservation are solved in a generalized body-fitted coordinate system. The equations are non-dimensionalized using a characteristic length scale $\left(L_c\right)$ as the hydraulic diameter of inlet tube, characteristic velocity scale as the jet inlet velocity $\left(U_{jet}\right)$, and a characteristic temperature scale $\left(T_{jet} - T_a\right)$. The non-dimensional time dependent equations are written as follows:

Continuity:

$$\frac{\partial}{\partial \xi_j}\left(\sqrt{g}\,\overline{U}^j\right) = 0 \qquad (12)$$

Momentum:

$$\frac{\partial}{\partial t}\left(\sqrt{g}\overline{u}_i\right)+\frac{\partial}{\partial \xi_j}\left(\sqrt{g}\overline{U}^j\overline{u}_i\right)+\frac{\partial}{\partial \xi_j}\left(\left(\frac{1}{\mathrm{Re}}+\frac{1}{\mathrm{Re}_t}\right)\sqrt{g}g^{jk}\frac{\partial \overline{u}_i}{\partial \xi_k}\right)=-\frac{\partial}{\partial \xi_j}\left(\sqrt{g}\left(\vec{a}^j\right)_i\overline{p}\right) \qquad (13)$$

Energy:

$$\frac{\partial}{\partial t}\left(\sqrt{g}\overline{\theta}\right)+\frac{\partial}{\partial \xi_j}\left(\sqrt{g}\overline{U}^j\overline{\theta}\right)=\frac{\partial}{\partial \xi_j}\left(\left(\frac{1}{\mathrm{Pr}\,\mathrm{Re}}+\frac{1}{\mathrm{Pr}_t\,\mathrm{Re}_t}\right)\sqrt{g}g^{jk}\frac{\partial \overline{\theta}}{\partial \xi_k}\right) \qquad (14)$$

where $\vec{a}^i$ are the contravariant basis vectors, $\sqrt{g}$ is the Jacobian of the transformation, $g^{(ij)}$ is the contravariant metric tensor, $\sqrt{g}U^j=\sqrt{g}\left(\vec{a}^j\right)_i u_i$ is the contravariant flux vector, u_i is the Cartesian velocity vector, and θ is the non-dimensional temperature. The overbar in the continuity, momentum and energy equations denote grid filtered quantities. Re_t is the inverse of the non-dimensional turbulent eddy-viscosity and is obtained by the Smagorinsky model.

$$\frac{1}{\mathrm{Re}_t}=C_s^2\left(\sqrt{g}\right)^{(2/3)}\left|\overline{S}\right| \qquad (15)$$

where $\left|\overline{S}\right|$ is the magnitude of the strain rate tensor given by $\left|\overline{S}\right|=\sqrt{\left(2\overline{S}_{ik}\overline{S}_{ik}\right)}$. The Smagorinsky constant C_s^2 is obtained via the dynamic procedure[40]. The turbulent Prandtl number is assumed to have a constant value of 0.5[41]. The details on the near wall modeling approach can be found in our previous work[42].

The particles or the dispersed phase is modeled in the Lagrangian framework. The model currently used has been described in our previous work[43]. The model is implemented in an unstructured multiblock, multiprocessor framework and validation in turbulent channel flow has been reported in our earlier studies[44]. The particle sizes investigated in this study are in the range of 20 - 40 μm. In this range of particle sizes, among all the forces acting on the particle, drag force dominates the particle motion[45]. Additionally, in practical situations the concentration of sand particles are very dilute in the mainstream, hence inter particle interactions and particle-to-fluid interactions are neglected. It is also assumed that subgrid scales have negligible effect on particle transport [46, 47]. The equations for particle motion and temperature in non-dimensional form are as follows:

Motion:

$$\frac{du_i^p}{dt} = -\frac{1}{St_p}\left(1+0.15\,\mathrm{Re}_p^{0.687}\right)\left(u_i^p - u_i^f\right) \tag{16}$$

Location:

$$\frac{dx_i^p}{dt} = u_i^p \tag{17}$$

Energy:

$$\frac{d\theta^p}{dt} = \frac{1}{St_{conv}}\left(\theta^f - \theta^p\right) - \frac{1}{St_{rad}}\left(\theta^p\right) \tag{18}$$

where St_p is the particle momentum Stokes number defined as $St_p = \left(\rho_p^* d_p^{**2} U_{jet}^*\right) / \left(18\mu L_c^*\right)$, St_{conv} is the particle convective thermal Stokes number defined as $St_{conv} = \left(\rho_p^* C_p^* d_p^{**} U_{jet}^*\right) / \left(6hL_c^*\right)$, St_{rad} is the particle radiative thermal Stokes number defined as $St_{rad} = \left(\rho_p^* C_p^* d_p^{**} U_{jet}^*\right) / \left(6h_r L_c^*\right)$, with the effective radiative heat transfer coefficient defined as $h_r = \varepsilon\sigma\left(T_p + T_a\right)\left(T_p^2 + T_a^2\right)$. L_c^* is a characteristic length, which is the hydraulic diameter of the inlet tube in this case.

5.3.6 Computational Grid

A structured grid is created using multi-block topology. The total grid size is 17 million cells and the spacing of grid points is shown in the figure 5.10. The first node y+ values on the walls are around 35 as par the wall model requirements.

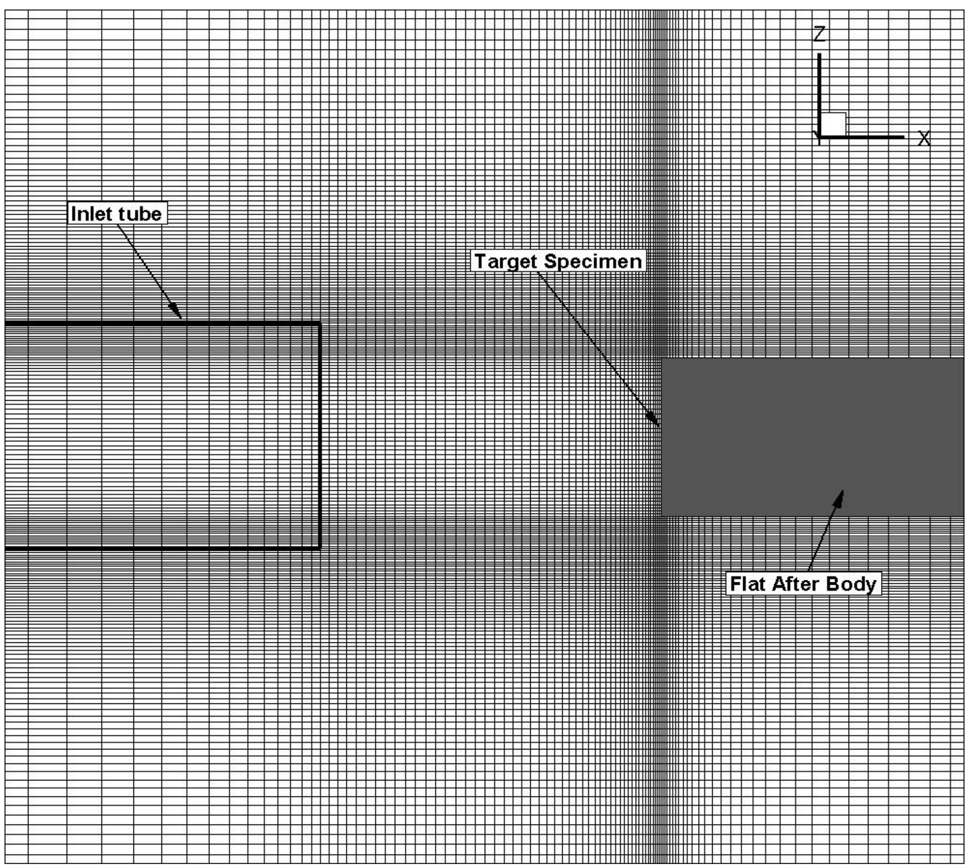

(a) Side View

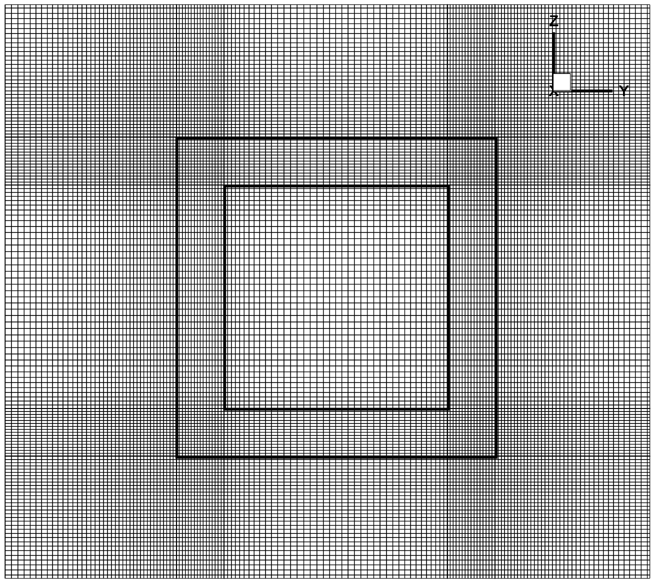

(b) Front View

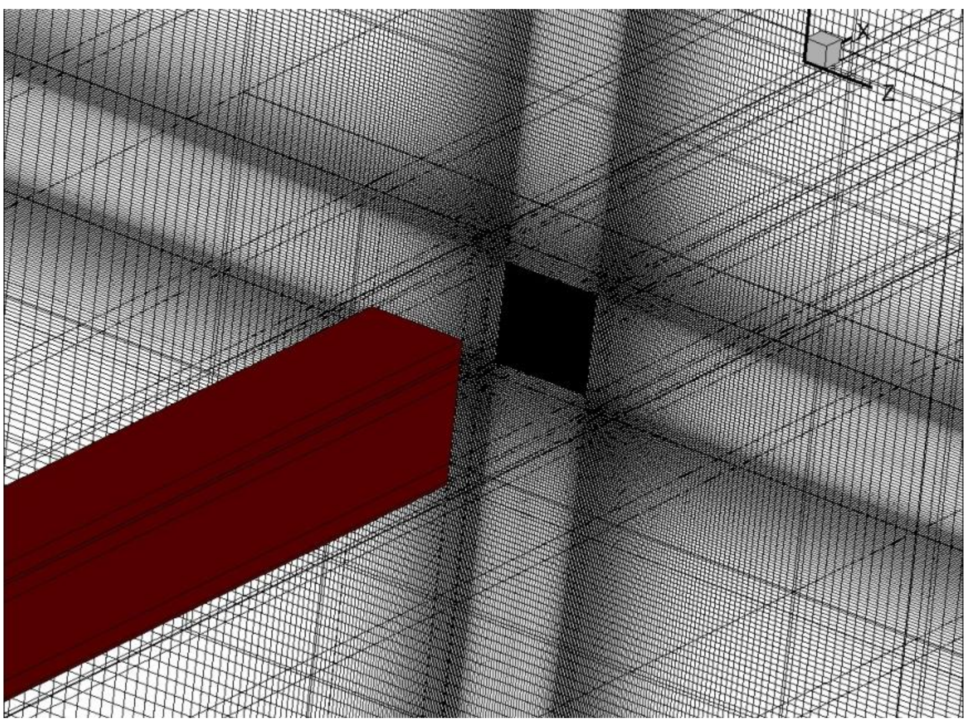

(c) Isometric View

Figure 5.10 Grid in the vicinity of inlet tube exit and coupon

5.3.7 Boundary Conditions

The goal of the current calculations is to simulate the flow field, heat transfer, particle transport and the deposition in the coupon experiments conducted at Virginia Tech. The target coupon plate is square shaped as opposed to experiment which use rectangular coupon as discussed before. This was done to reduce the computational grid complexity in the present structured multi-block grid framework. Except near the edges of the target plate, this simplification does not alter the bulk flow and particulate deposition quantities. The mean Reynolds number in the calculation based on mean bulk velocity in the inlet tube and inlet tube side is 30,000, which is also the case in the experiments.

The non-dimensional velocity $\left(U_{jet}\right)$, in the inlet tube is set to 1 and the velocity $\left(U_a\right)$ of the fluid surrounding the inlet tube is set to 1.0 × 10^{-10} to simulate ambient conditions. Constant uniform velocity profile is used at the inlet, normal to the boundary. The calculations are run at three different jet temperatures of 950 ^{o}C, 1000 ^{o}C and 1050 ^{o}C. In the experiments, the coupon temperature is found to be 80-140 ^{o}C lower than the jet temperature for the three cases. Constant wall temperature boundary conditions are used on all the surfaces. The coupon temperature is set to the values observed in the experiments. The inlet tube wall temperature is also set 100 ^{o}C below the jet temperature as observed in experiments. The non-dimensional temperature $\left(T_{jet}\right)$ at the tube inlet is set at 1.0 while the surrounding ambient temperature is set to 0. A convective outflow boundary condition is used at the exit.

The Stokes number of a particle signifies how quickly a particle responds to any perturbations in the flow. A Stokes number much less than unity implies that the particle responds almost instantaneously to the changes in the fluid surrounding it. In the present calculation the range of momentum Stokes number is 1.06 to 4.8.

240,000 particles are injected at the inlet over 12 injections. During the injection, the particles are randomly distributed over the cross-section of the inlet tube. The initial velocities and temperature of the injected particles are set to the fluid velocity and temperature. Particles travel through the length of the inlet tube before leaving with the free jet and impacting the coupon surface. Most of the particles in the core flow hit the coupon surface while some are able to go around the coupon. For each particle-wall collision, coefficient of restitution is calculated based on impact parameters of the collisions as discussed in our previous work[2]. A probability of sticking$\left(\mathrm{P}_e\right)$ is calculated based on this coefficient of restitution using eq. 6. The sticking probability$\left(P_{visc}\right)$ is also calculated based on the temperature of the particle from eq. 9 and hence the final probability$\left(P\right)$ from eq. 11. Depending upon the particle velocity and temperature, some of the impacting particles deposit while the remaining particles rebound and impact again or go around the coupon.

5.3.8 Solver Controls

All the calculations are carried out using our in-house finite volume code, GenIDLEST[48]. The carrier phase (fluid) is solved using LES and the dispersed phase (particles) are computed using Lagrangian particle tracking algorithm[43]. The governing equations for the carrier phase are discretized using second order central difference scheme on a non-staggered grid topology. The governing equations for particle motion are integrated using a third order Adams-Bashforth method in the Lagrangian frame of reference to obtain the velocity, location, and temperature. The convergence criterion for the momentum, pressure and the energy are 1×10^{-6}, and 1×10^{-6}, respectively at each time step. The time step is set at 1.6×10^{-4}. The flow is first allowed to develop for more than 20 non-dimensional time units before the particles are injected. The particles are tracked and allowed to run until all the particles cross the target plate. All the particle impacts on the coupon are recorded with impact velocities and angles, along with recording how many of the impacting particles deposit.

5.4 Results

Transport of 20-40 microns sized particles is simulated for jet impingement on a coupon at 45° and 90°, at three different jet temperatures using Large Eddy Simulations (LES). First the flow field and heat transfer results are discussed followed by the particle deposition.

5.4.1 Fluid Flow and Temperature Field

Again 90° case will be used to discuss flow field and temperature field. Figure 5.11(a) shows the instantaneous streamwise velocity contours and flow streamlines. The flow leaves the inlet tube as a free jet and hits the coupon normally and then accelerates around the coupon and eventually exits through the outflow. Recirculation zones are observed just at the corners where the flow accelerates around the coupon boundary. Large Eddy Simulations are able to capture one of the prominent features of the flow which is the free shear mixing layer between the jet from the pipe and surrounding stationary fluid. Figure 5.11(b) shows instantaneous temperature contours in the vicinity of the coupon and inlet pipe exit. The fluid in the mixing layer is cooled due to surrounding fluid entrainment, but the fluid in core of the flow that hits the coupon remains at or around jet temperature with very thin thermal boundary layer at coupon surface.

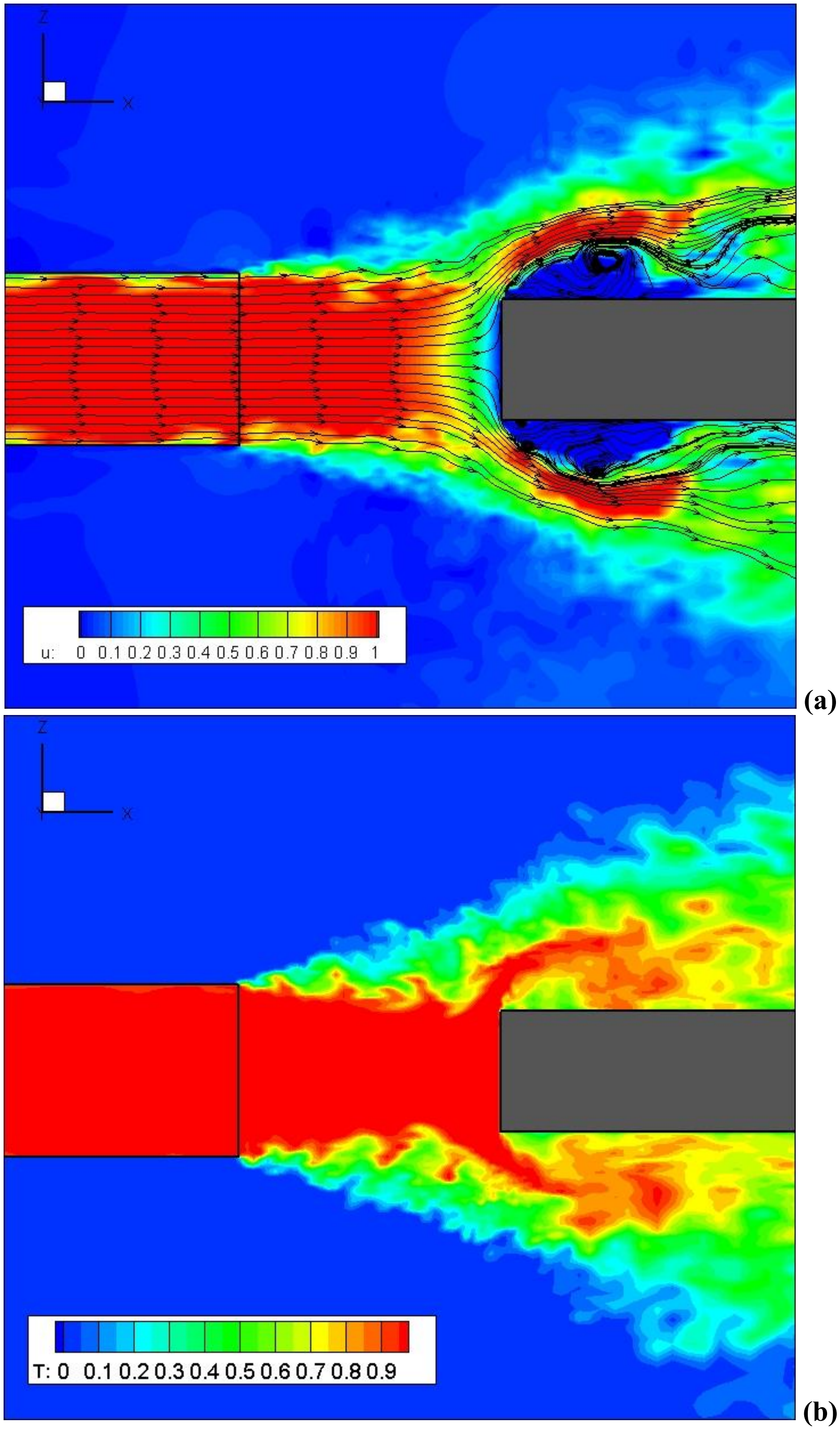

Figure 5.11 (a) Instantaneous streamwise velocity and streamlines, (b) Instantaneous temperature

5.4.2 Particle Transport and Deposition

Figure 5.12 shows a snapshot of particles impacting the coupon surface and going around the coupon. For the studied particle size range, due to larger Stokes numbers (St > 1.0), the particles do not decelerate significantly with the flow before impacting the coupon. Most of the particle impact the coupon near jet velocity and temperature. As expected, the particles impact nearly at right angles in the vicinity of the stagnation point and the impact angles decrease slightly away from center of the coupon. For every particle collision with the coupon surface, the particle temperature and particle velocity determine if the particle sticks or rebounds. Impact efficiency $\left(\eta_{imp}\right)$ is defined as the ratio of the number of particles impacting the coupon surface $\left(n_{imp}\right)$ to total number of particles injected $\left(n_{inp}\right)$ in the project area of the coupon. Sticking efficiency $\left(\eta_{stick}\right)$ is defined as the ratio of the number of particles depositing $\left(n_{dep}\right)$ to the total number of particles impacting $\left(n_{imp}\right)$ the coupon surface. Capture efficiency $\left(\eta_{cap}\right)$ is defined as the ratio of the number of particles deposited to the number of particles injected $\left(n_{inp}\right)$ in the projected area of the coupon.

$$\eta_{imp} = \frac{n_{imp}}{n_{inp}}, \ \eta_{stick} = \frac{n_{dep}}{n_{imp}} \ \ and \ \ \eta_{cap} = \frac{n_{dep}}{n_{inp}} \tag{18}$$

$$\Rightarrow \eta_{cap} = \eta_{imp} \times \eta_{stick} \tag{19}$$

Rebound ratio is defined as the number of particles rebounding from the coupon surface to the total number of particles impacting the coupon surface. The sum of sticking efficiency and rebound efficiency should be unity. This is easily verified in the numerical calculations while the experiments do record the sum to be unity due to possibility of the particles rebounding out of plane of examination.

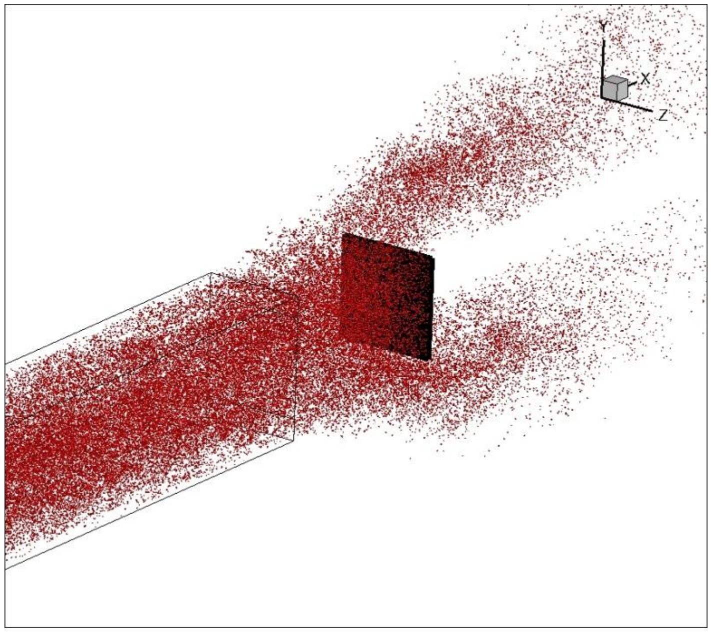

(a)

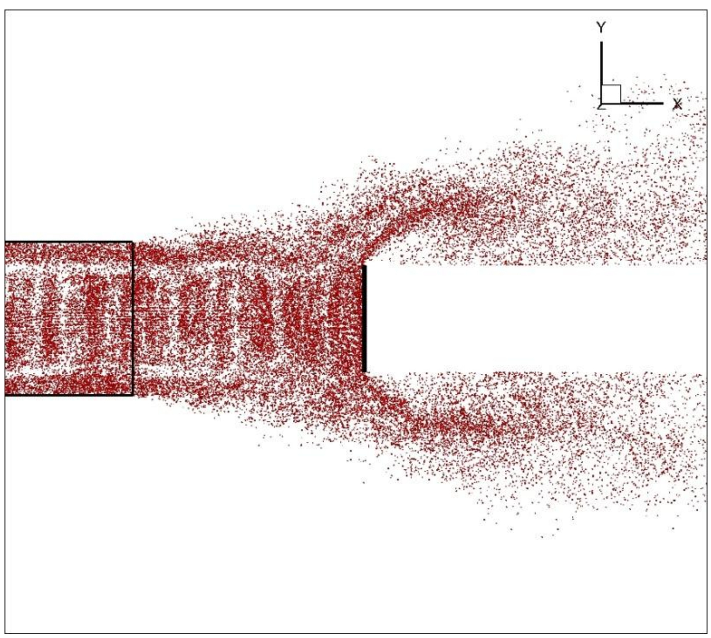

(b)

Figure 5.12 Snapshot of particle transport (a) Isometric view (b) Side view

Approximately, 54% of the 240,000 injected particles, impact the coupon for all the three jet temperature while the remaining particles are able to turn with the flow and go around the coupon. Table 5.2 shows the number of particles impacting (n_{imp}) the coupon and depositing (n_{dep}) for the three jet temperatures considered, along with sticking efficiency, capture efficiency and rebound ratio, for the coupon at 90^0. At jet temperature of 950 ^oC, 5% of the particles impacting the coupon deposit. At this temperature the effect of particle viscosity is significantly low and all the deposition is essentially due to energy losses due to impact. For jet temperature of 1000 ^oC and 1050 ^oC, particle begins to soften as the viscosity decreases and deposition increases. At these temperatures impact losses and particle viscosity, both the effects together determine the sticking probability.

Table 5.2 Sticking efficiency and rebound ratio at different jet temperatures, 90^0 case (CFD)

Jet Temperature	n_{imp}	n_{dep}	**Impact Efficiency** (η_{imp})	**Sticking Efficiency** (η_{stick})	**Capture Efficiency** (η_{cap})	**Rebound Ratio**
950 ^oC	126942	6473	0.881	0.050	0.045	0.950
1000 ^oC	129457	22560	0.899	0.174	0.157	0.826
1050 ^oC	129070	36721	0.896	0.284	0.255	0.716

Table 5.3 Sticking efficiency and rebound ratio at different jet temperatures, 45^0 case (CFD)

Jet Temperature	n_{imp}	n_{dep}	**Impact Efficiency** (η_{imp})	**Sticking Efficiency** (η_{stick})	**Capture Efficiency** (η_{cap})	**Rebound Ratio**
950 ^oC	120117	2464	0.834	0.021	0.017	0.979
1000 ^oC	120967	19307	0.840	0.159	0.134	0.841
1050 ^oC	120898	36970	0.839	0.306	0.256	0.694

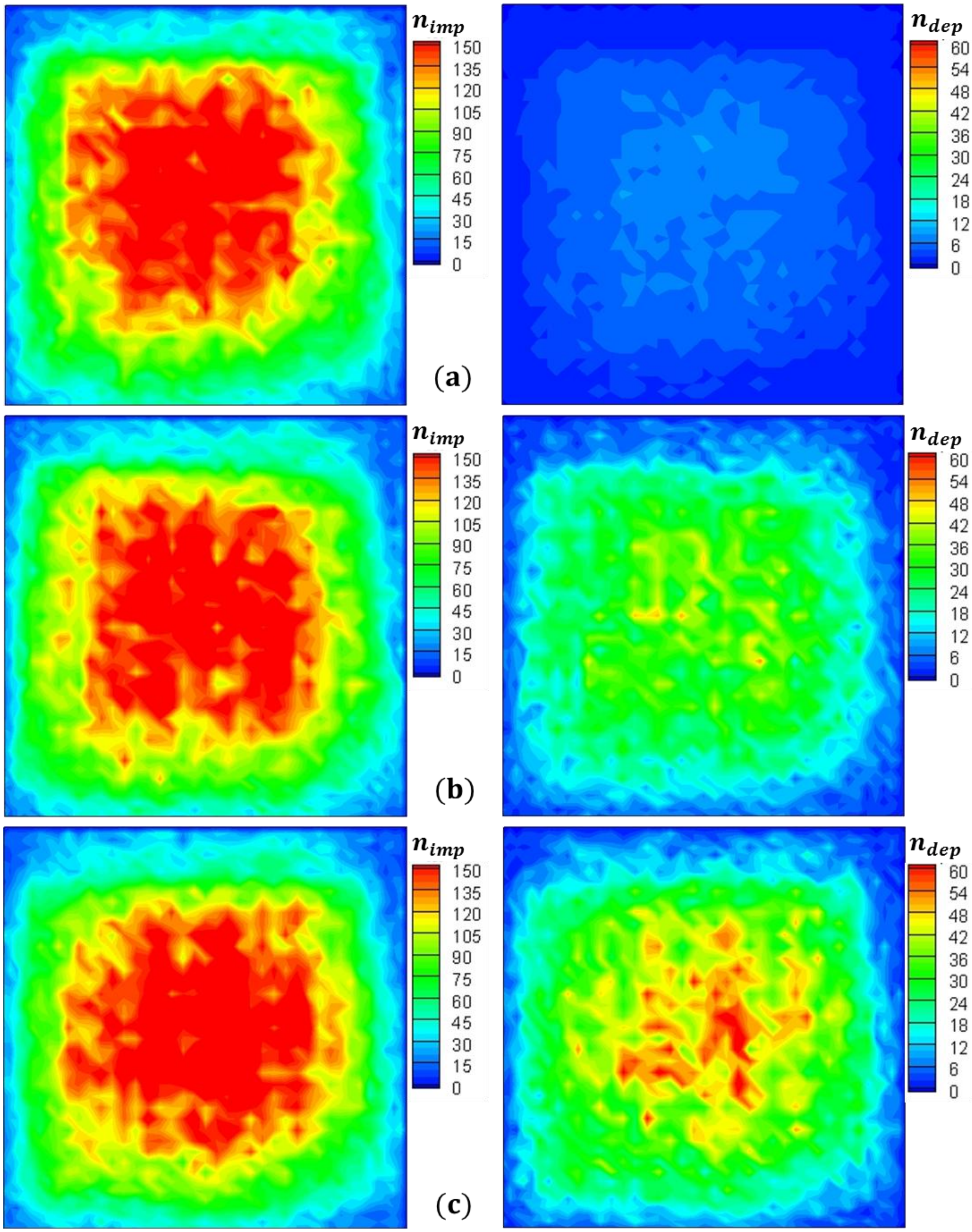

Figure 5.13 90^0 case, contours of particle impingement (n_{imp}), on the left and particle deposition (n_{dep}) on the right; Jet temperature (a) 950 °C, (b) 1000 °C and (c) 1050 °C

Approximately, 17 % of the particles impacting the coupon deposit at 1000 ^{o}C and 28% deposit at 1050 ^{o}C. Figure 5.13 shows the contours of particles impingement and deposition on the coupon for the three jet temperatures, for 90^0 case. For all the three jet temperatures, highest particle impingement is observed in and around the center of the coupon and decreases with distance away from center. Near the edges the particles are able to turn with the flow and hence, leading to lower particle impingement in those regions. As expected, the number of particle depositions also follow the same trend as particle impingements.

Table 5.3 shows the number of particles impacting (n_{imp}) the coupon and depositing (n_{dep}) for the three jet temperatures considered, along with sticking efficiency, capture efficiency and rebound ratio, for the coupon at 45^0. The overall impingement and sticking variation with temperature is very similar to as observed in the 90^0 case. As expected, lower impact efficiency is observed in 45^0 case compared to the 90^0 case due the particles being able to negotiate the smoother 45^0 turn compared to the sudden 90^0 turn in the normal impingement case. Figure 5.14 shows the contours of particles impingement and deposition on the coupon for the three jet temperatures, for 45^0 case. It can be noted that, the coupon area is no longer square but rectangular keeping the projected area same in the 90^0 case. Again, the particle impingement and deposition pattern are similar to the 90^0 case, but impingement/deposition area is stretched in the streamwise direction due to the coupon being aligned at 45^0 with the flow direction. It can also be noticed that for all the three jet temperatures, higher particle impingement is observed near the leading edge, for the farther the particles are from the leading edge, more the time to turn with flow and avoid the coupon surface.

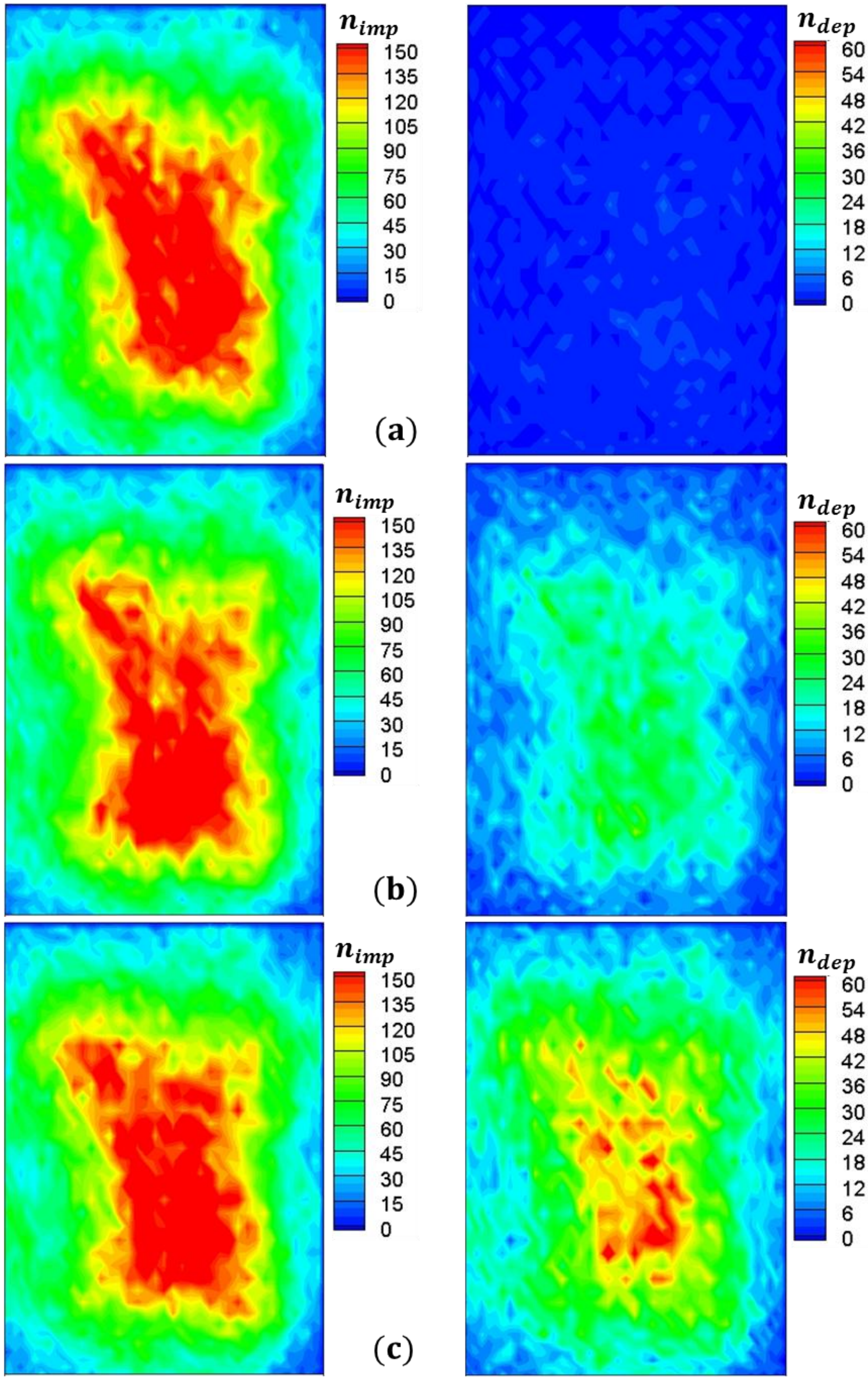

Figure 5.14 45^0 case, contours of particle impingement (n_{imp}), on the left and particle deposition (n_{dep}) on the right; Jet temperature (a) 950 ^oC, (b) 1000 ^oC and (c) 1050 ^oC

Figure 5.15 compares the numerically calculated rebound ratio for different jet temperatures with the experimental data[3] for the coupon at different angles from 30^{o}-80^{o}. Experiments show that from 950 ^{o}C to 1000 ^{o}C, for all coupon angles the rebound ratio decreases with increasing jet temperature. From 1000 ^{o}C to 1050 ^{o}C, while some coupon angles show increase in rebound ratio, but the mean rebound ratio over all the angles decreases. The numerical predictions show very good agreement with the experiments, especially for coupon angles of 80^{o}, 70^{o} and 40^{o}. Considering the challenges in measuring deposition in the experiments and assumptions in the current deposition model, the deposition predictions from LES show a very good agreement with the mean rebound ratio over all the coupon angles. However, the numerical predictions and mean experimental curves seem to diverge around 1050 ^{o}C, the efficacy of the model above these temperatures remains to be tested. The maximum attainable test section temperature of VT aerothermal rig is around 1050 ^{o}C and is restricted by the limits of uncooled equilibration tube.

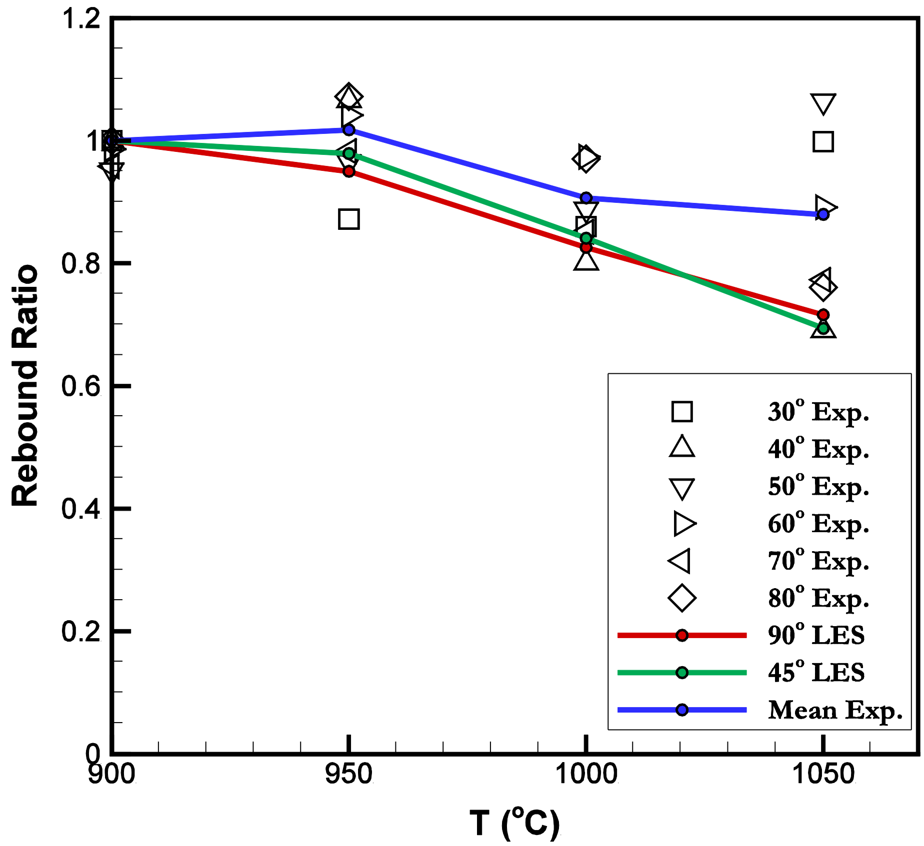

Figure 5.15 Rebound ratio comparison of LES and experiments at different jet temperatures (T_{jet})

5.5 Summary and Conclusions

An improved physical model based on the critical viscosity approach[1] and energy losses during particle-wall collisions, is developed to predict the sand deposition at high temperatures in gas turbine components. For validation purposes, the deposition of sand particles is calculated for particle laden jet impingement on a coupon and compared with experiments conducted at Virginia Tech[3]. Large Eddy Simulations are used to calculate the flow filed and heat transfer and particle dynamics is modeled using a Lagrangian approach. The proposed model is novel in the sense that it predicts the sticking probability based on the impact velocity along with the particle temperature.

For every particle impacting the coupon surface, the particle velocity and temperature determine if the particle sticks or rebounds based on the current deposition model. Apart from inevitable uncertainties in the model parameters due to idealization, there is no calibration involved. Results quantify the sticking, capture efficiency and rebound ratio for 20-40 microns sand particles. The results show a very good agreement with the experiments for the range of jet temperatures investigated. The results show decrease in rebound ratio as the temperature increases which can be attributed to change in the physical properties of the particle with temperature and collision losses. As the temperature increases the particles start to get soft and melt, leading to higher deposition. Even at temperatures much lower than softening temperature, the model predicts significant deposition, which can be attributed to energy losses during collisions. Considering the challenges in measuring particle deposition in the experiments and assumptions of the current deposition model, the model predictions are in very good agreement with the experiments. This model will be extended to study sand deposition in the internal cooling passages of gas turbine blades. This model can also be used to investigate sand deposition in the other hot gas path turbine components.

5.6 Acknowledgments

The calculations were performed on Virginia Tech's computing facility Blueridge and Hokiespeed. The authors would like to thank the Commonwealth of Virginia and Rolls-Royce for their support especially Kwen Hsu, Brett Barker, N. Wagers and Paul Davis for thoughtful discussions, analysis and advice. The authors are also thankful to Dr. Wing Ng, Dr. Srinath Ekkad, Jacob Delimont and Matt Murdock at Virginia Tech for providing experimental data along with discussions and feedback on model development.

References

[1] Sreedharan, S. S., and Tafti, D. K., 2011, "Composition dependent model for the prediction of syngas ash deposition in turbine gas hotpath," Int J Heat Fluid Fl, 32(1), pp. 201-211.

[2] Singh, S., and Tafti, D., "Predicting the Coefficient of Restitution for Particle Wall Collisions in Gas Turbine Components," Proc. ASME Turbo Expo 2013: Turbine Technical Conference and Exposition, American Society of Mechanical Engineers, pp. V06BT37A041-V006BT037A041.

[3] Delimont, J., Murdock, M., Ng, W., and Ekkad, S., 2014, "Effect of Near Melting Temperatures on Microparticle Sand Rebound Characteristics at Constant Impact Velocity," Proceedings of ASME Turbo Expo 2014: Turbine Technical Conference and Exposition, GT2014, June 16 – 20, 2014, Düsseldorf, Germany.

[4] Hamed, A., Tabakoff, W., and Wenglarz, R., 2006, "Erosion and deposition in turbomachinery," J Propul Power, 22(2), pp. 350-360.

[5] Kim, J., Dunn, M. G., Baran, A. J., Wade, D. P., and Tremba, E. L., 1993, "Deposition of Volcanic Materials in the Hot Sections of 2 Gas-Turbine Engines," J Eng Gas Turb Power, 115(3), pp. 641-651.

[6] Tabakoff, W., 1987, "Compressor Erosion and Performance Deterioration," J Fluid Eng-T Asme, 109(3), pp. 297-306.

[7] Alge T. L., M. J. T., 1994, "Modern Transport Engine Experience with Environmental Ingestion Effect," Propulsion and Energetic Panel (PEP), Symposium, Rotterdam, Netherlands. AGARD.

[8] Edwards, V. R., Rouse, P.L., 1994, "U.S. Army Rotorcraft Turboshaft Engines Sand & Dust Erosion Considerations," AGARD, Erosion, Corrosion and Foreign Object Damage Effects in Gas Turbines, Quebec, Canada.

[9] Wenglarz, R. A., Wright, I. G., 2002, "Alternate Fuels for Land-Based Turbines," Proceedings of the Workshop on Materials and Practices to Improve Resistance to Fuel Derived Environmental Damage in Land- and Sea-Based Turbines, October 22–24, Colorado School of Mines, Golden, Co.

[10] Toriz, F. C., Thakker, A. B., and Gupta, S. K., 1988, "Thermal Barrier Coatings for Jet Engines," ASME Paper No. 88-GT-279.

[11] Smialek, J. L., 1992, "The Chemistry of Saudi Arabian Sand: A Deposition Problem on Helicopter Turbine Airfoils," Advances in Synthesis and Processes , SAMPE, 3 , M92-M101.

[12] Wenglarz, R. A., and Fox, R. G., 1990, "Chemical Aspects of Deposition Corrosion from Coal Water Fuels under Gas-Turbine Conditions," J Eng Gas Turb Power, 112(1), pp. 1-8.

[13] Bons, J. P., Crosby, J., Wammack, J. E., Bentley, B. I., and Fletcher, T. H., 2005, "High pressure turbine deposition in land based gas turbines from various synfuels," Proceedings of the ASME Turbo Expo 2005, Vol 1, pp. 411-419.

[14] Jensen, J. W., Squire, S. W., Bons, J. P., and Fletcher, T. H., 2005, "Simulated land-based turbine deposits generated in an accelerated deposition facility," J Turbomach, 127(3), pp. 462-470.

[15] Wammack, J. E., Crosby, J., Fletcher, D., Bons, J. P., and Fletcher, T. H., 2006, "Evolution of surface deposits on a high pressure turbine blade, part I: Physical characteristics," Proceedings of the ASME Turbo Expo 2006, Vol 3, Pts A and B, pp. 1055-1063.

[16] Crosby, J. M., 2007, "Particle Size, Gas Temperature, and Impingement Cooling Effects on High Pressure Turbine Deposition in Land based Gas Turbines from Various Synfuels," Master's thesis. Brigham Young University.

[17] Anderson, R. J., Romanowski, C. J., and France, J. E., 1984, "The Adherence of Ash Particles From the Combustion of Micronized Coal," DOE/METC-85/2007.

[18] Ahluwalia, R. K., Wenglarz, R. A., and Im, K. H., 1989, "Flyash Adhesion in Simulated Coal-Fired Gas Turbine Environment," Journal of Engineering for Gas Turbines and Power, 111(4), pp. 672-678.

[19] Wenglarz, R. A., and Fox, R. G., 1990, "Physical Aspects of Deposition from Coal Water Fuels under Gas-Turbine Conditions," J Eng Gas Turb Power, 112(1), pp. 9-14.

[20] Dunn, M. G., Baran, A. J., and Miatech, J., 1996, "Operation of gas turbine engines in volcanic ash clouds," J Eng Gas Turb Power, 118(4), pp. 724-731.

[21] Walsh, W. S., Thole, K. A., Joe, C., 2006, "Effects of Sand Ingestion on the Blockage of Film-Cooling Holes," ASME Paper No. GT2006-90067, Proceedings of ASME Turbo Expo, Barcelona, Spain.

[22] Land, C. C., Joe, C., and Thole, K. A., 2010, "Considerations of a Double-Wall Cooling Design to Reduce Sand Blockage," J Turbomach, 132(3).

[23] Walsh, P. M., Sayre, A. N., Loehden, D. O., Monroe, L. S., Beer, J. M., and Sarofim, A. F., 1990, "Deposition of Bituminous Coal Ash on an Isolated Heat-Exchanger Tube - Effects of Coal Properties on Deposit Growth," Prog Energ Combust, 16(4), pp. 327-346.

[24] Huang, L. Y., Norman, J. S., Pourkashanian, M., and Williams, A., 1996, "Prediction of ash deposition on superheater tubes from pulverized coal combustion," Fuel, 75(3), pp. 271-279.

[25] Zhou, H. S., Jensen, P. A., and Frandsen, F. J., 2007, "Dynamic mechanistic model of superheater deposit growth and shedding in a biomass fired grate boiler," Fuel, 86(10-11), pp. 1519-1533.

[26] Hansen, L. A., Frandsen, F. J., Dam-Johansen, K., and Sorensen, H. S., 1999, "Quantification of fusion in ashes from solid fuel combustion," Thermochim Acta, 326(1-2), pp. 105-117.

[27] Kær, S. K., 2001, "Numerical Investigation of Ash Deposition in Straw Fired Boilers," Ph.D. thesis. Institute of Energy Technology, Denmark.

[28] El-Batsh, H., Haselbacher, H., 2002, "Numerical Investigation of the Effect of Ash Particle Deposition on the Flow Field through Turbine Cascades," IGTI, Amsterdam, Netherlands, GT-2002-30600.

[29] Ai, W. G., and Fletcher, T. H., 2012, "Computational Analysis of Conjugate Heat Transfer and Particulate Deposition on a High Pressure Turbine Vane," J Turbomach, 134(4).

[30] Crosby, J. M., Lewis, S., Bons, J. P., Ai, W. G., and Fletcher, T. H., 2007, "Effects of particle size, gas temperature, and metal temperature on high pressure turbine deposition in land based gas

turbines from various synfuels," Proceedings of the Asme Turbo Expo 2007, Vol 4, Pts a and B, pp. 1365-1376.

[31] Sreedharan, S. S., and Tafti, D. K., 2013, "Effect of Blowing Ratio on Early Stage Deposition of Syngas Ash on a Film-Cooled Vane Leading Edge Using Large Eddy Simulations," J Turbomach, 135(6).

[32] Senior, C. L., and Srinivasachar, S., 1995, "Viscosity of Ash Particles in Combustion Systems for Prediction of Particle Sticking," Energ Fuel, 9(2), pp. 277-283.

[33] Yin, C., Luo, Z., Ni, M., and Cen, K., 1998, "Predicting coal ash fusion temperature with a back-propagation neural network model," Fuel, 77(15), pp. 1777-1782.

[34] Hylton, L., Nirmalan, V., Sultanian, B., Kaufman, R., 1988, "The Effects of Leading Edge and Downstream Film Cooling on Turbine Vane Heat Transfer," NASA Contractor Report - 182133.

[35] Nealy, D. A., Mihelc, M. S., Hylton, L. D., and Gladden, H. J., 1984, "Measurements of Heat-Transfer Distribution over the Surfaces of Highly Loaded Turbine Nozzle Guide Vanes," J Eng Gas Turb Power, 106(1), pp. 149-158.

[36] Reagle, C., Delimont, J., Ng, W., Ekkad, S., and Rajendran, V., 2013, "Measuring the coefficient of restitution of high speed microparticle impacts using a PTV and CFD hybrid technique," Measurement Science and Technology, 24(10), p. 105303.

[37] Reagle, C., Delimont, J., Ng, W., and Ekkad, S., 2014, "Study of Microparticle Rebound Characteristics Under High Temperature Conditions," Journal of Engineering for Gas Turbines and Power, 136(1), p. 011501.

[38] Reagle C., D. J., Ng W., Ekkad S., Rajendran V., 2013, "Measuring the coefficient of restitution of
high speed microparticle impacts using a
PTV and CFD hybrid technique," Measurement Science and Technology, 24(10).

[39] Reagle CJ, D. J., Ng WF, Ekkad SV, 2014, "Study of Microparticle Rebound Characteristics Under High Temperature Conditions," Journal of Engineering for Gas Turbines and Power, 136(1).

[40] Germano, M., Piomelli, U., Moin, P., and Cabot, W. H., 1991, "A Dynamic Subgrid-Scale Eddy Viscosity Model," Phys Fluids a-Fluid, 3(7), pp. 1760-1765.

[41] Moin, P., Squires, K., Cabot, W., and Lee, S., 1991, "A Dynamic Subgrid-Scale Model for Compressible Turbulence and Scalar Transport," Phys Fluids a-Fluid, 3(11), pp. 2746-2757.

[42] Patil, S., and Tafti, D., 2012, "Wall modeled large eddy simulations of complex high Reynolds number flows with synthetic inlet turbulence," Int J Heat Fluid Fl, 33(1), pp. 9-21.

[43] Shah, A., 2005, "Development and Application of Dispersed Two Phase Capability in a General Multi-Block Navier Stokes Solver," Thesis, Virginia Polytechnic Institute and State University, Blacksburg, VA.

[44] Shah, A., and Tafti, D. K., 2007, "Transport of particulates in an internal cooling ribbed duct," J Turbomach, 129(4), pp. 816-825.

[45] Tabakoff, W., 1991, "Measurements of Particles Rebound Characteristics on Materials Used in Gas-Turbines," J Propul Power, 7(5), pp. 805-813.

[46] Wang, Q., and Squires, K. D., 1996, "Large eddy simulation of particle deposition in a vertical turbulent channel flow," Int J Multiphas Flow, 22(4), pp. 667-683.

[47] Armenio, V., Piomelli, U., and Fiorotto, V., 1999, "Effect of the subgrid scales on particle motion," Phys Fluids, 11(10), pp. 3030-3042.

[48] Tafti, D. K., 2001, "GenIDLEST – A scalable parallel computational tool for simulatingcomplex turbulent flows," Proc. ASME Fluids Engineering Division, 256.

Chapter 6

Sand Transport and Deposition in a Two Pass Internal Cooling Duct with Rib Turbulators

In Chapter 3, the sand transport of 0.5-25 microns sand particles was investigated in a two pass internal cooling duct with rib turbulators. The calculated impingement patterns showed good agreement when compared qualitatively with the experimental visualization results. The CFD and experiments simulated the sand transport in the two pass geometry at ambient conditions and the effect of temperature on particles was not considered. For particle-wall interaction it was assumed that the particles do not incur any energy losses in the collision process and all the collisions are perfectly elastic. This exercise with significant simplifications, was worthwhile in understanding the particle transport in the internal cooling passages of gas turbine blades. However, the simulations differ from the real engine conditions in two essential aspects, where: a) the particle wall collisions are anything but perfectly elastic; b) extremely high temperatures in the turbine blades can cause the particles to soften or even melt leading to significant deposition. Both these issues were addressed in detail in the previous chapters, Chapter 4 and Chapter 5, respectively. Chapter 4 developed and validated a model to predict the coefficient of restitution for particle-wall collisions by accounting for deformation and adhesion losses during an impact. Chapter 5 proposed and validated an improved physical model to predict the probability of sticking of a particle, by accounting for energy losses and change in the physical properties of the particle with temperature. In this chapter, the two pass geometry is revisited with the developed particle-wall interaction models in the previous two chapters. The flow field and heat transfer is identical to Chapter 2, by keeping the Reynolds number and Prandtl number same. Deposition of sand particles in the size range 5-25 microns, is investigated in the two pass geometry for three different wall temperatures of 950 ^{o}C, 1000 ^{o}C and 1050 ^{o}C. Particle impingement and deposition patterns are compared for the three temperatures, along with overall deposition in the two pass geometry.

6.1 Methodology

All the details about computational setup, grid and numerical method are identical to Chapter 2 for flow field and heat transfer calculation. Particle transport modelling is also identical to Chapter 3 and Chapter 5, except the particle size and particle-wall interaction which will be discussed in detail in this section.

6.1.1 Particle-wall interaction

To account for energy losses during a particle-wall interaction, the coefficient of restitution model developed in Chapter 4 is used and the sticking probability for deposition is calculated through the deposition model discussed in Chapter 5. For every particle impacting a surface, the coefficient of restitution is calculated from impact parameters as discussed in Chapter 4. Then a probability of sticking is calculated based on the coefficient of restitution and the temperature of the particle, as discussed in Chapter 5. A uniform random number generator is used to generate a number between 0 and 1. If this random number is less than the sticking probability calculated, the particle is assumed to deposit. If the particle does not deposit, it rebounds with the velocity calculated from the coefficient of restitution.

Randomly distributed particles are injected at the inlet with 10,000 particles per injection for 24 injections. Initially upon injection, the particle velocities and temperature are set to be the same as the surrounding fluid. Particle size range is 5-25 microns with mean particle diameter as 6 microns and standard deviation as 3 microns. The Stokes number corresponding to this size range is 0.385 to 6.059. The particles are tracked and the calculation is run until all the particles either deposit or leave the computational domain. Wall collision statistics are recorded during the run.

The calculations were run on 153 Intel Xeon E5-2670 (Sandy Bridge) processors with Infiniband QDR interconnect. For carrier phase only, computing one time dimensionless unit takes 6-8 hours and with particles the same takes 10-12. The calculations were run for approximately 50 nondimensional time units, which took around 500 wall clock hours for each of the three cases.

6.2 Results

Since the flow field and temperature field is identical to that discussed in Chapter 2, only the particle transport and deposition will be discussed in this chapter. Detailed particle impingement and deposition is discussed separately for the ribbed wall, side walls, endwall and rib faces.

6.2.1 Ribbed wall

In the internal cooling passages of a gas turbine blade, ribbed walls by far are the most important regions for heat transfer augmentation. Any particle deposition and damage on the ribbed wall may cause loss in the cooling performance of the internal cooling duct. It is observed that the particle impingement and deposition is similar on both the ribbed walls, so only one wall is shown for analysis. In figure 6.1 (a), 6.2 (a) and 6.3 (a), particle impingement patterns (n_{imp} is the number of particle impacts) are presented for the three wall temperatures of 950 ^{o}C, 1000 ^{o}C and 1050 ^{o}C, respectively. For all three wall temperatures, four regions on the ribbed wall can be identified with distinct particle impingement patterns: bend region, the region upstream of the bend, the region downstream of the bend, and the inlet/outlet region. Figure 6.1 (a), shows that the bend region experiences the highest particle impingement especially in the downstream end wall corner of the bend (pitch # 18). This is the region where the turning flow impinges on the end wall and the smooth outside side wall of the second pass. This particle impingement can be attributed to large particles bouncing off the end and side walls and impacting the ribbed surface, and smaller particles which are transported to the surface by the turbulent eddies which develop in the separated shear layer at the inner partition . This is corroborated by Figures 6.7 -6.8, which show the particle size distribution, particle velocity, and angle of impingement. Large particles impact the region of the bend immediately downstream of the first pass at medium velocities at relatively high angles, followed by a region mostly dominated by smaller particles impinging with mid-to-high velocities and shallower angles. Correlating the number of impacts with the particle size, it can be established that the ribbed wall in the bend region is prone to large particle medium impacts in the initial part of the bend (pitch # 16) followed by heavy small particle impingement in the downstream part of the bend (pitch # 18). Though there is a small recirculation in the corner, direct impingement of flow is essentially responsible for higher number of particle impacts. Significant particle impingement is also observed in the region where the flow enters the bend just downstream of the first pass (pitch # 16). This can be attributed to particles bouncing off the outer smooth wall in the first pass while turning into the bend region and lower the Stokes number particles carried to the ribbed wall. The upstream corner of the bend does not experience much particle impingement, implying that the particles are able to turn with the flow and evade the recirculation region in the upstream corner.

Comparing particle impingement in the four pitches upstream of the bend with the same downstream of the bend, it is found that particle impingement is more widespread in between two ribs, in the second pass, while in the first pass particles show a lower tendency to impact the region immediately behind the rib. The higher impingement immediately behind the rib in the second pass (pitch 19 &20) is due to higher turbulence in this region, accompanied by stronger secondary flows due to the turning flow, which result in more particles being entrained into the turbulent eddies. Also, higher particle impingement is observed near the sidewalls in pitch 15 in the first pass because of the turning flow. From Figure 6.7, it can be established that larger particles tend to impact the ribbed wall in regions near the side walls and immediately upstream of the ribs indicating that the impacting particles bounce off these surfaces before impaction on the ribbed wall. On the other hand, the smaller particles seem to be more uniformly distributed in the pitch. While there is no clear correlation between particle size with velocity and angle of impact (see Figure 6.8), the velocity and angle of impingement are noticeable higher in the second pass.

When the particle impingement is compared for different wall temperatures of 950 ^{o}C, 1000 ^{o}C and 1050 ^{o}C, though the overall impingement pattern remains the same, the amount of impingement decreases with increasing temperature. The impingement at 1050 ^{o}C is significantly lower than that at 950 ^{o}C. This is due to the loss of near wall particles to deposition. Particle impingement decreases downstream of the inlet for 1000 ^{o}C and 1050 ^{o}C cases compared to 950 ^{o}C. In the bend region the particle impingement is similar for all the three temperatures, since in this region, the direct impingement of the particles in the core of the flow (relatively immune to deposition) is essentially responsible for higher impingement and deposition. This is also confirmed by the impacts in this region being dominated by larger diameter particles as discussed later. Impingement immediately downstream of the bend is again high for all three wall temperatures plausibly due to remixing of all the particles after impacting the endwall and the side wall in the bend region before entering the second pass. However, the impingement for the 1050 ^{o}C case is much lower due to significant loss of particles to deposition in the first pass and bend region.

In figure 6.1 (b), 6.2 (b) and 6.3 (b), particle deposition patterns (n_{dep} is the number of particles deposited) are presented for all the three wall temperatures of 950 ^{o}C, 1000 ^{o}C and 1050 ^{o}C, respectively. As expected the particle deposition also follows the same trend as the particle impingement but the extent of deposition depends on the wall temperature. For a relatively lower temperature of 950 ^{o}C, the impacting particles are not soft enough and only a very small number of the impacting particles stick showing slight deposition on all the surfaces. Deposition increases significantly as the temperature is increased to 1000 ^{o}C, roughly 12% of the impacting particles, deposit. For 1050 ^{o}C, approximately 23% of the particles deposit on impact, also leading to a decrease in particle impingement on the ribbed surface in the downstream regions.

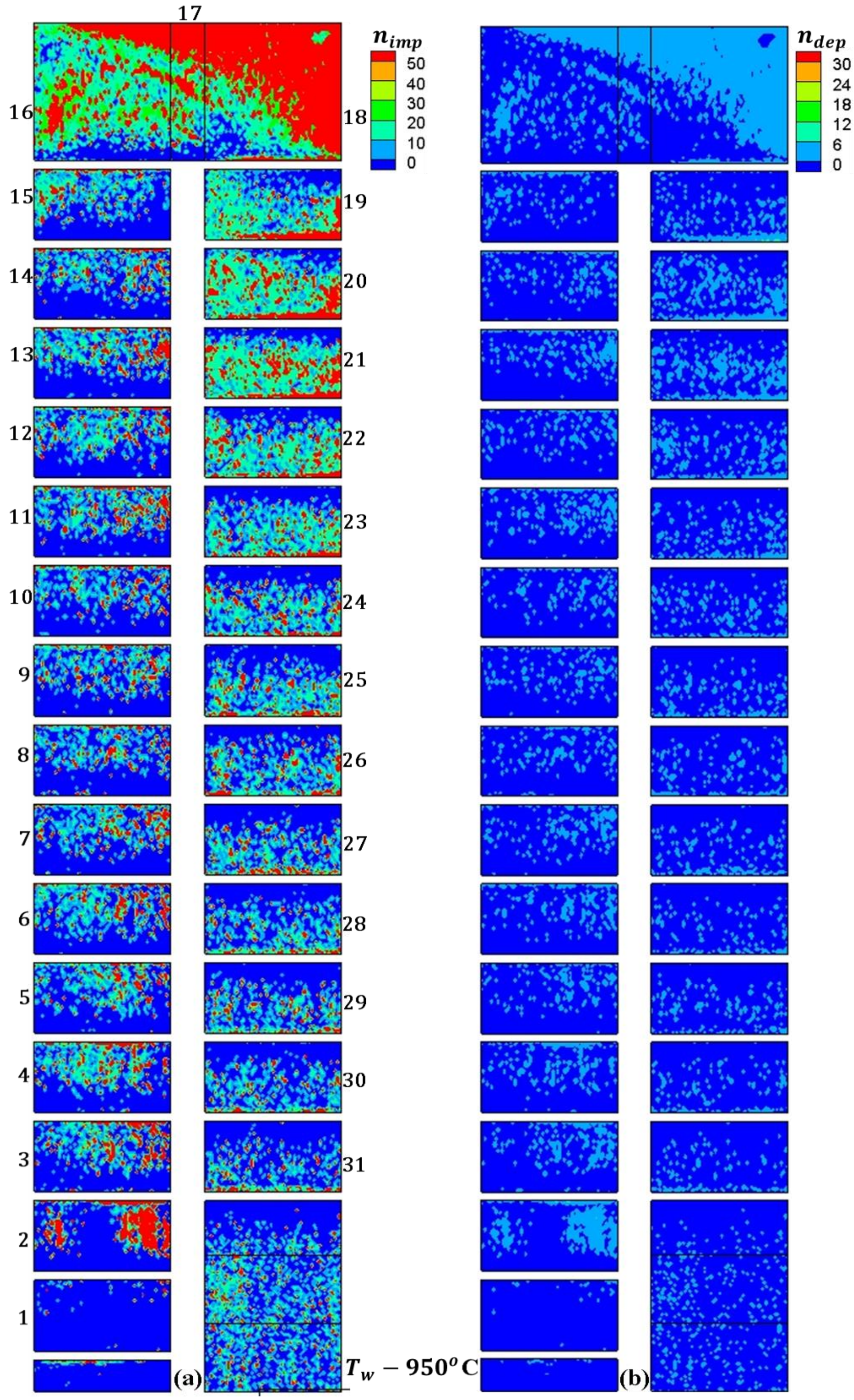

Figure 6.1 Contours of particle impingement (a) and particle deposition (b) on the ribbed wall for wall temperature of 950^{o}C.

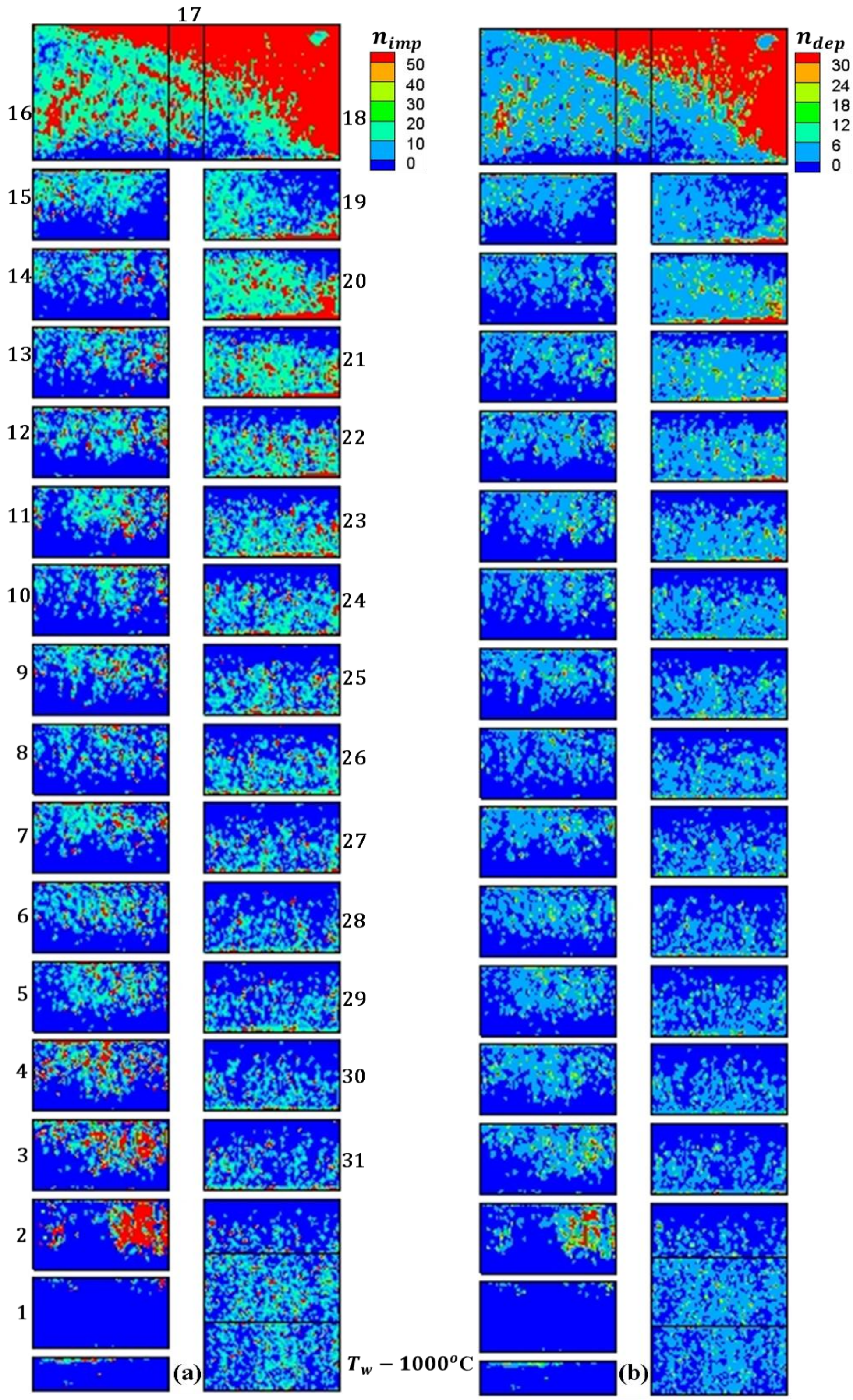

Figure 6.2 Contours of particle impingement (a) and particle deposition (b) on the ribbed wall for wall temperature of 1000^{o}C.

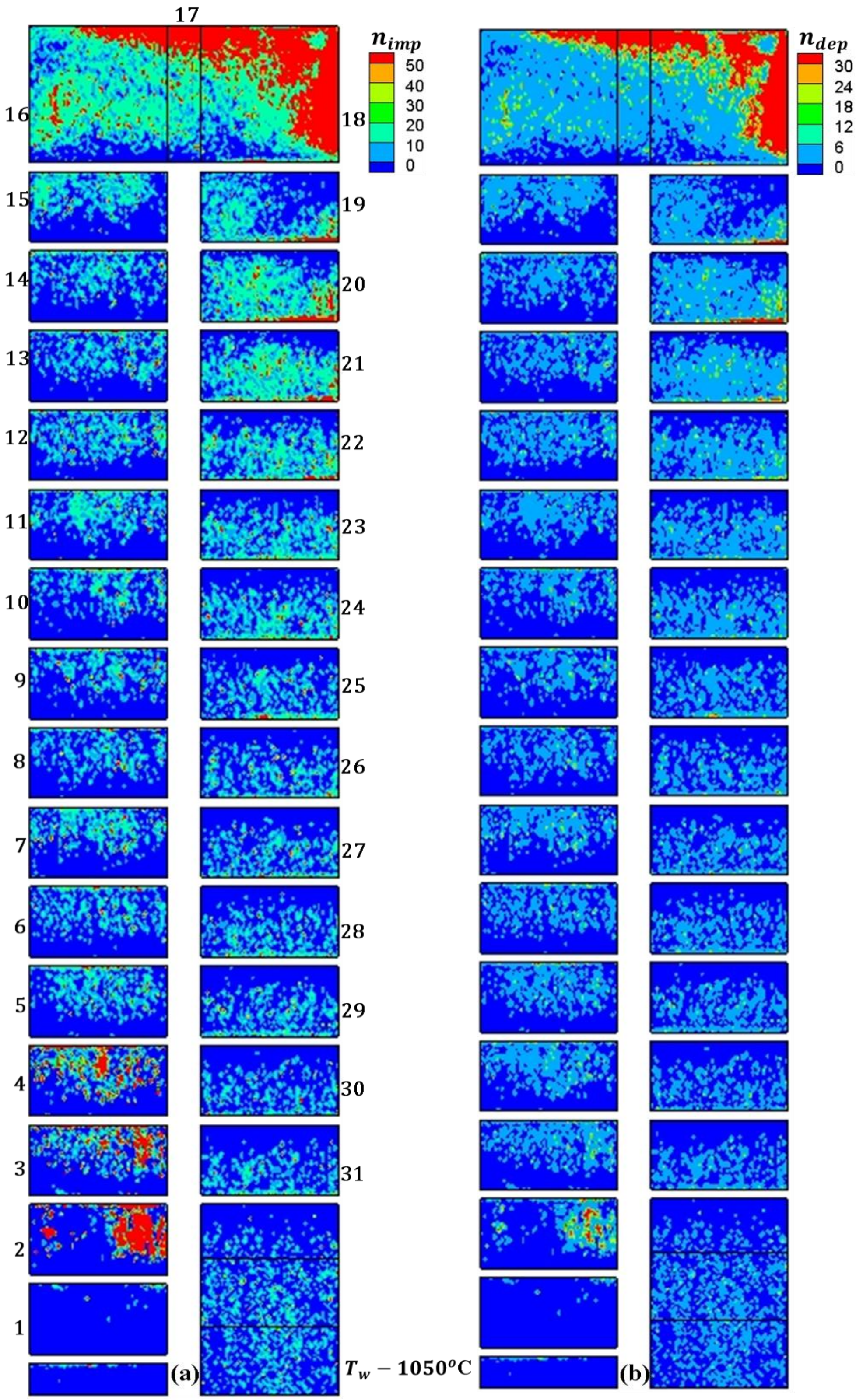

Figure 6.3 Contours of particle impingement (a) and particle deposition (b) on the ribbed wall for wall temperature of 1050^{o}C.

6.2.2 Smooth side walls

For all the three wall temperatures of 950 ^{o}C, 1000 ^{o}C and 1050 ^{o}C, relatively lower particle impingement is observed on the smooth side wall in the first pass and the divider walls, except in small regions in the vicinity of the rib-sidewall junctions. The sidewall in the second pass experiences significantly high particle impingement due to direct flow impingement of the turning flow in the bend. Figure 6.4 shows the particle impingement and deposition pattern on the outer side wall of the second pass for the first six pitches. Distinct patterns of particle impingement are observed at the rib-sidewall junctions at all the sidewalls. This particle impingement is a manifestation of high secondary flows causing spanwise velocities as high as 18% of the mean bulk velocity. There is a clear correlation between impingement patterns and particle diameter (Figure 6.7). The end-side wall adjacent to the 180^{o} bend is dominated by large inertia driven particle impingement which gradually changes to smaller particle impacts as the flow maneuvers the bend carrying smaller particles with it. The core of the secondary flow at the rib-side wall junction is dominated by large particle impacts carried by the strength of the high spanwise velocity into this region, followed by smaller particle impacts as the spanwise velocity weakens. Interestingly, while the average angle of impingement experienced by the particles is high in the side wall region adjacent to the bend, the average velocity of impact is quite low (Figure 6.8). As the flow develops in the second pass, this trend is reversed as the velocity of impact decreases and the angle of impact increases. Small particles (low Stokes number) are very sensitive to the flow field and hence easily carried to the walls by these highly unsteady three dimensional structures. Also, very high particle impingement is observed at the side wall toward the downstream end of the bend, due to direct flow impingement at this wall.

When the particle impingement and deposition is compared for all the three wall temperatures, as observed in the case of ribbed wall, the particle impingement decreases with temperature. This is attributed to the loss of particles upstream due to deposition. The fraction of particles deposited increases with temperature. However the total number of particles deposited is highest for a wall temperature of 1000 ^{o}C. This is because even though the sticking probability is highest at 1050 ^{o}C wall temperature, a significant number of particles are deposited in the upstream region resulting in less number of particles entering the second pass. The side wall region in the bend experiences very high deposition for wall temperatures of 1000 ^{o}C and 1050 ^{o}C.

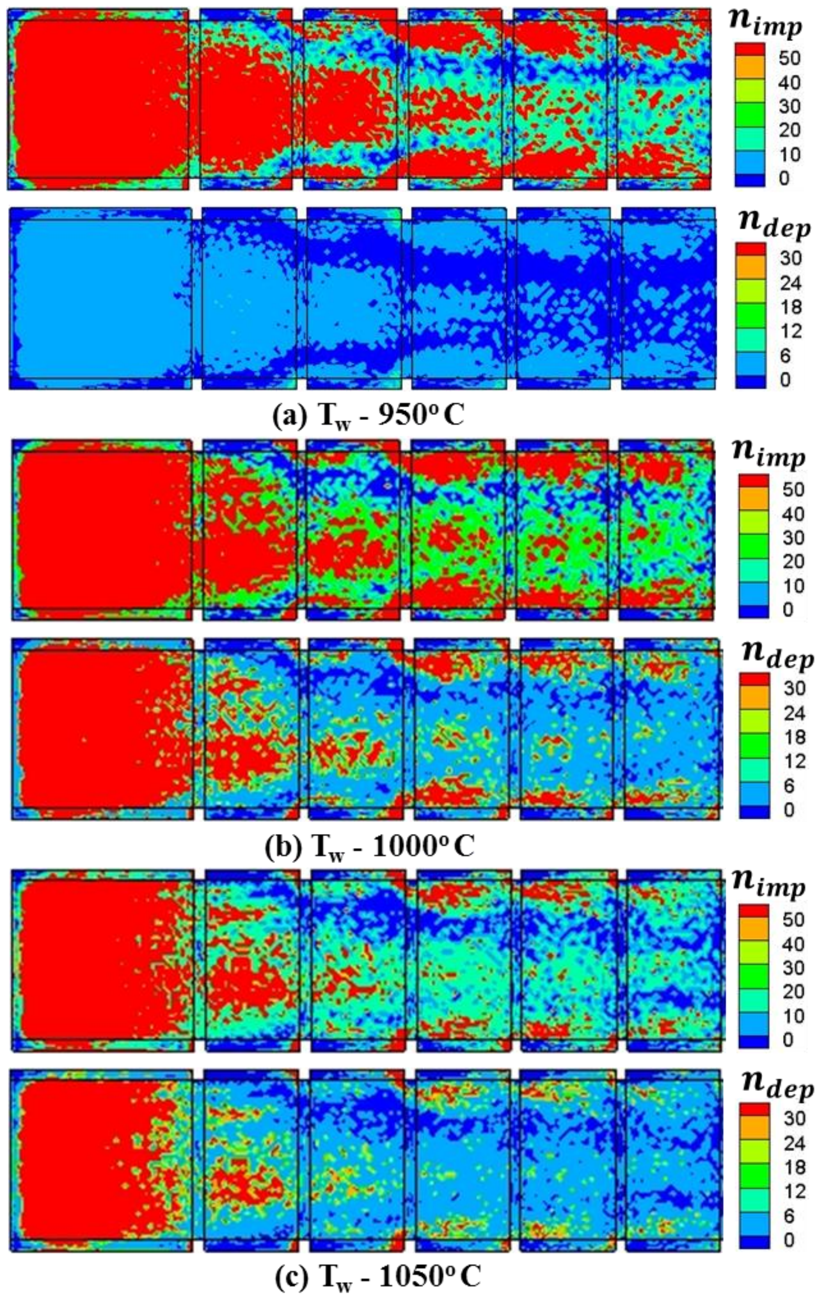

Figure 6.4 Contours of particle impingement and deposition on the side wall of the second pass (pitch # 18-23) for the wall temperature of (a) 950°C, (b) 1000°C and (c) 1050°C

6.2.3 Ribs

Figure 6.6 shows the particle impingement and deposition on the rib faces for six ribs upstream and downstream of the bend, for the representative case of 1000^o C wall temperature. Very high particle impingement is observed on the rib faces facing the flow in both the passes. In addition, the trailing side of the rib also experiences some particle impingement. Particles impinging at the rib backs are mostly a result of them bouncing off of the front face of the following rib with enough momentum to travel backward against the flow. Comparatively higher impingement is seen at rib faces in the second pass than the first pass. This is due to the higher velocities of the particles coming out of the bend and also due to increased transport by turbulent eddies, both of which combine to increase particle impingement at the trailing face of ribs in the second pass. Significant deposition is recorded for the rib faces in the first quarter of the second pass due to reasons discussed earlier.

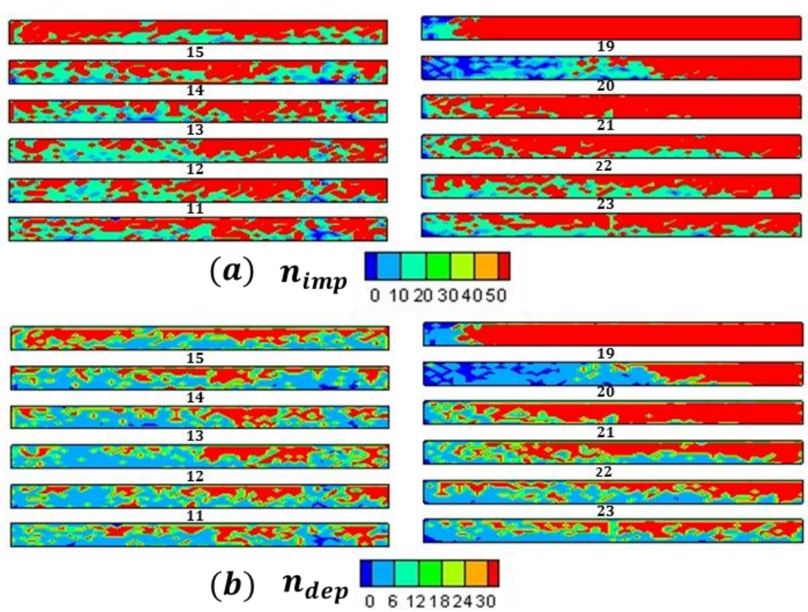

Figure 6.5 Particle impingement (a) and deposition (b) on rib faces in 6 ribs upstream and downstream of the bend (pitch # shown) (T_w = 1000^o C)

6.2.4 Endwall

Figure 6.6 shows particle impingement and deposition for the representative case of 1000^o C wall temperature at the endwall. The surface experiences significantly high particle impingement and deposition mostly due to larger particle impacts as can be found in Figure 6.7. The larger inertia driven particles cannot maneuver the bend and impinge with the endwall head on whereas smaller particles undergo a partial turn before impinging further downstream. This observation is supported by the impact velocity and angle in Figure 6.8. High impact angles representative of head-on collisions is followed by lower impact angles as the smaller particles impinge on the endwall.

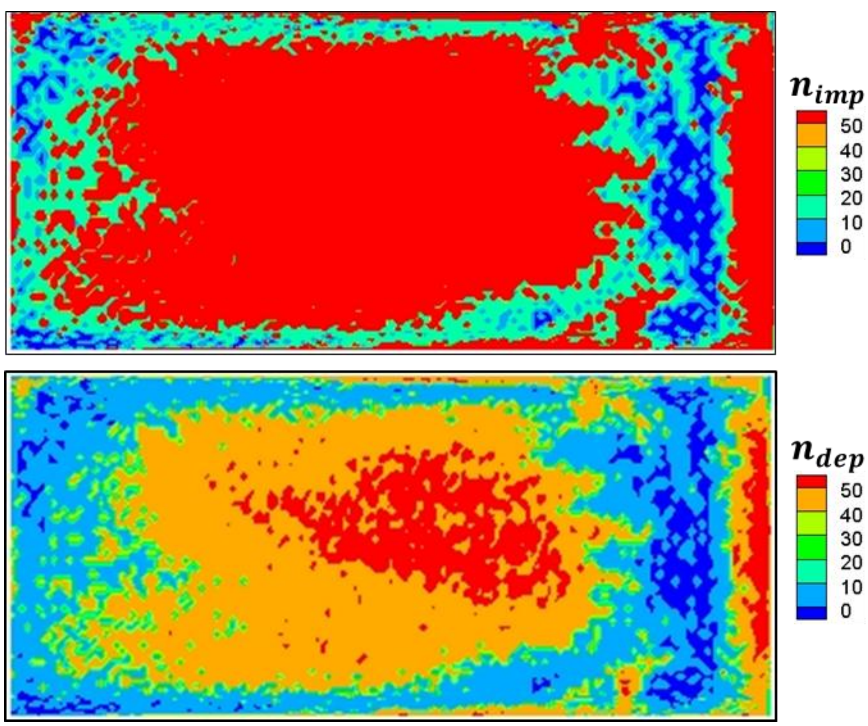

Figure 6.6 Particle impingement and deposition at the endwall surface (T_w = 1000^o C)

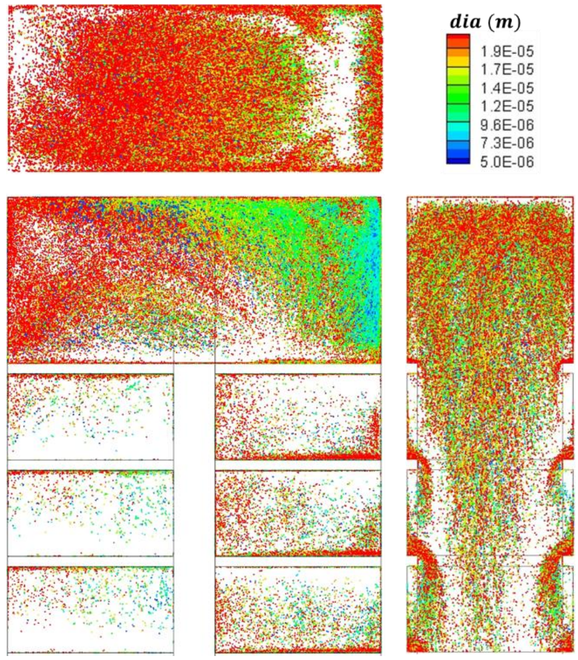

Figure 6.7 Scatter plot of impacting particle diameters on ribbed surface, sidewall and endwall (T_w = 950^o C)

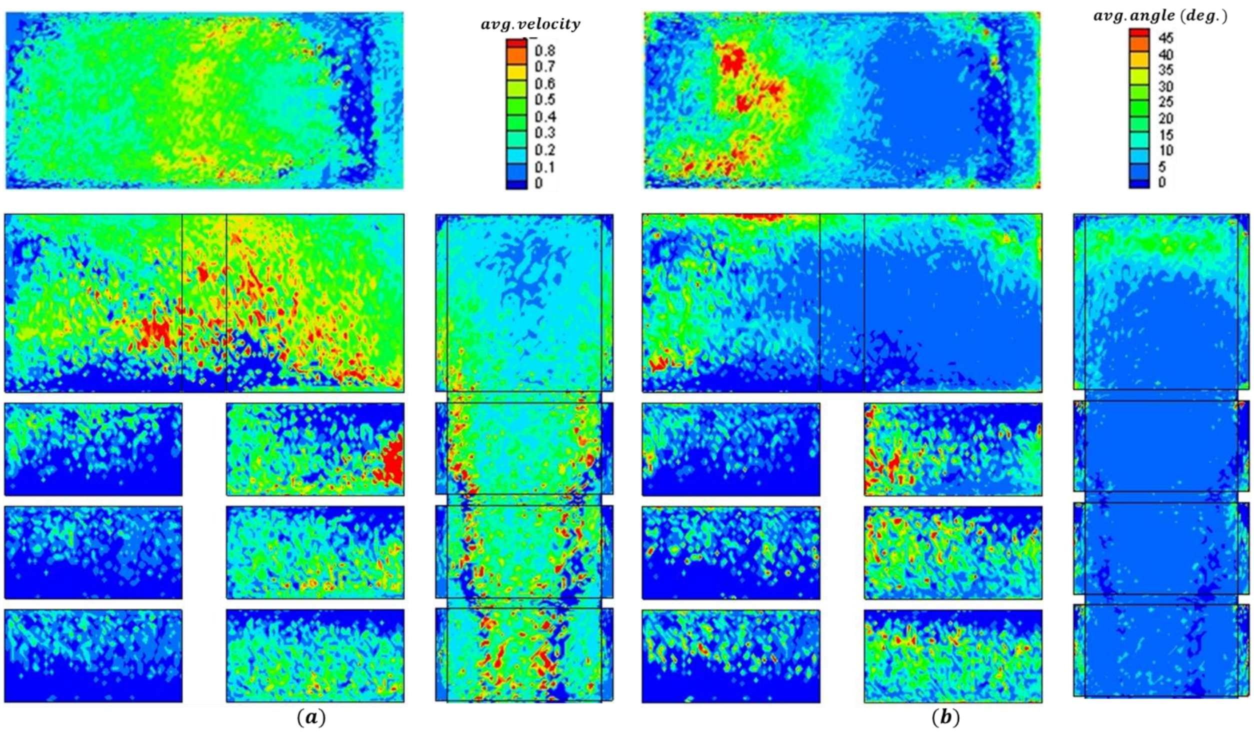

Figure 6.8 Contour plots of average impact velocity (a) and average impact angle on the ribbed surface, sidewall and endwall (T_w = 950^o C)

6.2.5 Pitch-Averaged Characteristics

Figure 6.9 shows, n_{pitch}, the number of leftover particles entering each pitch after deposition upstream. For all the three wall temperatures, a gradual decrease in n_{pitch} is observed with pitch number. For a particular pitch, n_{pitch} decreases with wall temperature due to increased deposition. Roughly 8%, 13% and 16% of the injected particles are lost to deposition in the first pass for the wall temperatures of 950 ^{o}C, 1000 ^{o}C and 1050 ^{o}C, respectively. Significant deposition is observed in the bend region with a sharp drop in $n_{pitch}$for all the three wall temperatures. This is due to the large number of particle impacts and the resultant deposition on the end wall and side walls in the bend. Though significant number of particles are lost to deposition in the first pass, but most of the particles lost are near wall particles while the high Stokes number particles remain in the core of the flow. These core flow particles then impact the end wall and all other surfaces in the bend leading to very high impingement and deposition. As discussed before, particle impingement is significantly higher in the second pass due to higher turbulence and turning flow impacting the side walls. This higher impingement also leads to higher deposition as observed in figure 6.5. Downstream from the bend, in the second pass, the fall in n_{pitch} number is relatively faster compared to the first pass due to higher impingement and resultant deposition from higher turbulence and the turning flow hitting the side walls. In total, approximately 38%, 59% and 67% of the injected particles deposit in the two pass, for the three wall temperatures of 950 ^{o}C, 1000 ^{o}C and 1050 ^{o}C, respectively.

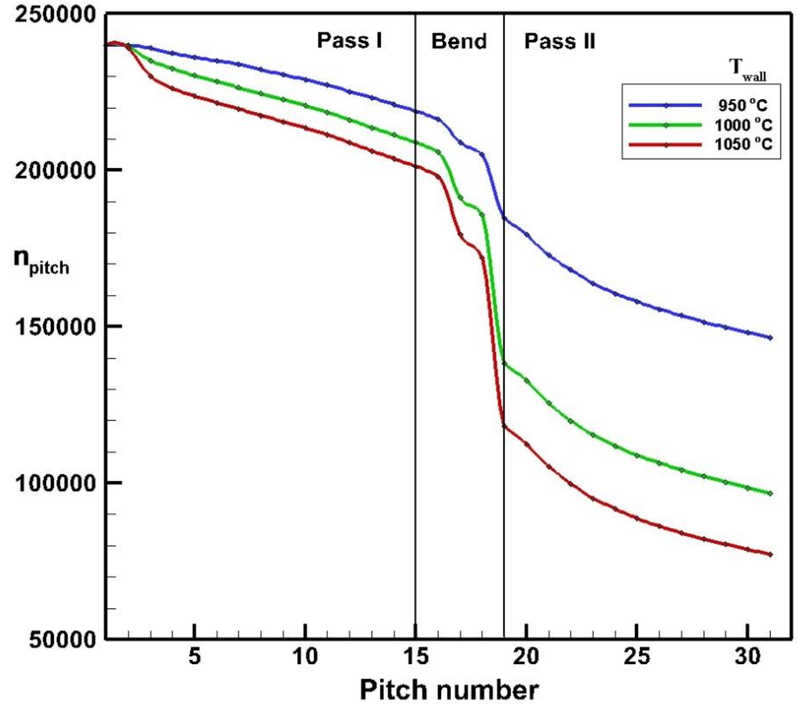

Figure 6.9 Number of particles remaining particles entering each pitch

Figure 6.10 shows the number of particle impacts on all the surfaces per pitch normalized by the pitch area and total number of particles injected at the inlet. For all the three cases, highest particle impingement density is found in downstream half of the bend and the first quarter section of the second pass after the bend region, where the recorded impingement is more than twice that of any other region. It can also be seen that the average particle impingement per pitch is also higher in the second pass than the first pass.

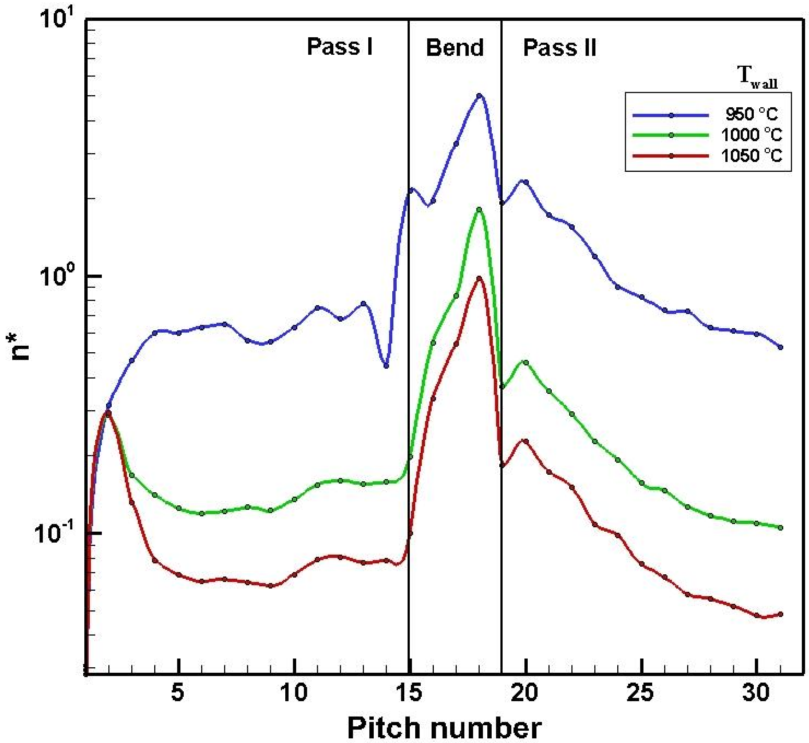

Figure 6.10 Total number of particle impacts per pitch normalized by the pitch area and the number of particles injected

For a particular pitch, the total number of particle impacts decrease with temperature. This decrease in particle impacts is relatively higher going from wall temperature of 950 ^{o}C to 1000 ^{o}C, compared to the same for 1000 ^{o}C to 1050 ^{o}C. This is due to two reasons; first, the number of particles left in the pitch decrease with temperature and second, when the probability of sticking is lower (T_w - 950 ^{o}C), the particles rebound multiple times before depositing whereas at higher sticking probability (T_w - 1050 ^{o}C), particles deposit in fewer rebounds leading to a much lower number of impacts. As confirmed in figure 6.10, this difference in impingement is significantly lower in the bend region where impingement is dominated by the particles in the core flow. For all the three cases, particle impingement in the first pass is more or less same in each pitch, while the impingement decreases in the second pass from bend to the outlet. This is a result of the combination of two major flow features in this region; the direct flow impingement on the walls and high turbulence. The effect of both of these mechanisms decreases as we move downstream of the bend.

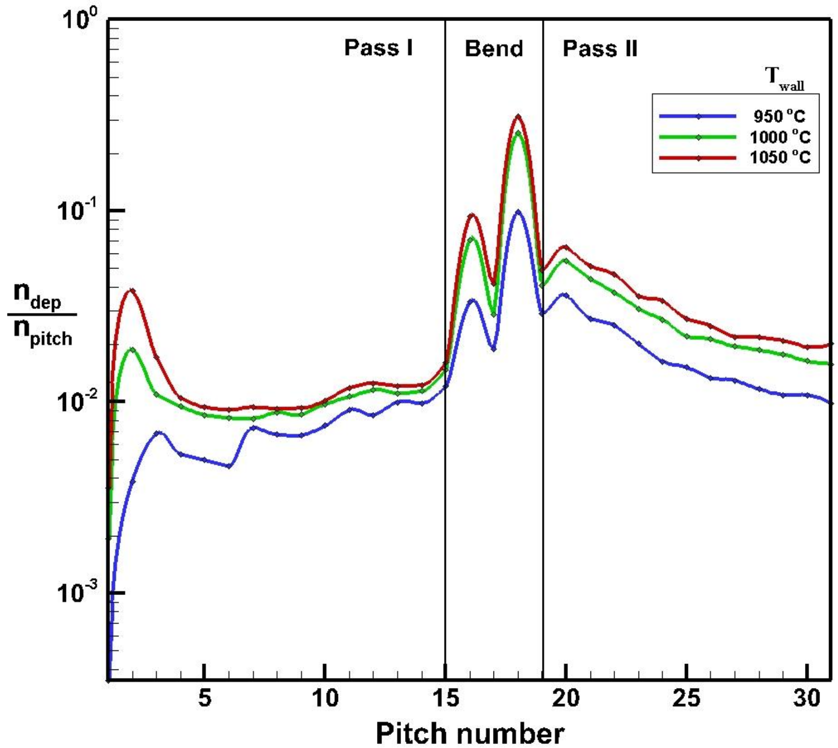

Figure 6.11 Number of particles deposited, n_{dep} , normalized by the number of particles *entering the pitch* (n_{pitch}).

Figure 6.11 shows the number of particles deposited, n_{dep}, normalized by the number of particles *entering the pitch* (n_{pitch}). As expected, the number of deposited particles follows the similar trend with pitch number as observed for number of particle impacts. For each case, higher deposition ratio is observed in the bend region and the second pass compared to the first pass. The particle deposition per pitch is more or less uniform in the first pass, whereas in the second pass it decreases from the bend towards the outlet. The deposition increases with wall temperature. Again, the increase in deposition ratio is relatively high going from a wall temperature of 950 ^{o}C to 1000 ^{o}C, compared to the same for 1000 ^{o}C to 1050 ^{o}C. Another observation is that the difference in particle deposition ratio at wall temperature of 1000 ^oC to 1050 ^oC is larger in the second pass compared to first pass. This is consistent with previous observations of increased deposition downstream of the bend.

6.3 Summary and conclusions

Sand transport and deposition is investigated in a two pass internal cooling geometry at realistic engine conditions. LES calculations are performed for bulk Reynolds number of 25,000 to calculate flow field and heat transfer. Constant wall temperature boundary condition is used to investigate the effect of temperature on particle deposition. Three different wall temperatures of 950 ^oC, 1000 ^oC and 1050 ^oC are considered. Particle sizes in range 5-25 microns are considered, with mean particle diameter of 3 microns. An improved particle-wall interaction and deposition model is used as discussed in Chapter 5. Calculated impingement and deposition patterns are discussed for different exposed surfaces in the two pass geometry. The highest particle impingement and deposition is observed in the bend region and first quarter of the second pass. All side walls experience minimal particle impingement except the outer side wall in the second pass. Rib faces experience significantly high impingement and deposition while rib backs only experience higher impingement in the second pass due to high turbulence intensity and secondary flows. The particle impingement pattern is more uniform in the first pass compared to second pass, as observed in the flow field. Significant deposition is observed in the two pass geometry for all the three wall temperatures considered. Particle impingement and hence deposition is dominated by larger particles except in the downstream half of the bend region. In total, approximately 38%, 59% and 67% of the injected particles deposit in the two pass, for the three wall temperatures of 950 ^oC, 1000 ^oC and 1050 ^oC, respectively. While particle impingement is highest for wall temperature of 950 ^oC, higher deposition is observed for 1000 ^oC and 1050 ^oC cases. Deposition increases significantly with wall temperature, for 1000 ^{o}C case, roughly 12% of the impacting particles, deposit. For 1050 ^{o}C, approximately 23% of the particles deposit on impact. For all the three cases, the second pass experiences higher deposition compared to the first pass due to higher turbulence and direct flow impingement.

This study helps identify the damage prone areas in the internal cooling passages of a turbine blade exposed to sand ingestion. This information can help modify the geometry of the blade or the location of film cooling holes to avoid hole clogging and degradation of heat transfer. For example, a modified bend geometry with gradual turning can reduce the direct flow impingement on the smooth side wall in the second pass. Similarly, if possible, the placement of cooling holes in the vicinity of the downstream end of the bend, should be avoided to prevent hole blockage. Though this study is simplified under the assumptions of constant wall temperature, it is nevertheless an important step in understanding the effect of particulate transport and deposition in serpentine ribbed internal cooling passages.

Chapter 7
Summary and Conclusions

The research presented in this dissertation was motivated by the desire to explore the problem of sand ingestion in gas turbine components which continues to be a major area of concern for the aircraft engine industry for the last several decades. The objective of this dissertation is to investigate sand transport and deposition in the internal cooling passages of turbine blades. A simplified rectangular geometry is simulated to mimic the flow field, heat transfer and particle transport in a two pass internal cooling geometry. Two major challenges are identified while trying to simulate particle deposition. First, no reliable particle-wall collision model is available to calculate energy losses during a particle wall interaction. Second, available deposition models for particle deposition do not take into consideration all the impact parameters like impact velocity, impact angle, and particle temperature. These challenges led to the development of particle wall collision and deposition models in the current study.

First a preliminary simulation is carried out to investigate sand transport in the two pass geometry at ambient conditions. Wall Modeled Large Eddy Simulations (WMLES) are carried out to calculate the flow field and a Lagrangian approach is used for particle transport. For modeling particle-wall interaction, perfectly elastic collisions are considered and deposition is neglected. This exercise was carried out to understand the particle impingement patterns in the two pass geometry. The results showed good agreement with experiments and identified the deposition prone areas in the two pass geometry.

The follow on studies focused on the development of particle-wall collision models by computing the effective coefficient of restitution based on elastic-plastic deformation and adhesion forces during a particle impact. The model builds on available theories of deformation and adhesion for a spherical particle in contact with a flat surface by calculating deformation and adhesion losses from particle-wall material properties and impact parameters. The model is broadly applicable to spherical particles undergoing oblique impact with a rigid wall and successfully predicts the general trends observed in experiments.

To address the issue of predicting deposition, an improved physical model based on the critical viscosity approach and energy losses during particle-wall collisions, is developed to predict the sand deposition at high temperatures in gas turbine components. For validation purposes, the deposition of sand particles is calculated for particle laden jet impingement on a coupon and compared with experiments conducted at Virginia Tech. Large Eddy Simulations are used to calculate the flow and temperature field and particle dynamics is modeled using a Lagrangian approach. The proposed model is novel in the sense that it predicts the sticking probability based on the impact velocity along with the particle temperature. For every particle impacting the coupon surface, the particle velocity and temperature determine if the particle sticks or rebounds. Apart from inevitable uncertainties in the model parameters due to idealizations, there is no calibration involved. Results quantify the sticking, capture efficiency, and rebound ratio for 20-40 microns sand particles. The results show good agreement with the experiments for the range of jet temperatures investigated.

Finally the two pass geometry is revisited with the developed particle-wall collision and deposition models. Sand transport and deposition is investigated in a two pass internal cooling geometry at realistic engine conditions. LES calculations are carried out for a bulk Reynolds number of 25,000 to calculate the flow and temperature fields. Constant wall temperature boundary condition is used to investigate the effect of temperature on particle deposition. Three different wall temperatures of 950 ^{o}C, 1000 ^{o}C and 1050 ^{o}C are considered. Particle sizes in the range 1-20 microns are considered, with a mean particle diameter of 3 microns. Calculated impingement and deposition patterns are discussed for different exposed surfaces in the two pass geometry.

This study helps categorize the deposition prone areas in the internal cooling passages of a turbine blade exposed to sand ingestion. This information can help modify the internal cooling geometry for a turbine blade to minimize heat transfer degradation and film-cooling hole clogging when exposed to sand ingestion. For example, a gradual turning bend in a two pass geometry can reduce the direct flow impingement on the smooth side wall in the second pass. Similarly, if possible, the placement of cooling holes in the vicinity of the downstream end of the bend, should be avoided to prevent hole blockage. Though this study is simplified under the assumptions of constant wall temperature, it is nevertheless is an important step in understanding the effect of particulate transport and deposition in serpentine ribbed internal cooling passages.

This thesis makes the following engineering and scientific contributions to the literature.

- Wall-Modeled Large Eddy Simulations used to predict flow filed and heat transfer in a two pass geometry which significantly reduces the grid requirements.
- A first of its kind study gives an insight into the particle impingement and deposition in the serpentine internal cooling passages of gas turbine blades
- An improved particle-wall collision model is presented based on deformation and adhesion losses.
- An improved particle deposition model is presented to predict sand deposition at high temperatures in gas turbine components.

Following is the list of peer reviewed conference papers and journal papers written as an integral part of this dissertation.

Conference papers

- Singh, S., Tafti, D., 2012, "Detailed Heat Transfer in a Two Pass Internal Cooling Duct With Rib Turbulators Using Wall Modeled Large Eddy Simulations (WMLES)," ASME 2012 Heat Transfer Summer Conference, Puerto Rico, USA, July 8–12, 2012, 1(Paper no. HT2012-58260), pp. 791-800.
- Singh, S., Reagle, C., Delimont, J., Tafti, D., Ng, W., and Ekkad, S., "Sand Transport in a Two Pass Internal Cooling Duct With Rib Turbulators," Proc. ASME 2012 Heat Transfer Summer Conference collocated with the ASME 2012 Fluids Engineering Division Summer Meeting and the ASME 2012 10th International Conference on Nanochannels, Microchannels, and Minichannels, American Society of Mechanical Engineers, pp. 727-735.
- Singh, S., and Tafti, D., "Predicting the Coefficient of Restitution for Particle Wall Collisions in Gas Turbine Components," Proc. ASME Turbo Expo 2013: Turbine Technical Conference and Exposition, American Society of Mechanical Engineers, pp. V06BT37A041-V006BT037A041.

Journal papers

- Singh, S., Tafti, D., Reagle, C., Delimont, J., Ng, W., and Ekkad, S., 2014, "Sand transport in a two pass internal cooling duct with rib turbulators," Int J Heat Fluid Fl, 46(0), pp. 158-167.
- Singh, S. and Tafti D., 2014, “Predicting the Coefficient of Restitution for Particle Wall Collisions in Gas Turbine Components”, Int J Heat Fluid Flow, Under Review
- Singh, S. and Tafti D., 2014, “Particle Deposition Model for Particulate Flows at High Temperatures in Gas Turbine Components”, to be submitted.

- Singh, S. and Tafti D., 2014, “Sand transport and deposition in a two pass internal cooling duct with rib turbulators”, to be submitted.

Appendix A

Nomenclature

$\vec{a}^{i}$	Contravariant basis vector
a	Contact radius
A	Area of contact
B	Contact area material property coefficient
C	Critical yield stress coefficient
C_p	Specific heat
D_h	Hydraulic diameter
e	Coefficient of restitution, rib height
E	Elastic modulus
H_G	Hardness geometric limit
d_p	Particle diameter
C_d	Drag coefficient
g^{ij}	Contravariant metric tensor
$\sqrt{g}$	Jacobian of transformation
$\sqrt{g}U^{j}$	Contravariant flux vector
k	Thermal conductivity
K	Hardness factor

L_c^*	Characteristic length
m	Mass of the particle
n	Number of particles
$\vec{n}$	Surface normal vector
Nu	Nusselt number
p	Fluctuation pressure
P	Probability of sticking, contact force
q	Heat flux
$\Pr$	Prandtl number
$\Pr_t$	Turbulent Prandtl number
R	Radius
Re	Reynolds number
Re_p	Particle Reynolds number
St	Momentum Stokes number
St_{conv}	Convective Stokes number
St_{rad}	Radiative Stokes number
S_y	Yield strength
t	Time
T	Temperature
u_b	Mean bulk velocity

v	Instantaneous velocity
U	Velocity
V	Particle velocity
ω	Interference/Deformation
W_A	Work of adhesion
$\vec{x}$	Physical space coordinate
α	Impact angle with the surace
γ	Surface adhesion energy parameter
θ	Non-dimensional temperature
ε	Dissipation rate of turbulent kinetic energy
η	Coefficient of friction, efficiency
ρ	Density
μ	Dynamic Viscosity
$\vec{\xi}$	Computational space coordinates
τ	Shear stress
ν	Kinematic viscosity

Subscripts/superscripts

1	Incidence value for particles
2	Rebound value for particles
a	Computational space coordinate
ad	Adhesion regime

c	Critical value at onset of plastic deformation
cap	Capture
dep	Deposited
ep	Based on elastic plastic losses
e	Based on coefficient of restitution
f	Fluid
imp	Impact
inj	Injected
inp	Injected on projected area
jet	Inlet jet
p	Particle
pitch	Particles entering the pitch
res	Residual value
$soft$	Softening Temperature
stick	Sticking
t	Tangential to the surface
m	Maximum value
n	Normal to the surface
*	Dimensional quantity

Appendix B

Tecplot macro for particle animation

```
#!MC 1100
$!VarSet |MFBD| = 'C:\Program Files\Tecplot\Tec360\Bin'
$!VarSet |DIR| = 'S:\RR Project\2pass22\Fresh\ParticleSimulations\'
$!VarSet |AVIFILE| = 'Animations\sample.avi'
$!VarSet |INNERDIR| = '0'
$!READDATASET  '"|DIR|tecplot.plt" '
  READDATAOPTION = NEW
  RESETSTYLE = YES
  INCLUDETEXT = NO
  INCLUDEGEOM = NO
  INCLUDECUSTOMLABELS = NO
  VARLOADMODE = BYNAME
  ASSIGNSTRANDIDS = YES
  INITIALPLOTTYPE = CARTESIAN3D
  VARNAMELIST = '"x" "y" "z"'
$!READSTYLESHEET  "|DIR|xy2.sty"
  INCLUDEPLOTSTYLE = YES
  INCLUDETEXT = YES
  INCLUDEGEOM = YES
  INCLUDEAUXDATA = YES
  INCLUDESTREAMPOSITIONS = YES
  INCLUDECONTOURLEVELS = YES
  MERGE = NO
  INCLUDEFRAMESIZEANDPOSITION = NO
$!ALTERDATA
  EQUATION = '{npar_glb}=0.0'
$!ALTERDATA
  EQUATION = '{u}=0.0'
$!ALTERDATA
  EQUATION = '{v}=0.0'
$!ALTERDATA
  EQUATION = '{w}=0.0'
$!ALTERDATA
  EQUATION = '{t}=0.0'
$!FIELDMAP [1-153]  MESH{SHOW = NO}
$!FIELDMAP [1-153]  CONTOUR{SHOW = NO}
$!FIELDMAP [1-153]  VECTOR{SHOW = NO}
$!FIELDMAP [1-153]  SCATTER{SHOW = NO}

# EXPORTSETUP: SetValue command that sets the attributes for exporting
image files from Tecplot.

$!EXPORTSETUP
  EXPORTFORMAT = AVI
  EXPORTFNAME = "|DIR||AVIFILE|"
```

```
  BITDUMPREGION = CURRENTFRAME
  IMAGEWIDTH = 4000
  USESUPERSAMPLEANTIALIASING = NO
  ANIMATIONSPEED = 10

$!FRAMELAYOUT XYPOS{X = 0.5}
$!FRAMELAYOUT XYPOS{Y = 1.0}
$!FRAMELAYOUT WIDTH = 9
$!FRAMELAYOUT HEIGHT = 6

#TOTAL NUMBER OF FRAMES TO LOOP THROUGH


$!VarSet |CURRENT| = '1'
$!VARSET |NUMFILES| = 104

$!LOOP |NUMFILES|
$!VarSet |CURRENT| += 1

# IF LOOP for distinction between digits when reading the file
$!IF |LOOP| <= 9
$!VarSet |INPUTFILE1| = 'parplot\parplot.000|LOOP|.dat'
$!ENDIF

$!IF |LOOP| > 9
$!IF |LOOP| <= 99
$!VarSet |INPUTFILE1| = 'parplot\parplot.00|LOOP|.dat'
$!ENDIF
$!ENDIF

$!IF |LOOP| > 99
$!IF |LOOP| <= 999
$!VarSet |INPUTFILE1| = 'parplot\parplot.0|LOOP|.dat'
$!ENDIF
$!ENDIF

$!IF |LOOP| > 999
$!VarSet |INPUTFILE1| = 'parplot\parplot.|LOOP|.dat'
$!ENDIF


$!READDATASET  '"|DIR||INPUTFILE1|" '
  READDATAOPTION = APPEND
  RESETSTYLE = NO
  INCLUDETEXT = NO
  INCLUDEGEOM = NO
  INCLUDECUSTOMLABELS = NO
  VARLOADMODE = BYNAME
  ASSIGNSTRANDIDS = YES
  INITIALPLOTTYPE = CARTESIAN3D
  VARNAMELIST = '"x" "y" "z" "npar_glb" "u" "v" "w" "t"'
$!FIELDLAYERS SHOWSCATTER = YES
```

```
$!ACTIVEFIELDMAPS += [154-306]
$!FIELDMAP [154-306]  SCATTER{SYMBOLSHAPE{GEOMSHAPE = SPHERE}}
$!FIELDMAP [154-306]  SCATTER{COLOR = RED}
$!FIELDMAP [154-306]  SCATTER{FRAMESIZE = 0.25}

$!IF |LOOP| == 1
  $!EXPORTSTART
    EXPORTREGION = CURRENTFRAME
$!ENDIF
$!IF |LOOP| != 1
  $!EXPORTNEXTFRAME
$!ENDIF

$!DELETEZONES  [154-306]

$!ENDLOOP

$!EXPORTFINISH
$!RemoveVar |MFBD|
```

Appendix C

Copyrights and Permissions

Copyright Clearance Center RightsLink®

Home | Account Info | Help

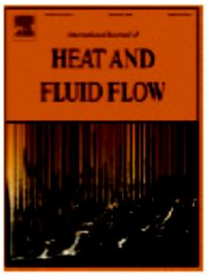

Title:	Sand transport in a two pass internal cooling duct with rib turbulators
Author:	Sukhjinder Singh,Danesh Tafti,Colin Reagle,Jacob Delimont,Wing Ng,Srinath Ekkad
Publication:	International Journal of Heat and Fluid Flow
Publisher:	Elsevier
Date:	April 2014

Logged in as:
Sukhjinder Singh

LOGOUT

Order Completed

Thank you very much for your order.

This is a License Agreement between Sukhjinder Singh ("You") and Elsevier ("Elsevier"). The license consists of your order details, the terms and conditions provided by Elsevier, and the payment terms and conditions.

Get the printable license.

License Number	3335990131289
License date	Feb 25, 2014
Licensed content publisher	Elsevier
Licensed content publication	International Journal of Heat and Fluid Flow
Licensed content title	Sand transport in a two pass internal cooling duct with rib turbulators
Licensed content author	Sukhjinder Singh,Danesh Tafti,Colin Reagle,Jacob Delimont,Wing Ng,Srinath Ekkad
Licensed content date	April 2014
Licensed content volume number	46
Number of pages	10
Type of Use	reuse in a thesis/dissertation
Portion	full article
Format	both print and electronic
Are you the author of this Elsevier article?	Yes
Will you be translating?	No
Title of your thesis/dissertation	Large Eddy Simulations of Sand Transport and Deposition in the Internal Cooling Passages of Gas Turbine Blades
Expected completion date	Mar 2014
Estimated size (number of pages)	200
Elsevier VAT number	GB 494 6272 12
Permissions price	0.00 USD
VAT/Local Sales Tax	0.00 USD / 0.00 GBP
Total	0.00 USD

Sukhjinder Singh

From: Beth Darchi <DarchiB@asme.org>
Sent: Thursday, March 13, 2014 2:34 PM
To: 'Sukhjinder Singh'
Subject: RE: Post publishing copyright request

Dear Mr. Singh,
It is our pleasure to grant you permission to publish the following ASME materials:

- "Predicting the Coefficient of Restitution for Particle Wall Collisions in Gas Turbine Components," by Sukhjinder Singh and Danesh Tafti, Paper Number GT2013-95623
- "Detailed Heat Transfer in a Two Pass Internal Cooling Duct With Rib Turbulators Using Wall Modeled Large Eddy Simulations (WMLES)," by Sukhjinder Singh and Danesh Tafti, Paper Number HT2012-58260
- **Figures 1, 2** from "Study of Microparticle Rebound Characteristics Under High Temperature Conditions," by C. J. Reagle, J. M. Delimont, W. F. Ng and S. V. Ekkad, J. Eng. Gas Turbines Power, Volume 136(1), 2013

as cited in your letter for inclusion in a Dissertation entitled Large Eddy Simulations of Sand Transport and Deposition in the Internal Cooling Passages of Gas Turbine Blades to be published by Virginia Tech.

Permission is granted for the specific use as stated herein and does not permit further use of the materials without proper authorization. Proper attribution must be made to the author(s) of the materials. **Please note**: if any or all of the figures and/or Tables are of another source, permission should be granted from that outside source or include the reference of the original source. ASME does not grant permission for outside source material that may be referenced in the ASME works.

As is customary, we request that you ensure proper acknowledgment of the exact sources of this material, the authors, and ASME as original publisher. Acknowledgment must be retained on all pages printed and distributed.
Many thanks for your interest in ASME publications.

Sincerely,

ASME
SETTING THE STANDARD

Beth Darchi
Publishing Administrator
ASME
2 Park Avenue, 6th Floor
New York, NY 10016-5990
Tel 1.212.591.7700
darchib@asme.org